A Design Calculating System for Deep Drawing Die by Using Simulation Model

Kadhim M. Abed

Mech. Eng. Department

Collage of Engineering

Thi-Qar University

kahdimabd@yahoo.com

Abstract

In this research, the deep drawing dies are designed by using a "computer - aided designed calculating system" to save time and facilitate the design process. Also finite elements method (FEM) is used to simulate the drawing process to select the best die design. A programming language (VISUAL BASIC 6.0) was used to build the computer – aided design system, which was linked to drafting package (AutoCAD) to plot the deep drawing dies. A commercially available finite elements program code (ANSYS) was used to perform the numerical simulation. Finite elements results is compared with experimental results. Though the compression between the experimental and FEM, it has concluded that finite elements method is more accurate than the experimental method in predicting the best die design, and a good match between the two methods was found.

Keywords : Deep drawing , dies design , finite element.

نظام الحسابات التصميمية لقوالب السحب العميق باستخدام المحاكاة

المستخلص

في هذا البحث تم تصميم قوالب السحب العميق باستخدام " نظام الحسابات التصميمية بمساعدة الحاسوب" ، لتوفير الوقت ولتسهيل عملية التصميم. كذلك تم استخدام طريقة العناصر المحددة (FEM) لمحاكاة عملية السحب العميق ولاختيار تصميم القالب الأفضل.استخدمت لغة البرمجة (VISUAL BASIC 6.0) لبناء نظام تصميم قوالب السحب العميق بمساعدة الحاسوب التي تم ربطها مع برنامج الرسم (AutoCAD) لرسم قوالب السحب الناتجة من النظام. وقد تمت الاستفادة أيضا من إمكانيات برنامج العناصر المحددة لنظائر (ANSYS)لانجاز المحاكاة الرقمية لعملية السحب العميق. وقد تم مقارنة النتائج المستخرجة من المحاكاة باستخدام العناصر المحددة مع النتائج العملية لبعض الجروف المنشورة. لقد وجد من خلال المقارنة بين الطريقة العملية وطريقة العناصر المحددة، إن طريقة العناصر المحددة أكثر دقة من الطريقة العملية في اختيار تصميم القالب الأفضل، وانه يوجد تطابق جيد بين النتائج المستخرجة نتيجة لاستخدام الطريقتين.

1- Introduction

This work demonstrates the design and development of an algorithm that represent stages of computer-aided design calculation and finite elements simulation of deep drawing process that facilitate in making the design of drawing process and predicting drawing variables easier, faster , cheaper and more reliable[1]. The computer – aided system requires developing and using a database to present inputs (blank material properties) to this algorithm. VISUAL BASIC programming used to build the computer-aided calculation system , AutoCAD program linked automatically to the computer aided system to plot the deep drawing dies. ANSYS programming is used to simulate the drawing process as a finite elements software.

2- Computer-aided design of deep drawing

The architecture of Computer – Aided Deep Drawing Design and Simulation system as shown in Figure (1)

2-1 Cup geometry input

Include input of cup internal diameter (d), cup height (h), and thickness (t). This is the first stage in deep drawing dies design, which depends on cup geometry.

2-2 Product (cup) database

Consist of empirical equations which used to build the system, and database file containing necessary information about sheet metal to be drawn, such as metal name , and type using two international classifications (US), and (DIN) , also yield stress, ultimate stress, drawing ratio (LDR) , and lubrication.

2-3 Blank and Die design calculation[2]

Blank and die design include the following:

2-3-1 Blank design

Blank diameter can be calculated using equation (1):

$$D = (d^2 - 4\,d\,h)^{0.5} \quad (1)$$

where h= cup height (mm),

d = cup diameter (mm),

D= blank diameter (mm).

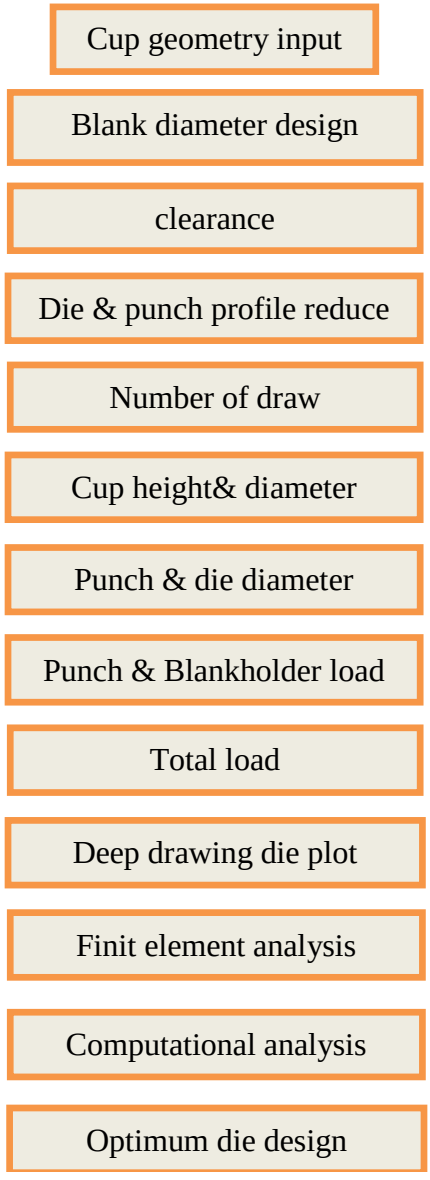

Figure (1). The system architecture.

2-3-2 Die design

Die design includes many stages

❖ Clearance determination:

Clearance is the gap between punch and die, in this work clearance is equal to 0.55 mm.

❖ Determining punch profile radius (r_p)

Punch profile radius ranges from 4 to 10 times of metal thickness, in this work (r_p) is set as (10 mm). The value of (r_p) can be changed to match the profile radius of the cup to be drawn, or by the designer.

❖ Determining die Profile radius (r_D) :

Die profile radius range from 4 to 10 times of metal thickness, in this design (r_D) is set as (10 mm) .The value of (r_D) can be changed by the designer.

❖ Determining number of draws:

Number of die(s) necessary to produce the desired product (cup) depends on "cup height over cup diameter" (h/d) ratio as shown in (Table 1).

Table(1). The relationship between the (h/d) ratio and number of draws.

If h/d < 0.75	then no. of draws = 1
If 0.75 < h/d < 1.5	then no. of draws = 2
If 1.5 < h/d < 3.0	then no. of draws = 3
If 3.0 < h/d < 4.5	then no. of draws = 4

❖ Determining cup(s) height:

Cup (s) height for each draw can be estimated using equation (1):

❖ Determining cup(s) diameter:

Cup(s) diameter for each draw can be estimated using equation (2):

$$P = 100 \left(1 - \frac{d}{D}\right) \quad (2)$$

where P = percentage reduction

d = inner diameter of drawn cup (mm)

D = blank diameter (mm)

❖ Determining punch(s) diameter:

Punch diameter for the first draw is equal to the diameter of the cup to be drawn (d), and for other draws equal to the cup diameter at that draw.

❖ Determining die(s) diameter:

Die diameter for each draw can be determined using the following formula:

Die diameter = punch diameter + (2 * clearance) (3)

❖ Determining punch load(s):

Maximum punch load for each draw can be estimated using equation (4):

$F_{max} = \pi\, d\, t\, \sigma_{ult}\, ((D/d) - 0.7)$ (4)

where F_{max} = maximum drawing force (N),

t = original blank thickness (mm),

σ_{ult} = tensile strength (Mpa),

D = blank diameter (mm),

d =punch diameter (mm)

The constant (0.7) is a correction factor to account for friction.

❖ Determining blankholder load(s):

Blankholder load for each draw can be determined using the following formula:

Blank holder load = 1/3 * maximum punch load (5)

❖ Determining total load(s):

Total load for each draw can be determined using the following formula:

Total load = maximum punch load + blank holder load (6)

2-3-3 Plot the die(s)

Result of the design will be plotted using (AutoCAD) programming.

3- Simulation of deep drawing

In this work finite element method was used to simulate deep drawing process which is performed experimentally by (Al – Bassam) [2], and a comparison between results of the two methods (FEM& experimental) achieved.

3-1 Finite element method

The use of finite element analysis is beneficial in the design of tooling in sheet metal forming operations because it is more cost effective than trial and error. The prime objective of an analysis is to assist in the design of the product by: (1) predicting the material deformation and (2) predicting the forces and stresses necessary to execute the forming

operation. FE of the sheet metal forming problem usually adopts one of three analysis methods based on the membrane, shell and continuum element [3,4].

3-2 Blank properties

An axisymmetric cup was formed using a blank of mild steel type (SAE 1006). Chemical composition of the blank material is C% = (0.08), Mn% = (0.25 – 0.45). Thickness and diameter of the blank used in the FEM analysis are taken as (0.42) mm and (454.31) mm respectively.

3-3 Drawing tools properties

Drawing tools consist of the effective parts (punch, die, and blankholder), other accessories (upper plate, lower plate, guides, and etc.) were neglected to simplify the simulation and to save analysis time. Due to the symmetry of the problem, only one – half of the blank and the tools is modeled. Tool geometry) is as follows:

Punch diameter (D_p) and height (h_p) are taken as 120 mm and 60 mm respectively. Die outer diameter, inner diameter (D_d), and height are taken as 200 mm, 121.1 mm, and 50 mm respectively. Blankholder diameter and height are taken as 123 mm, and 8mm respectively. Punch velocity was constant and equal to 10 mm/min.

To produce the drawn part, one draw is needed, since the ratio of cup height to its diameter is less than (0.75) as mentioned in Table (1).

To study the effect of clearance between punch and die, four dies with different inner diameters of (120.9, 121, 121.1, and 121.14) mm with one punch of 120 mm diameter were used .Thus, clearance between punch and dies were (0.45, 0.50, 0.55,and 0.57) mm respectively. Punch and dies profile radius are taken as 15 mm, and 6 mm respectively.

3-4 Finite element analysis

3-4-1 Preprocessing

This stage includes the creation of a geometric model for the part to be formed, the selection of the appropriate boundary conditions for the forming process, and the selection of material and process variables, and it include the following steps[4]:

i. Define elements types and material properties for blank and tools

❖ Define blank element type:

The element used to simulate the blank is (**VISCO106 2-D Large Strain Solid)** .VISCO 106 is used for 2-D modeling of solid structures, and it is defined by four nodes

having up to three degrees of freedom at each node: translations in the nodal X, Y, and Z directions. The geometry, node locations, and the coordinate system for this element are shown in Figure (2).

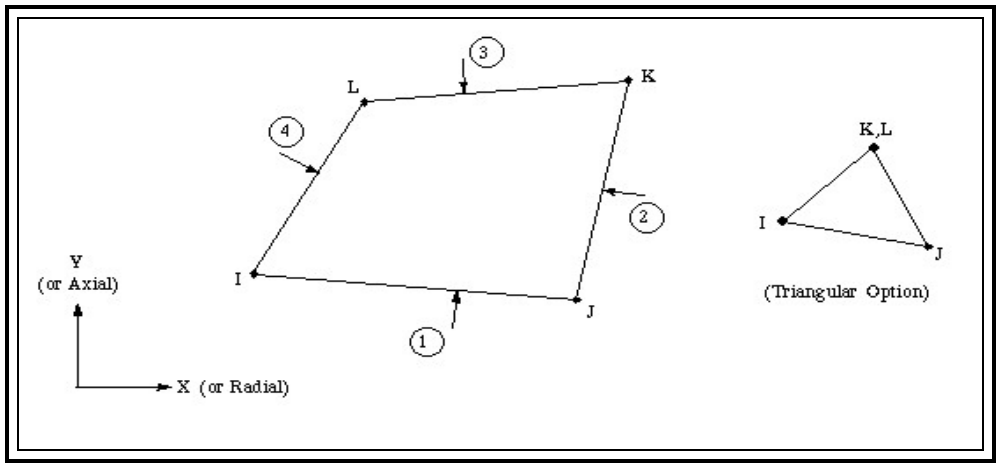

Figure (2). Visco106 2-D large strain solid element [4,5].

❖ Define blank material properties:

Material properties include Young Modulus (200GPa), Density(7800 Kg/m^3), Poisson Ratio (0.3), Coefficient of Friction (0.1), Yield Stress (220 MPa), Tangent Modulus (0.5)

❖ Define tools element type:

In this work, the element used to represent tool set of deep drawing (punch, die, and blankholder) is (**PLANE42 2-D Structural Solid**).PLANE 42 is used for 2-D modeling of solid structures. The element is defined by four nodes having two degrees of freedom at each node: translations in the nodal X, and Y directions. The geometry, node locations, and the coordinate system for this element are shown in Figure (3).

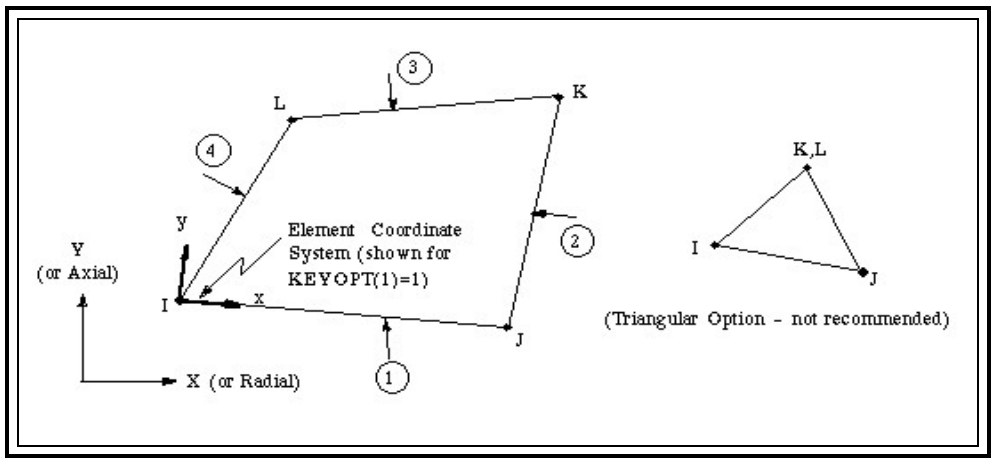

Figure (3). Plane42 2-D structural solid element [4, 5].

❖ Input tools material properties:

Material properties include Young Modulus (220 GPa), Poisson Ratio (0.3), Coefficient of Friction (0.1)

❖ Define contact element:

The element used to represent the contact between the tool set (punch ,die , and blankholder) and the blank is (**CONTAC48 2-D Point-to-Surface Contact)** . This element has two degrees of freedom at each node: translations in the nodal X and Y directions. Contact occurs when the contact node penetrates the target line, Elastic Coulomb friction and rigid Coulomb friction are allowed, where sliding is along the target line. The geometry and node locations are shown in Figure (4).

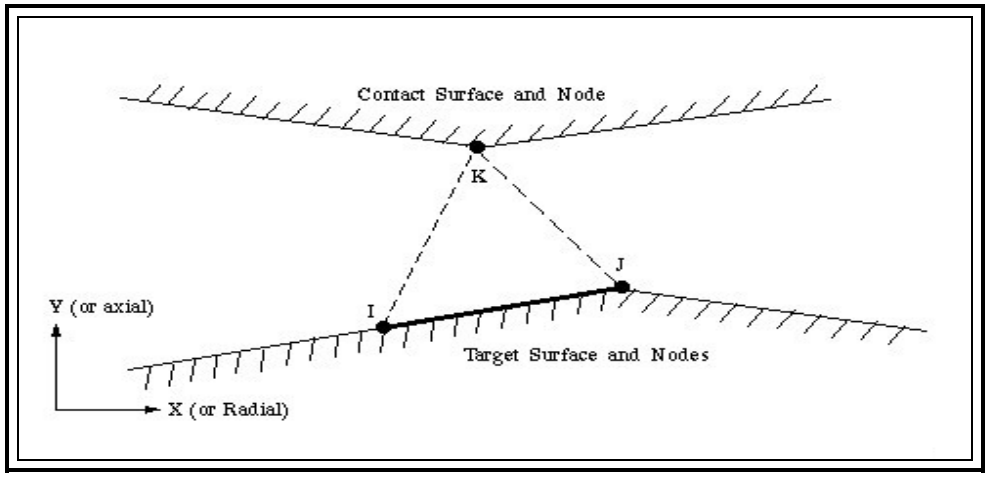

Figure (4). Contact48 2-D node-to-node contact [4,5].

ii. Set Real Constant:

After defining the element type, it needs to select the correct real constants set. The real constant set for each contact surface must be the same as the one used for the corresponding target surface for each contact pair. Each contact pair must refer its own real constant number. In this work "seven" contact pairs are used, i.e. seven real constant values are used.

iii. Generation of Geometric Model:

The model generated using, key points, lines, area, and area meshing.

iv. Set Contacts:

- ❖ Contact between punch and blank (three "node – to – surface" contacts)
- ❖ Contact between blankholder and blank (one "node – to – surface" contact)
- ❖ Contact between die and blank (two "node – to – surface" contacts)
- ❖ Contact between die and blankholder (one "surface – to – surface" contact).

v. Boundary conditions:

Set the geometry to be axisymmetric around y= 0 (axis y-y) and set blankholder load = 15 KN and fixing the die at points (1,2,3) (no displacement in both x & y directions) as shown in Figure (5).

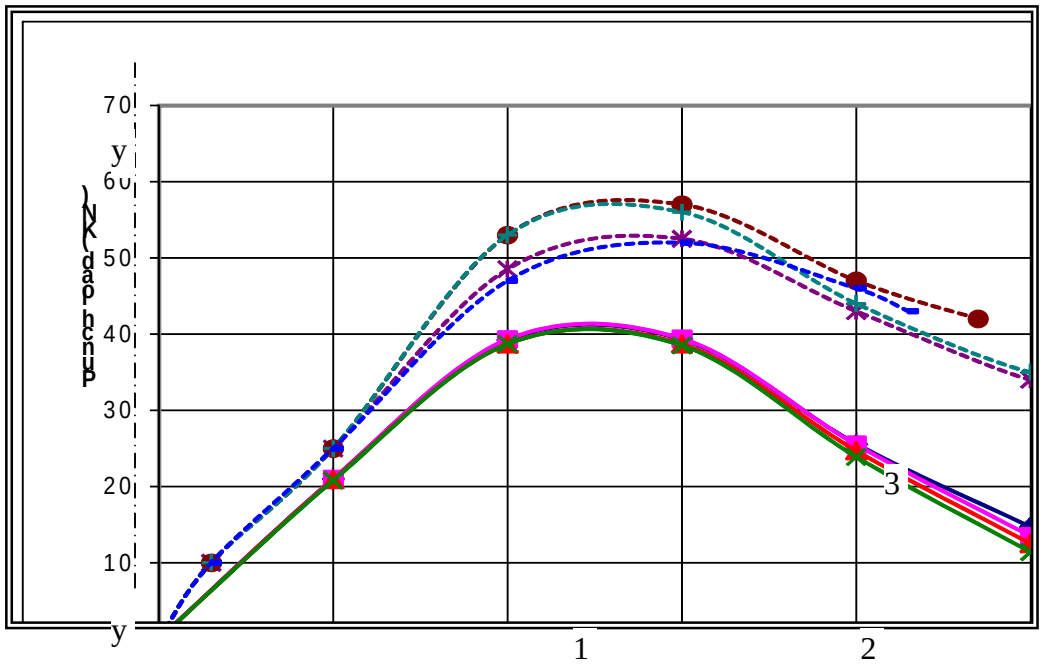

Figure (5). FEM model.

vi. Applying displacement to punch:

Punch moves downward to draw the blank inside the die to produce a cup, this movement consists of (11 steps) (maximum), in each step the punch moves a distance of (5) mm, to reach a maximum total displacement of (55) mm. Punch speed equal to (10) mm/ min.

Speed (v) = displacement (u)/ time (t) (7)

3-4-2 Computational analysis:

The data set prepared in preprocessing stage is used as input to the finite elements code itself, which construct and solve a system of non-linear algebraic equations.

4- Results and discussion

4-1- Implementation

Figure (6) shows a screen used to input cup dimensions which are; cup diameter = (120) mm, cup thickness (0.42) mm, while cup height is deeper here and equal to (400) mm.

Figure (7) illustrates blank material properties screen. This screen contains information about properties of the blank to be drawn, like metal type , the type of the used metal is " Mild Steel" , and metal designation in two international classifications (US) and (DIN) , the used metal designation in (US) is (SAE 1006) , and (RRSt 14) using (DIN). Also this screen contains yield stress, which is equal to (220 N/mm2), and ultimate tensile stress which is equal to (350 N/mm2). and draw ratio for first draw, first redraw with annealing , and first

redraw without annealing ,and their values are as follows (2, 1.7, and 1.3) respectively. The proper lubricant of this type of metal is also displayed in this screen. At this stage data is retrieved form a database file[7].

In Figure (8), the results are as follows; Clearance between punch and die equal to (0.55) mm (1.309*t), die and punch profile radii are equal to (10, 10) mm respectively. Blank diameter here is larger and is equal to (454.31) mm, since the cup is deeper, thus more metal is needed.

In Figure (9), number of draws will be displayed and equal to “Four draws”, since (h/d) ratio which is acceptable and equal to (3.33) is more than (3.0) and less than (4.5).

Cup diameter and height for the first, second, third and fourth draws are (272.58, 190.80, 137.38, 120) mm, and (121.15, 246.93, 385.03, 400) mm respectively.

Figure (10) shows tool geometry and loads will be determined and the blank with diameter (D) that become a completely drawn cup in four stages .Results for the first draw are as follows; punch diameter = (272.58) mm , die diameter = (273.68) mm, punch load = (121.68) KN, blankholder load = (40.56) KN , and total load = (162.24) KN.

Results for the second draw are as follows; punch diameter = (190.80) mm, die diameter = (191.90) mm, punch load = (64.20) KN, blankholder load = (21.40) KN, and total load = (85.60) KN.

Results for the third draw are as follows; punch diameter = (137.38) mm, die diameter = (138.48) mm, punch load = (43.7) KN, blankholder load = (14.56) KN, and total load = (58.26) KN.

Results for the fourth draw are as follows; punch diameter = (120) mm, die diameter = (121.1) mm, punch load = (25.16) KN, blankholder load = (8.38) KN, and total load = (33.55) KN.

By clicking on “Connect to AutoCAD” button, AutoCAD will be automatically launched, and by clicking on “Plot 1st die” and “Plot 2nd die” and “Plot 3rd die” and “Plot 4th die” buttons, first, second, third and fourth deep drawing dies will be plotted directly as shown in Figure (11).

The whole results of the computer-aided design system are listed in details in Table (2). It can be concluded that, if the product (cup) needs more than one stage (draw) to be completely drawn, punch load, blankholder load, total load, and (LDR) will be decreased with subsequent stages.

The developed system showed how to design for deep drawing process which is a time consuming and tedious work can be accomplished automatically. Also it is not violated by human errors; these benefits will be next reflected on the quality of the produced part.

4-2 Finite elements analysis

FE method is used to simulate the drawing operation, the result were compared with experimental results found by (Al-bassam) [1] and the theoretical results found by Mithaq [5].

The maximum punch stroke was set as (55) mm to ensure that the product (cup) is completely drawn. Boundary conditions utilized by FEM were as follows, coefficient of friction (μ) = 0.1, blankholder force (BH. F.) = (15) KN, Poisson ratio (υ) = 0.3, punch speed = 10 mm / min.

To investigate the effect of radial clearance between punch and die on the drawing operation, one punch with profile radius of (15) mm, and with diameter of (120) mm, and four dies with die profile radius of (6) mm , and diameter of (120.9 , 121, 121.1, 121.14) mm. This tool set gave the best drawn cups with less wrinkles and earing experimentally.

the radial clearances were taken as follows: C1= 0.45 mm (107 %), C2 = 0.5 mm (116 %), C3 = 0.55 mm (130.9 %) , and C4 = 0.57 mm (135.7%).

Figure (11) represents the effect of radial clearance on punch load. Both FEM and experimental results are included. It is clear that the punch load increases slightly with the decrease of radial clearance between punch and die. This occur since the gap between punch and die decreases, thus the contacted area between the blank and tools will be larger an the friction higher. Also the Figure shows that experimental loads are higher than FEM loads , this may occur since in the experimental circumstances , the lubricant could be inefficient, and this causes the friction between the blank and tools to be higher.

It is clear that cup thickness remains stationary at the cup bottom. At the next region (under punch profile radius), the thickness decrease, because of stretching applied to this region. At the cup edge, the cup wall thickness has a proportional relation with radial clearance, this is caused by the hoop stress applied to this area and also the gap between punch and die acting to size the blank.

It is clear that the equivalent strain over the cup wall increase with deeper punch movement and the change of radial clearance does not affect the equivalent strain.

The effect of radial clearance seems to be very small using both the experimental method or FEM, since the difference in range of the used clearances is very small, it is difficult to determine the optimum one, thus C3 (1.309 t) can be considered as best clearance.

In the experimental method the optimum die design was concluded depending on normal (thickness) strain, in addition to punch load, while using finite element method in this work, the optimum die design is predicted depending on equivalent (effective) strain and stress which represent the resultant of strain and stress in the normal , radial, and circumferential directions , and this proves that predicting the optimum die design using finite elements methods is accurate than the experimental method.

Optimum die design, using FEM, can be concluded to have a tool set with r_p equal to (10 or 15) mm , and r_d equal to (6 or 10) mm, and clearance of (0.55) mm (130.9 % t), and this gives a good match with the experimental results.

5- Conclusions

- It has been observed that the computer – aided deep drawing design system aids designers in providing an automated easy tool for working faster and more accurate.; these benefits will be next reflected on the quality of the produced part.
- If the product (cup) need more than one stage (draw) to be completely drawn, punch load, blankholder load, total load, and (LDR) will decreased with subsequent stages.
- It was concluded, using FEM, that it is possible to produce successful cups.
- Finite elements method is more accurate than the experimental method in predicting the best die design the experimental method ,since predicting of best die design, using FEM, as show in Figure (12)

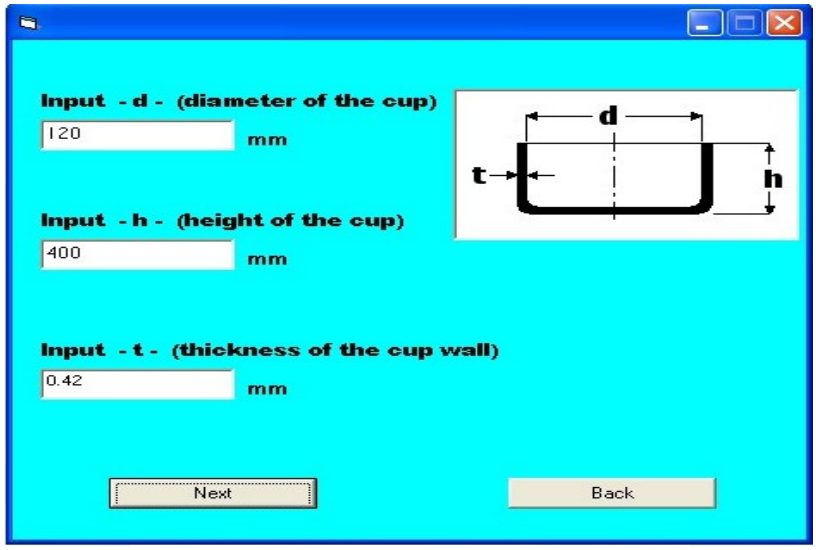

Figure (6). Cup geometry screen.

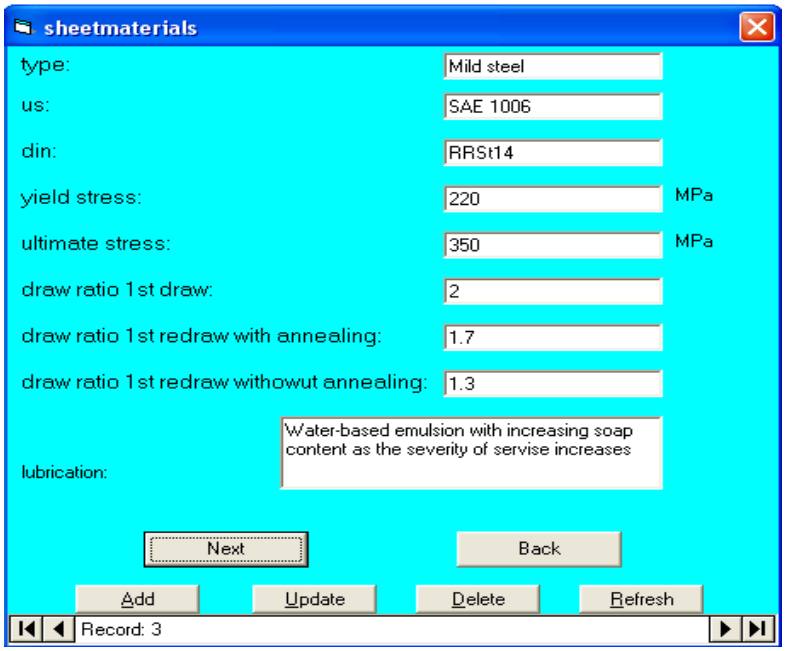

Figure (7). Blank metal properties screen.

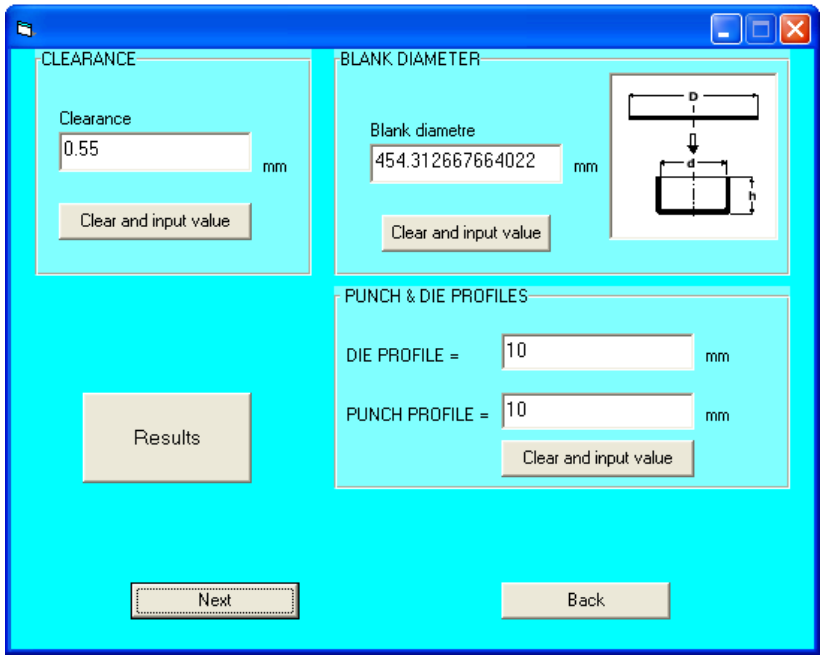

Figure (8). Blank diameter and tool geometry.

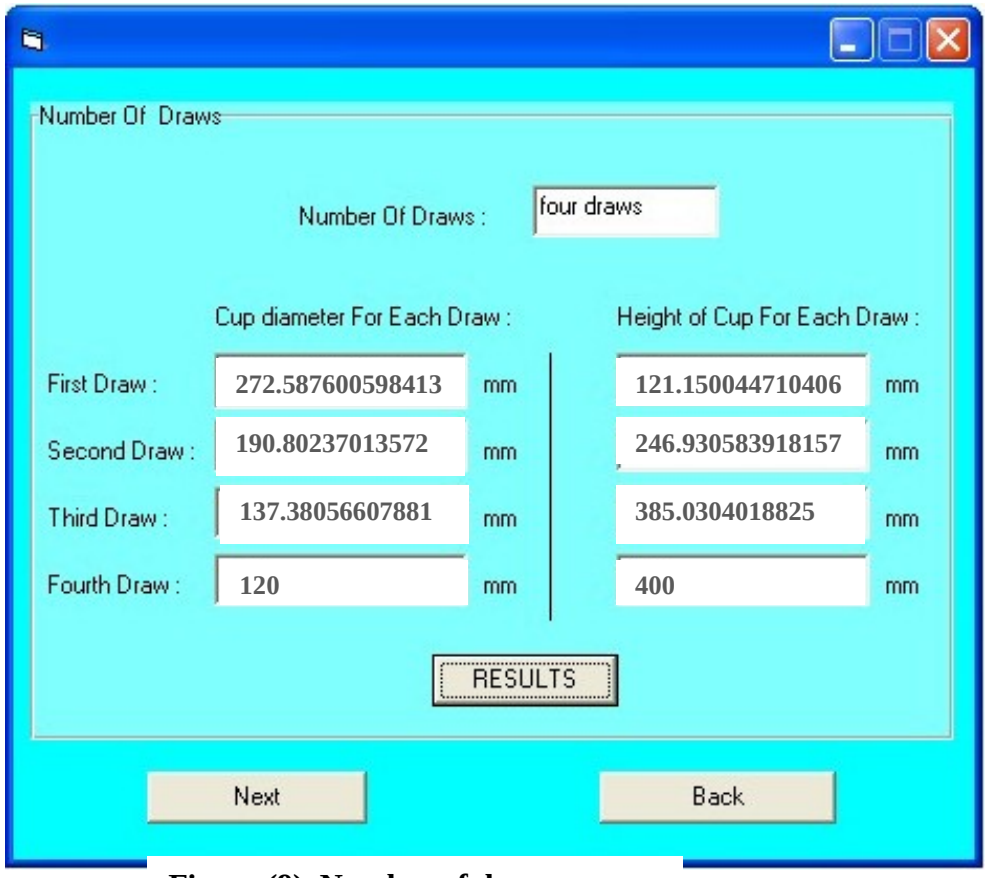

Figure (9). Number of draws screen.

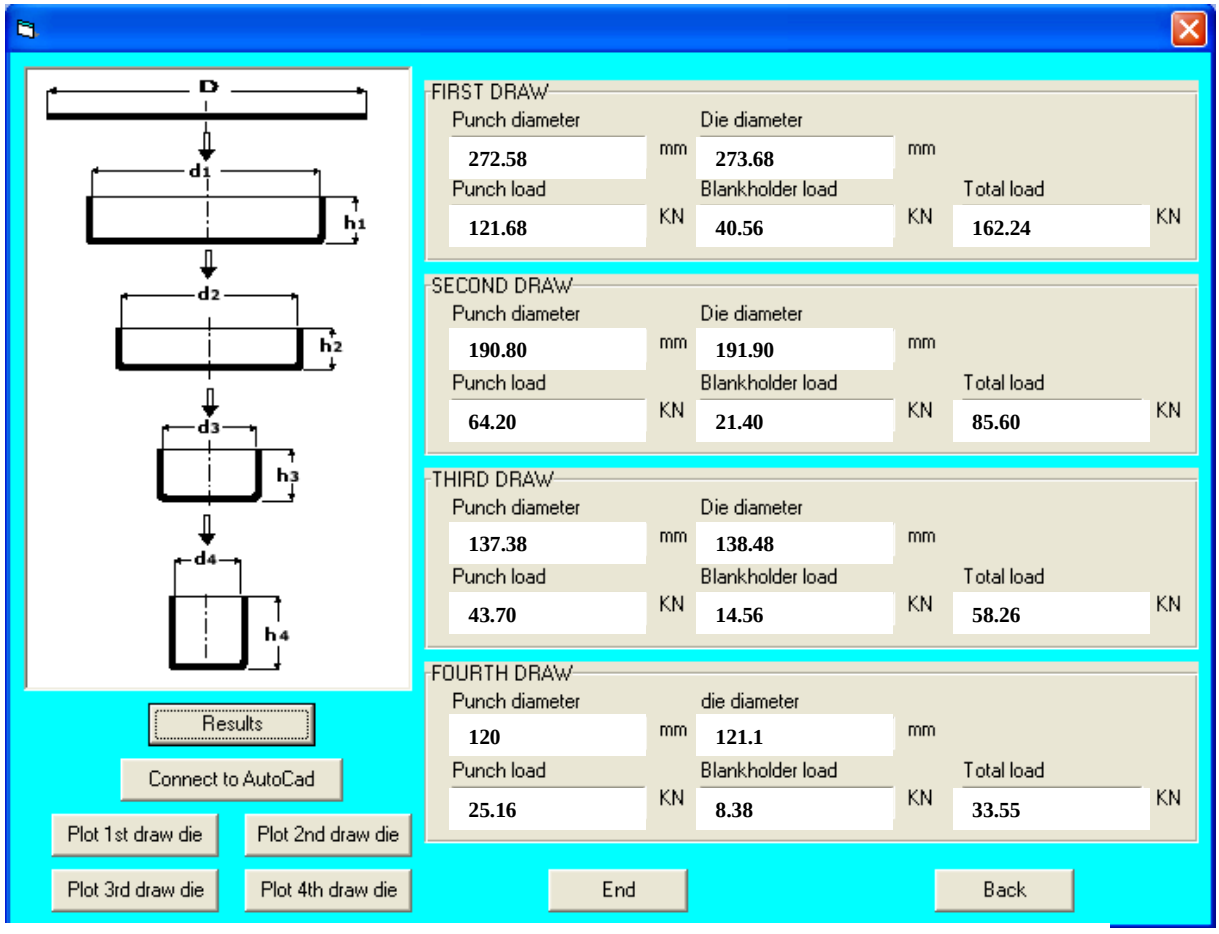

Figure (10). Tool geometry, load, connection to AutoCAD, and auto plot screen.

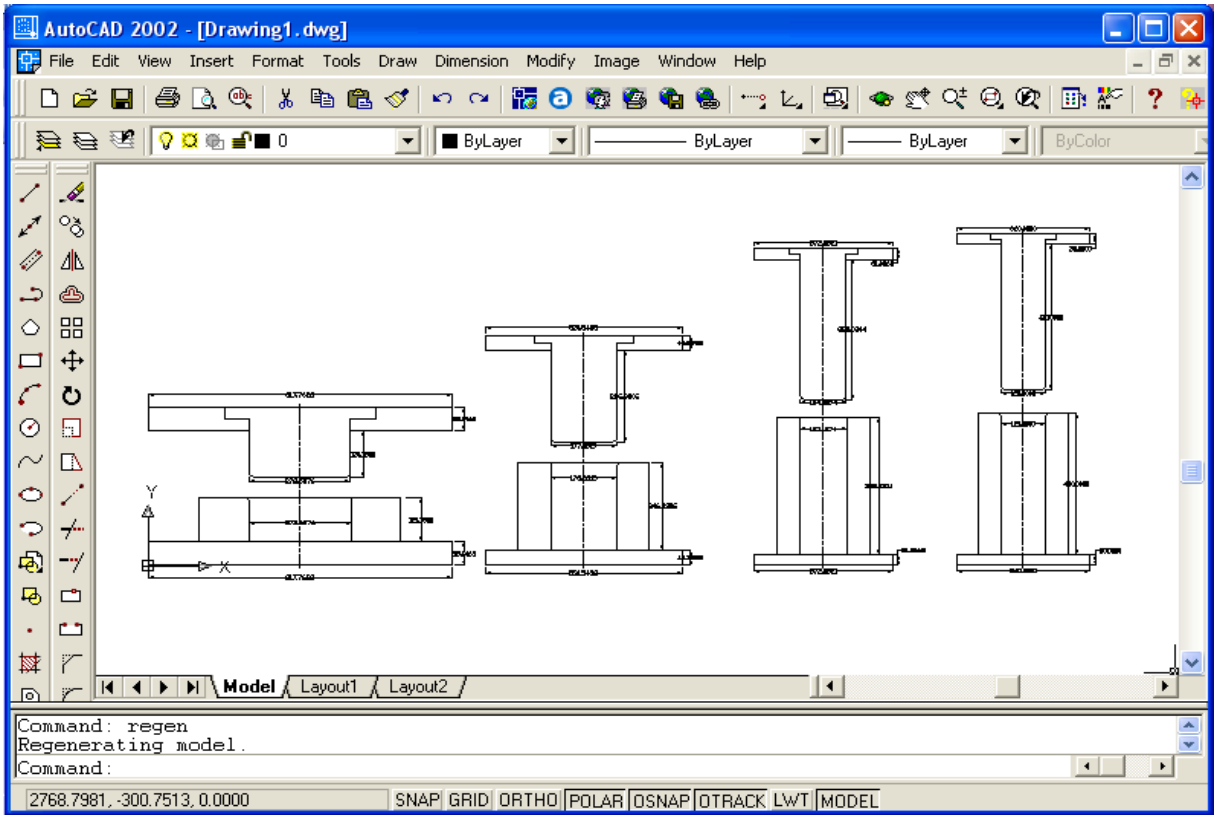

Figure (11). Deep drawing die(s) screen (four draws).

Table (2). Results of the computer-aided design system.

	First draw	second draw	Third draw	Fourth draw
Blank diameter (mm)	454.31	454.31	454.31	454.31
Cup diameter (mm)	120	120	120	120
Cup height (mm)	400	400	400	400
Cup thickness (mm)	0.42	0.42	0.42	0.42
Clearance (mm)	0.55	0.55	0.55	0.55
Die profile radius	10	10	10	10
Punch profile radius	10	10	10	10
Cup diameter (mm)	272.58	190.80	137.38	120
Cup height (mm)	121.15	246.93	385.03	400
Die diameter (mm)	273.68	191.90	138.48	121.1
Punch Load (KN)	121.68	64.20	43.70	25.16
B. H. Load (KN)	40.56	21.40	14.56	8.38
Total Load (KN)	162.24	85.60	58.26	33.55

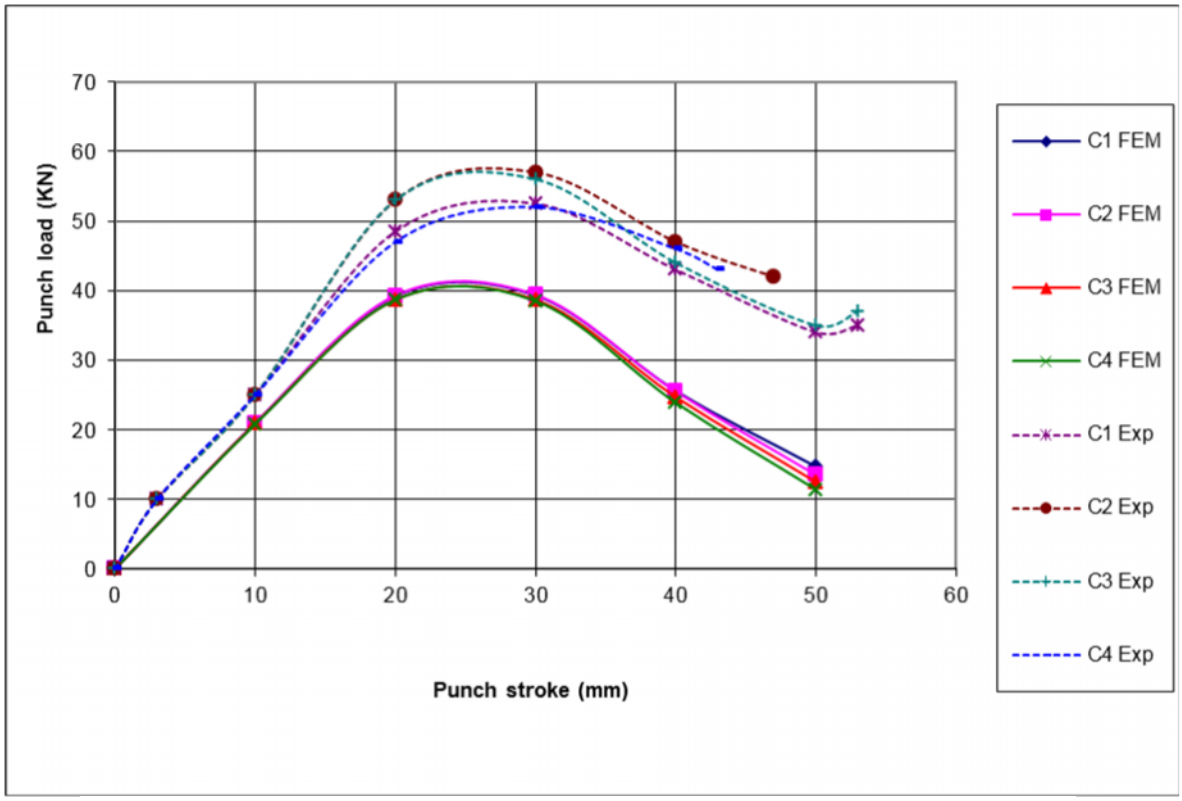

Figure (12). The effect of radial clearance on punch load (p15 d6).

6- References

[1] T. Cwiekala, A. Brosins, A. E. Tekkaya, "Accurate Deep Drawing Simulation by Combining Analytical Approaches" International Journal of Mechanical science,2011

[2] Al-Bassam F. A., “Study of the Effect of Some Parameters on Deep – Drawing Process”, M.Sc. Thesis, University Of Technology, 1983.

[3] Joseph C. D., “Experimental Measurement And Finite Element Simulation Of Springback In Stamping Aluminum Alloy Sheets For Auto-Body Panel Application”, M. Sc. Thesis, Mississippi State University, 2003.

[4] Al-Samaraey W. K., “Studying The Effect of Die Geometry on Deep Drawing Operation using Finite Element Method”, Ph.D. Thesis, University of Technology, 2003.

[5] ANSYS 5.4 Structural Analysis Guide", third edition.

[6] Mithaq Elias Hanno “Computer – Aided Design and Simulation of Deep Drawing Operation”, Ph.D Thesis, University of Technology, 2003.

[7] Lang k., "Handbook of Metal Forming ",McGraw Hill, 1985.

Reduction of Separation Distance in MIMO Systems Using Polarization Diversity

A. S. Ghazi

College of Engineering

Thi-Qar University

Abstract

One of the promising techniques in communication systems is the Multiple Input – Multiple Output (MIMO) systems. The aim of these systems is increasing channel capacity, and the main problem in these systems is the required separation distance between antennas which must be greater than or equal to half wavelength. Satisfying this separation distance is difficult especially at low frequencies. In this paper we study the ability to reduce the total separation distance by using polarization diversity. Each two adjacent antenna are replaced by one dual polarized antenna. The obtained results show that the use of polarization diversity will reduce the required separation distance and the performance of the system will be better than that of classical system (without polarization diversity). This improvement is more useful at the system with greater number of antennas. Increasing the correlation between antennas due to the separation angle will reduce the channel capacity. The results also show that increasing the cross polarization discrimination XPD will increase channel capacity at low level of signal to noise ratio (SNR) and decrease it at high level of it if the attenuation for horizontally polarized signal is the same as that for vertically polarized signal (CPF=0), but if ($CPF \neq 0$) then low values of XPD will improve channel capacity especially at high level of SNR. The results also prove that channel capacity inversely proportional with CPF at rural area ($XPD \neq 0$), and when XPD=0 (urban area) the channel capacity linearly proportion with CPF at high level of SNR, and inversely proportional with CPF at low level of it.

Keywords: MIMO, Multiple antenna systems, Polarization diversity, Channel capacity.

تقليل المسافة الفاصلة في النظم متعددة الهوائيات باستخدام تنوع الاستقطاب

أمين شريف غازي

كلية الهندسة ،جامعة ذي قار

المستخلص

تعتبر النظم متعددة الادخل- متعددة الاخراج واحدة من النظم او التقنيات الواعده في مجال الاتصالات وهدفها الاساسي هو زيادة سعة قناة الاتصال وبالتالي جودته. لكن المشكلة الاساسية في هذه النظم هي مسألة المسافات الفاصلة بين الهوائيات

والتي يجب ان تكون اكبر او مساوية لنصف طول الموجة. ان تحقيق مسافات فاصلة بهذا المقدار امر صعب وخاصة عند الترددات الواطئة، لذلك درسنا في هذا البحث امكانية استبدال كل هوائيين متجاورين بهوائي واحد ثنائي الاستقطاب وفي هذه الحالة تقل المسافة الفاصلة المطلوبة لمصفوفة الهوائيات كاملة. وقد اظهرت النتائج ان لستخدام تنوع الاستقطاب امر مفيد في تحسين الاداء ومقدار هذا التحسين يكون اكبر في النظم ذات عدد الهوائيات الاكبر. تعمل الزيادة في مقدار الترابط بين الهوائيات نتيجة لزوايا الاستقطاب على تقليل سعةالقناة. كما ان زيادة نسبة تغير الاستقطاب تؤدي الى تحسين سعة القناة عند المستويات القليلة من نسبة الاشارة الى الضوضاء وتسئ السعة عند المستويات العالية منها اذا كان التوهين الذي تعانيه الموجة المستقطبة أفقيا مشابه لما تعانيه الموجة المستقطبة عموديا ,أما إذا كان التوهين الذي تعانيه الموجة المستقطبة أفقيا اكبر من التوهين الذي تعانيه الموجة المستقطبة عموديا فان تقليل نسبة تغير الاستقطاب يؤدي إلى تحسين سعة القناة وخاصة عند المستويات العالية من نسبة الإشارة إلى الضوضاء. وبينت النتائج أن العلاقة بين سعة القناة ونسبة التوهين الأفقي إلى العمودي هي علاقة عكسية في المناطق الريفية ,أما في المناطق المزدحمة فان العلاقة بين سعة القناة ونسبة التوهين الأفقي إلى العمودي هي علاقة طردية عند المستويات العالية من نسبة الإشارة إلى الضوضاء وعكسية عند المستويات القليلة منها.

1. Introduction

The use of antenna array at both ends of a wireless link(MIMO technology) has recently been shown to have the potential to drastically increase spectral efficiency through a technique known as spatial multiplexing [1-5].This leverage often referred to as multiplexing gain permits the opening of multiple spatial pipes between transmitter and receiver within the frequency band of operation for no additional power expenditure leading to a linear(in the number of antennas) increase in capacity [6-9].But these antennas are required a separation distance greater than half wavelength. The cost of increasing spatial dimensions at the base station and the mobile terminal especially at low frequencies has been an impediment to the deployment of spatial diversity in practical systems [9].

Polarization diversity provides an alternative means of increasing the diversity order with little increase in spatial dimensions [10, 11].Recent researchs in multiple antennas systems aims to reduce the spatial dimensions without degrade system performance. One of these solutions is the use of multiple polarized antennas, so this paper aimed to study the effect of many polarization factors on systems performance. These factors include: cross-polarization discrimination (XPD), co-polarized factor (CPF), and polarization separation angles at transmitter and receiver side. The rest of this paper organized as follows: section 2 introduces the channel model and states our assumptions, section 3 provides the simulation results at different conditions, section 4 states the discussion and conclusion, and finally section 5 list the references.

2. Channel model

In linear antenna system shown in Figure(1a), the relation between transmitter and receiver is govern by the following equation[12]:

$$Y = HX + n \tag{1}$$

Where Y is $N_R \times 1$ received vector, X is $N_T \times 1$ transmitted vector, H is $N_R \times N_T$ channel matrix, n is $N_R \times 1$ vector of additive white Gaussian noise, N_T is the number of antennas at transmitter side, and N_R is the number of antennas at receiver side.

The channel capacity in multiple antennas system is given by the following equation [13]:

$$C = Log_2 \left| I_{N_R} + \frac{SNR}{N_T} \times HH^* \right| \quad \text{b/s/Hz} \quad \text{(bit/second/hertz)} \tag{2}$$

Where I_{N_R} is $N_R \times N_R$ identity matrix, SNR is the signal to noise ratio at the receiver side, and H^* is the complex conjugate transpose of the channel matrix H. As we see from the above equation the channel capacity depend on many factors, the most important factor is the channel matrix. The channel matrix also depends on many factors. The most important one is the separation distance, if we refer to the separation distance at the transmitter side by d_t, and refer to the separation distance at the receiver side by d_r, then we need $(N_T - 1)d_t$ separation distance at the transmitter side, and $(N_R - 1)d_r$ separation distance at the receiver side. If we assume that $d_t = d_r = d_{sep}$ and $N_T = N_R = N$, then the separation distance will be $(N-1)d_{sep}$ at both side (without polarization diversity). We study two cases: 2×2 case and 4×4 case in the present and absent of polarization diversity.

2.1 Case 2×2 :consider the system shown in Figure(1). In the presence of polarization diversity the channel matrix can be separated into three components:

$$H = H_T H_{CH} H_R \tag{3}$$

Where H_T is the transmitter component for the channel matrix, H_R is the receiver component for the channel matrix, and H_{CH} is the channel component for the channel matrix,

$$H_T = \begin{bmatrix} 1-\alpha_T & \alpha_T \\ \alpha_T & 1-\alpha_T \end{bmatrix} \tag{4}$$

Where α_T is the cosine of the minimum angle between the vertically polarized and the horizontally polarized antenna at the transmitter side.

$$H_R = \begin{bmatrix} 1-\alpha_R & \alpha_R \\ \alpha_R & 1-\alpha_R \end{bmatrix} \quad (5)$$

where α_R is the cosine of the minimum angle between the vertically polarized and the horizontally polarized antenna at the receiver side.

$$H_{CH} = \begin{bmatrix} h_{vv} & h_{vh} \\ h_{hv} & h_{hh} \end{bmatrix} \quad (6)$$

where h_{vv} is the relation between the vertically polarized receiver antenna with the vertically polarized transmitter antenna, h_{hh} is the relation between the horizontally polarized receiver antenna with the horizontally polarized transmitter antenna, h_{vh} is the relation between the vertically polarized receiver antenna with the horizontally polarized transmitter antenna, and h_{hv} is the relation between the horizontally polarized receiver antenna with the vertically polarized transmitter antenna.

The polarization of the transmitted signal will change due to the scattering, diffraction, and reflection .The cross polarization discrimination (XPD) is define as the average cross-coupled (vh,hv) power relative to the co-polarized(vv,hh)power[14]. XPD is produced due to the depolarization of the transmitted signal by scattering , diffraction , and reflection in the channel [11].The horizontally polarized signal will attenuated more than the vertically polarized signal and the ratio between these attenuation is co-power factor (CPF),the value of CPF between 0-15dB[15]. For these assumption the H_{CH} matrix will be as follow

$$H_{CH} = \begin{bmatrix} h_{vv} & h_{vh} \\ h_{hv} & h_{hh} \end{bmatrix} = h_{vv} \begin{bmatrix} 1 & xpd \\ xpd & cpf \end{bmatrix} \quad (7)$$

where $xpd = Log^{-1} \dfrac{-XPD}{10}$

and

$$cpf = Log^{-1} \frac{-CPF}{10}$$

hence

$$H = \begin{bmatrix} 1-\alpha_T & \alpha_T \\ \alpha_T & 1-\alpha_T \end{bmatrix} * h_{vv} \begin{bmatrix} 1 & xpd \\ xpd & cpf \end{bmatrix} * \begin{bmatrix} 1-\alpha_R & \alpha_R \\ \alpha_R & 1-\alpha_R \end{bmatrix} \quad (8)$$

if we assume $\alpha_T = \alpha_R = \alpha$,then

$$H = \begin{bmatrix} 1-\alpha & \alpha \\ \alpha & 1-\alpha \end{bmatrix} * h_{vv} \begin{bmatrix} 1 & xpd \\ xpd & cpf \end{bmatrix} * \begin{bmatrix} 1-\alpha & \alpha \\ \alpha & 1-\alpha \end{bmatrix} \quad (9)$$

This equation represents the channel matrix for **2×2** antenna system in the present of polarization. There isn't any need to the separation distance for **2×2** system in the present of polarization [d_{sep}=0]. While the separation distance for **2×2** system in the absent of polarization is d_{sep} which must be greater than or equal to half wavelength. The channel matrix for **2×2** system in the absent of polarization is:

$$H = H_{CH} = \begin{bmatrix} h_{11} & h_{12} \\ h_{21} & h_{22} \end{bmatrix} \tag{10}$$

where h_{ij} represent the relation between the i^{th} receiver antenna and j^{th} transmitter antenna.

2.2 Case 4×4: In the same way that illustrated in section 2.1, we get:

$$H_T = \begin{bmatrix} 1-\alpha_T & \alpha_T & 0 & 0 \\ \alpha_T & 1-\alpha_T & 0 & 0 \\ 0 & 0 & 1-\alpha_T & \alpha_T \\ 0 & 0 & \alpha_T & 1-\alpha_T \end{bmatrix} \tag{11}$$

$$H_R = \begin{bmatrix} 1-\alpha_R & \alpha_R & 0 & 0 \\ \alpha_R & 1-\alpha_R & 0 & 0 \\ 0 & 0 & 1-\alpha_R & \alpha_R \\ 0 & 0 & \alpha_R & 1-\alpha_R \end{bmatrix} \tag{12}$$

$$H_{CH} = \begin{bmatrix} h_{11} & h_{11}*xpd & h_{12} & h_{12}*xpd \\ h_{11}*xpd & h_{11}*cpf & h_{12}*xpd & h_{12} \\ h_{21} & h_{21}*xpd & h_{22} & h_{22}*xpd \\ h_{21}*xpd & h_{21} & h_{22}*xpd & h_{22}*cpf \end{bmatrix} \tag{13}$$

Substitute Eqs.(11-13) in (3)to get:

$$H = \begin{bmatrix} 1-\alpha_T & \alpha_T & 0 & 0 \\ \alpha_T & 1-\alpha_T & 0 & 0 \\ 0 & 0 & 1-\alpha_T & \alpha_T \\ 0 & 0 & \alpha_T & 1-\alpha_T \end{bmatrix} * \begin{bmatrix} h_{11} & h_{11}*xpd & h_{12} & h_{12}*xpd \\ h_{11}*xpd & h_{11}*cpf & h_{12}*xpd & h_{12} \\ h_{21} & h_{21}*xpd & h_{22} & h_{22}*xpd \\ h_{21}*xpd & h_{21} & h_{22}*xpd & h_{22}*cpf \end{bmatrix} * \begin{bmatrix} 1-\alpha_R & \alpha_R & 0 & 0 \\ \alpha_R & 1-\alpha_R & 0 & 0 \\ 0 & 0 & 1-\alpha_R & \alpha_R \\ 0 & 0 & \alpha_R & 1-\alpha_R \end{bmatrix} \tag{14}$$

If $\alpha_T = \alpha_R = \alpha$ then

$$H = \begin{bmatrix} 1-\alpha & \alpha & 0 & 0 \\ \alpha & 1-\alpha & 0 & 0 \\ 0 & 0 & 1-\alpha & \alpha \\ 0 & 0 & \alpha & 1-\alpha \end{bmatrix} * \begin{bmatrix} h_{11} & h_{11}*xpd & h_{12} & h_{12}*xpd \\ h_{11}*xpd & h_{11}*cpf & h_{12}*xpd & h_{12} \\ h_{21} & h_{21}*xpd & h_{22} & h_{22}*xpd \\ h_{21}*xpd & h_{21} & h_{22}*xpd & h_{22}*cpf \end{bmatrix} * \begin{bmatrix} 1-\alpha & \alpha & 0 & 0 \\ \alpha & 1-\alpha & 0 & 0 \\ 0 & 0 & 1-\alpha & \alpha \\ 0 & 0 & \alpha & 1-\alpha \end{bmatrix} \tag{15}$$

This matrix represent the channel matrix for 4×4 MIMO system where each two adjacent antenna are replaced by one dual polarized antenna and the total separation distance will be

$(\frac{N}{2}-1)d_{sep} = d_{sep}$ instead of $3d_{sep}$ (without polarization diversity). The channel matrix for **4**$\times$**4** system in the absent of polarization is:

$$H = H_{CH} = \begin{bmatrix} h_{11} & h_{12} & h_{13} & h_{14} \\ h_{21} & h_{22} & h_{23} & h_{24} \\ h_{31} & h_{32} & h_{33} & h_{34} \\ h_{41} & h_{42} & h_{43} & h_{44} \end{bmatrix} \quad (16)$$

where h_{ij} represent the relation between the i^{th} receiver antenna and j^{th} transmitter antenna.

3. Simulation and results

After we derive a useful expressions for the channel matrix for 2×2 and 4×4 cases as a function of polarization factors (XPD,CPF,α).We substitute these expressions in the channel capacity equation (eq.2) for the two cases .We use IEEE802.11F program to generate Rayleigh fading channel matrix coefficients h_{vv}, h_{11}, h_{12}, h_{21}, h_{22} and substitute these coefficients in channel capacity equation. After that we draw the channel capacity at different conditions. The obtained results show that the use of polarization diversity will reduce the separation distance between antennas, and at the same conditions the performance of the systems with polarization better than the systems without polarization as shown in Figure(2)for 4×4 case. If the separation angle θ between antennas become less than 90^0 (not right angle)the separation correlation coefficient α (α=cosθ)will increase and the channel capacity decrease as α increase in transmitter and /or receiver side as shown in Figures(3-4).If we increase the cross polarization discrimination (XPD) ,the channel capacity will improve at low level of signal to noise ratio (SNR)and disprove at high level of SNR if the attenuation for horizontally polarized signal is the same as for vertically polarized signal(CPF=0).But if the ($CPF \neq 0$) then reduce the value of XPD will improve the channel capacity for all values of SNR specially at high level of it as shown in Figures(5-10).To study the effect of co-polarization factor (CPF) we make correlation angle θ constant at right angle so that α=0,XPD constant, and vary the CPF. The obtained results show that the channel capacity inversely proportional with CPF at rural area ($XPD \neq 0$) for all values of SNR. While in urban areas (XPD=0)the channel capacity increase as CPF increase at high level of SNR and decrease as CPF increase at low level of SNR for all systems as shown in Figures(11-14).

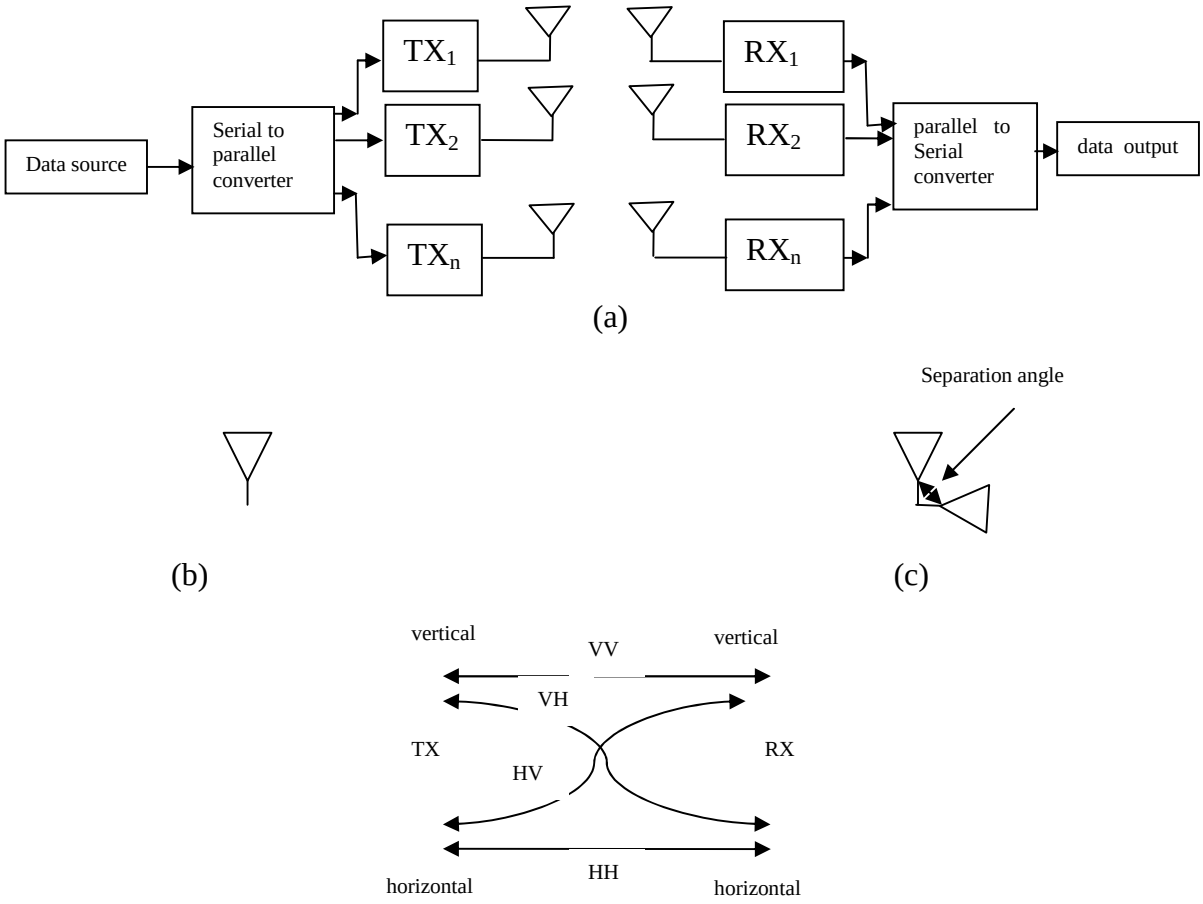

Figure(1).(a) spatial multiplexing system,(b) vertically polarized antenna,(c) dual polarized antenna , (d)schematic plot of the transmission link between transmitter and receiver indicate the components of the polarization matrix .

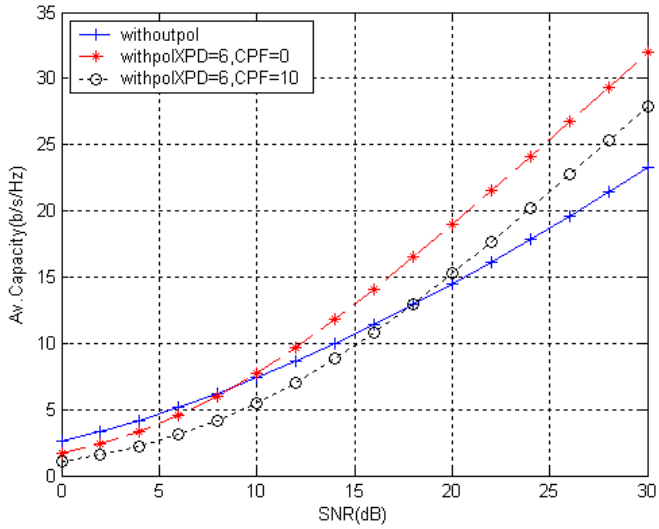

Figure(2).Channel capacity vs SNR for 4×4 system in the present and absent of polarization.

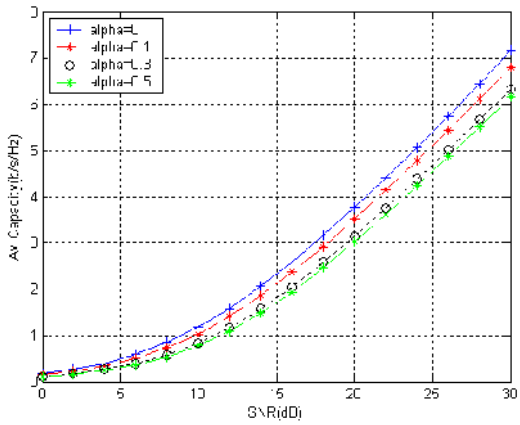

Figure(3).Channel capacity vs SNR for 2×2 system when XPD=6dB,CPF=10dB.

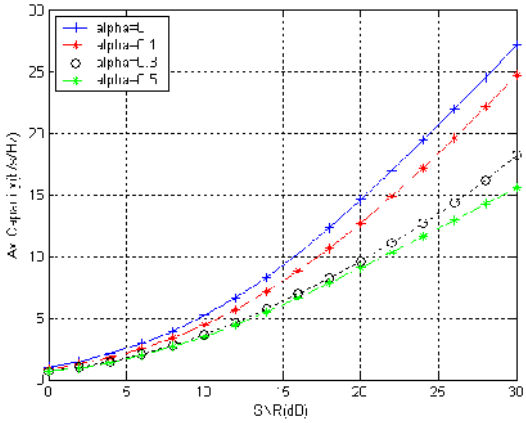

Figure(4).Channel capacity vs SNR for 4×4 system when XPD=6dB,CPF=10dB.

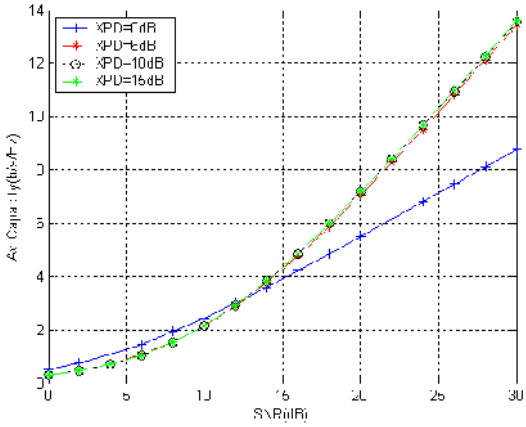

Figure(5).Channel capacity vs SNR for 2×2 system when CPF=0dB,α=0.

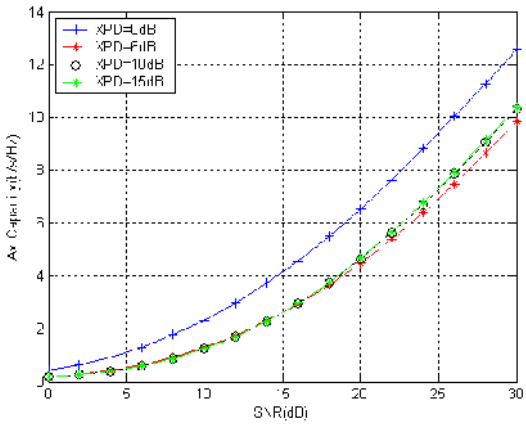

Figure(6).Channel capacity vs SNR for 2×2 system when CPF=5dB,α=0.

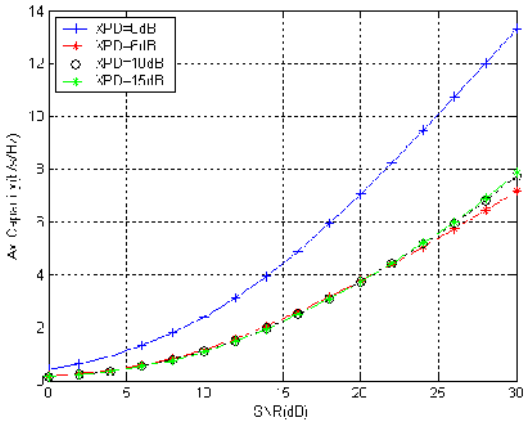

Figure(7).Channel capacity vs SNR for 2×2 system when CPF=10dB,α=0.

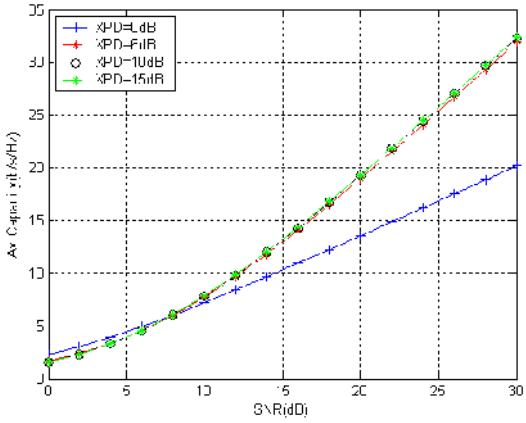

Figure(8).Channel capacity vs SNR for 4×4 system when CPF=0dB,α=0.

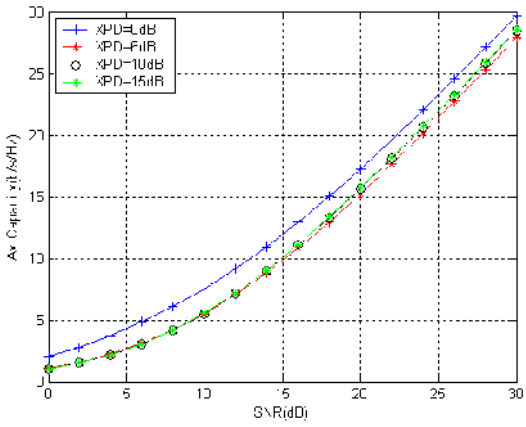

Figure(9).Channel capacity vs SNR for 4×4 system when CPF=5dB,α=0.

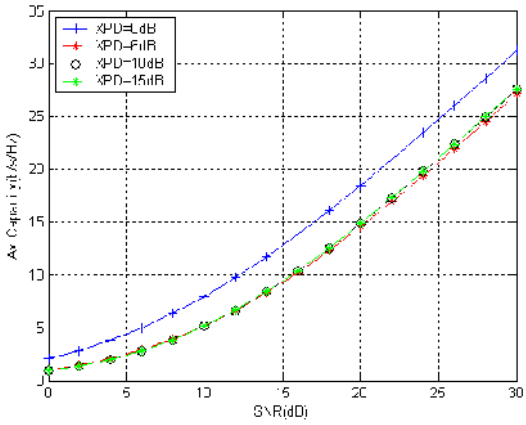

Figure(10).Channel capacity vs SNR for 4×4 system when CPF=10dB,α=0.

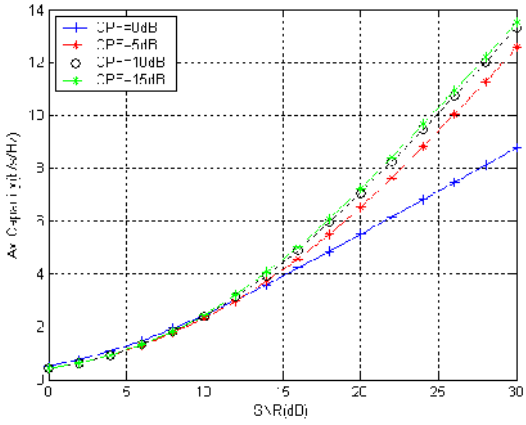

Figure(11).Channel capacity vs SNR for 2×2 system when XPD=0dB,α=0.

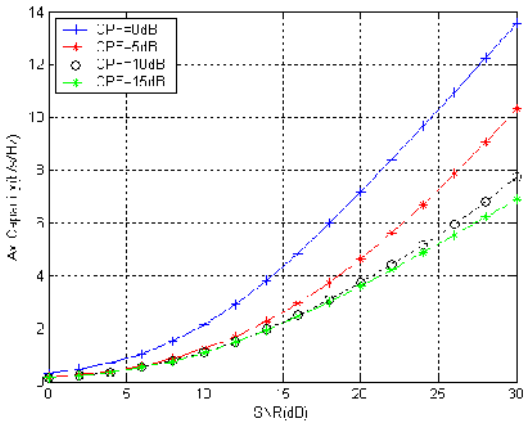

Figure(12).Channel capacity vs SNR for 2×2 system when XPD=10dB,α=0.

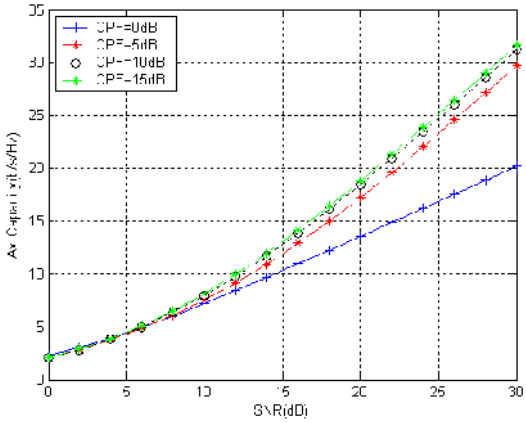

Figure(13).Channel capacity vs SNR for 4×4 system when XPD=0dB,α=0.

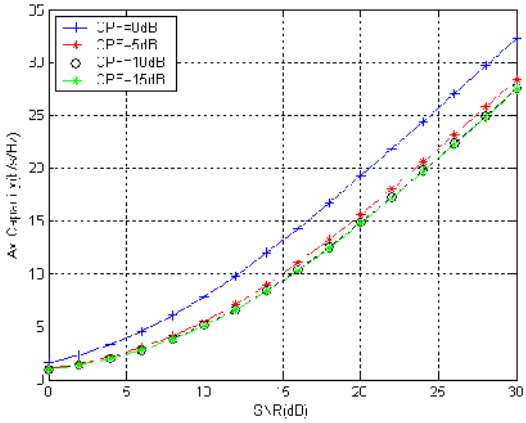

Figure(14).Channel capacity vs SNR for 4×4 system when XPD=10dB,α=0.

4. Discussion and conclusion

One of the main problems in multiple antenna system is the separation distance between antennas. By using dual polarized antenna we can make the total separation distance as $(\frac{N}{2}-1)d_{sep}$ instead of $(N-1)d_{sep}$ in non polarized state(without using polarization diversity). Without using dual polarized antenna we cannot decrease the separation distance to less than half wavelength because of the correlation between the antennas. If we can reduce the correlation between antennas, we can reduce the separation distance to small value (lower than half wavelength). We suggest that each antenna in MIMO system replaced by an endfire array of antenna i.e. the MIMO system translate from linear to planar antenna array, but each row of antenna represent one antenna with certain radiation pattern. In this case we may be able to reduce the correlation between the antennas and then reduce the separation distance.

5. References

[1] A.J. Paulraj and T.Kailath, "**Increasing Capacity in Wireless Broadcast Systems using Distributed Transmission/Directional Reception**", U.S. Patent No.5,345 599,1994.

[2] G.J. Foschini, "**Layered Space–Time Architecture for Wireless communication in a Fading Environment when using Multi-element Antennas** ", Bell Laboratories Technical Journal, pp.41-59,Autumn,1996.

[3] I.E.Teletar, "**Capacity of Multi-antenna Gaussian Channels**", European Transaction on Telecommunication, Vol.10,No.6,pp.585-595 , November /December, 1999.

[4] G.G. Raleigh and J.M. Cioffi, "**Spatio-Temporal Coding for Wireless Communications**", IEEE Transaction on Communications,Vol.46,pp.357-366, March, 1998

[5] H. Bolcskei, D. Gesbert , and A.J. Paulraj "**On the Capacity of OFDM-based Spatial Multiplexing Systems**", IEEE Transaction on Communications ,Vol.50 , pp.225-234,February, 2002.

[6] N.Seshadri and J.Winters ,"**Two Signaling Scheme for Improving the Error Performance of Frequency-Division-Duplex (FDD) Transmission Systems using Transmitter Antenna Diversity**", International Journal on Wireless Information Networks,Vol.1, No.1, pp.49-60, January,1994.

[7] J.Guey, M. Fitz, M. Bell, and W. Kuo ,"**Signal Design for Transmitter Diversity Wireless Communication Systems Over Rayleigh Fading Channels** ", IEEE Transaction on Vehicular Technology and Conference,Vol.1, pp.136-140, April/ May,1996.

[8] V.Tarokh , N.Seshadri ,and A.R. Calderbank ,"**Space-Time Code for High Data Rates Wireless Communication:Performance Criterion and Code Construction**", IEEE Transaction on Information Theory,Vol.44,pp.744-765,March,1998.

[9] V.Tarokh, H. Jafarkhani, and A.R. Calderbank, "**Space-Time Code for Orthogonal Design**", IEEE Transaction on Information Theory,Vol.45, pp.1456-1467, July,1999.

[10] R.Visoz and E.Bejjani, "**Matched Filter Bound for Multichannel Diversity over Frequency-Selective Rayleigh-Fading Mobile Channels** ", IEEE Transaction on Vehicular Technology ,Vol.49, No.5, pp.1832-1845, September, 2000.

[11] R.G.Vaughan, "**Polarization Diversity in Mobile Communications**" IEEE Transaction on Vehicular Technology ,Vol.39, No.3, pp.177-186, August,1990.

[12] R.U.Nabar, H. Bolcskei, V.Erceg, D. Gesbert, and A.J. Paulraj ,"**Performance of Multiantenna Signaling Techniques in the Presence of Polarization Diversity**", IEEE Transaction on Signal Processing ,Vol.50, No.10,pp.2553-2562, October, 2002.

[13] L.Dong, H.Choo, R.W.Heath, and H.Ling, "**Simulation of MIMO Channel Capacity with Antenna Polarization Diversity**", IEEE Transaction on Wireless Communications,Vol.4, No.4, pp.1869-1873, July,2005.

[14] T.Neubar and P.C.F.Eggers ,"**Simultaneous Characterization of Polarization Diversity Matrix Components in Pico Cells**", IEEE Transaction on Vehicular Technology and Conference,Vol.3 , pp.1361-1365, Autumn ,1999.

[15] J.V.M.Halim ,H.El-badawy, and H.M.El-Hennawy ,"**Design and Performance of Adaptive Polarized MIMO–MC-SS-CDMA System for Downlink Mobile Communication** ", Proceedings of World Academy of Science, Engineering and Technology,Vol.31, pp.50-557, July, 2008

Shape Function Analysis of Three Dimensional Pre-Tensioned Spherical Dome

Kadhim Karim Mohsen

Mechanical Engineering Department
College of engineering
Thi-Qar University

Abstract

Predicting the shape function of a pre-tensioned spherical dome is very important for the safety of a dome structures design and performance under cyclic loading. This paper presents a new shape function mathematical model which is proposed for use with three dimensional pre-tensioned spherical dome that should provide for a more accurate stresses. The new model is proposed based on an improved Airy stress function principle; to retain objectivity of the results for three dimensional pre-tensioned spherical dome. This model is adopted in this study for its simplicity and computational efficiency. The objective of this work is to analyze the response and to describe the behavior of pre-tensioning dome structure under loading. The model provides a very powerful tool for the solution of many problems in elasticity; such applications include tensor analysis of the stresses and strains. Correlation between the proposed model with experimental studies results of pre-tensioned specimens are conducted and show a reasonable agreement. The results are drawn as to the applicability of this approach. Stresses within dome surface are constant and the shear stress is zero when subjected to a hoop stress. The maximum stress occurs at the boundary of the dome intersecting the y-axis and is decreased along the boundary of the disc as it nears the x-axis. The maximum compressive stress occurs at the boundary intersecting with the x-axis and decreases as it nears the z-axis along the interfacing boundary.

Keywords : Airy stress function ,Pre-stressing , Pre-tensioning, Finite-element method, Nonlinear analysis, Slip

المستخلص

ان التنبا لدالة شكل القبة المستديرة التي لها قاعدة دائرية الكروية ثلاثية الابعاد المشدودة مسبقا مهم جدا في التصميم والاداء الامن لهيكل القبة المستديرة تحت ظروف اداء احمال دورية مختلفة. في هذا البحث تم اقتراح نموذج رياضي لدالة شكل جديدة يمكن استخدامها في القبة المستديرة التي لها قاعدة دائرية الكروية ثلاثية الابعاد المشدودة مسبقا والتي يمكن الاستفادة منها لايجاد الاجهادات بدقة اكبر. ان النموذج المقترح يستند على دالة ايري المعدلة للاجهادات للمحافظة على

فعالية ايجاد النتائج للقبة المستديرة التي لها قاعدة دائرية كروية ثلاثي الابعاد مشدود مسبقا وهذا النموذج تم اعتماده في هذه الدراسة لبساطته وكفائتة في ايجاد الحسابات حيث ان الهدف من هذا العمل هو تحليل الاستجابة ووصف سلوك القبة الكروية تحت تاثير الاحمال وهو اداة قوية لحل المسائل في المرونة .تم استخدام اسلوب الموتور في تحليل الاجهادات والانفعالات وان الربط بين نتائج الدراسات العملية وان نتائج النموذج المقترح بينت التوافق المعقول بينهما من خلال رسم النتائج لبيان قابلية الطريقة. الاجهادات داخل سطح القبة الكروية ثابت وإجهاد القص صفرا عندما يتعرض لإجهاد حلقي. ان الضغط الأقصى يحدث في حدود القبة الكروية متقاطعا على المحور الصادي وينخفض على طول الحدود من القرص لأنها تقترب من محورس وان اجهاد الضغط الاقصى يحدث في أقصى الحدود التي تتقاطع مع المحور س وتقل لأنها تقترب من محور ص على طول رابط الحدود.

1. Introduction

Roth and Whitely [1] propose a technology based on tensegrity for tough, rigid, large scale domes that are also economical to construct. The development of a structural technology to economically cover large areas would be useful for warehouses, permanent or temporary protection for archaeological and other vulnerable sites, large-scale electrical or electromagnetic shielding and exclusion or containment of flying animals or other objects. Structures based on such a technology can serve as frameworks in which environmental control, energy transformation and food production facilities could be embedded. The space application is also possible by using self-deployed structures. Summary advantages are improved rigidity, ethereal, resilient, equal-length struts, simple joints.

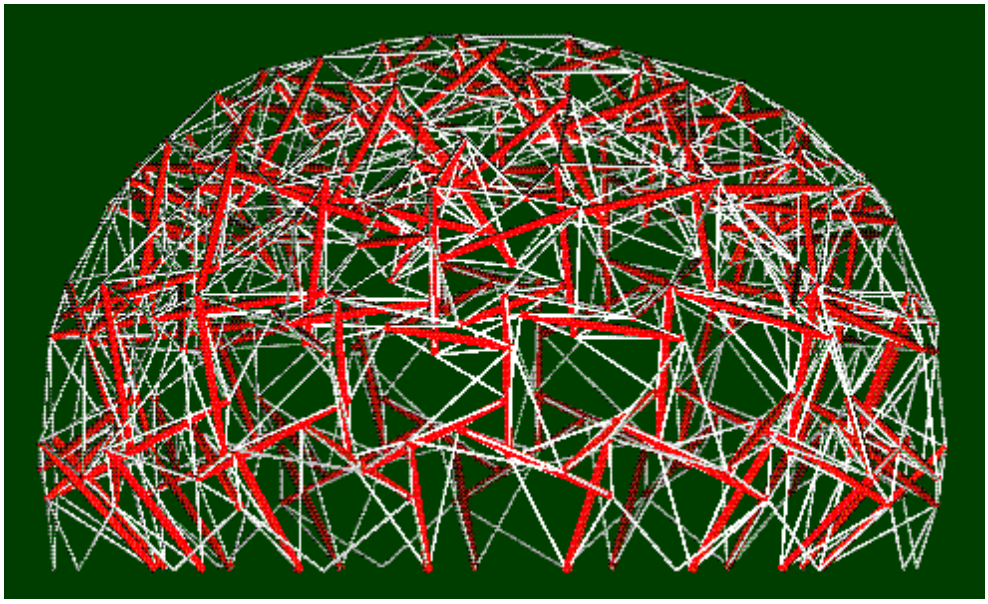

Figure(1). A representation of a dome which utilitizes tensegrity solutions' technology [2].

Predicting the shape function of a pre-tensioned spherical dome is very important for the safety of a dome structures design. In addition, there are growing concerns about the performance dome under loading. Hence, a more realistic evaluation of the dome structure behavior due to cyclic loading is necessary to maintain containment integrity.

Elasticity is an elegant and fascinating subject that deals with the determination of the stress, strain and distribution in an elastic solid under the influence of external forces. A particular form of elasticity which applies to a large range of engineering materials, at least over part of their load range produces deformations which are proportional to the loads producing them, giving rise to the Hooke's Law. The theory establishes mathematical models of a deformation problem, and this requires mathematical knowledge to understand the formulation and solution procedures. The variable theory provides a very powerful tool for the solution of many problems in elasticity. Employing complex variable methods enables many problems to be solved that would be intractable by other schemes. The method is based on the reduction of the elasticity boundary value problem to a formulation in the complex domain. This formulation then allows many powerful mathematical techniques available from the complex variable theory to be applied to the elasticity problem [3].

Material properties must be determined experimentally. Careful examinations of the properties of most structural materials indicate that they are not isotropic or homogeneous. Nonetheless, it is common practice to use the isotropic approximation for most analyses. In the future of structural engineering, however, the use of composite, anisotropic materials will increase significantly. The responsibility of the engineer is to evaluate the errors associated with these approximations by conducting several analyses using different material properties [4].

In the recent years, thin shell structures find wide applications in many branches of technology such as space vehicle, nuclear reactor, pressure vessels, roofs of industrial building and auditoriums. From the point of view of architecture, the development of shell structure offers unexpected possibilities and opportunities for the combined realization of functional, economic and aesthetic aspects studied and tested conical concrete-shell specimens with widely varying material properties and traced their load deformation response, internal stresses and crack propagation through the elastic, inelastic, and ultimate stress ranges [5].

The finding of a structural evaluation of the 5 meter diameter observatory dome structure constructed by Observa-Dome laboratories, Inc. Regarding to the presentation of literature

review, it should be emphasized that no investigation related to the analysis of large concrete thin shell dome is found. So it can be represented this work as a first one in the field of the study of concrete dome. The main objectives of this study are conducting an analytical study on the behavior of reinforced concrete ribbed dome with precast rib and cast-inplace cover and concrete slab under monotonically increasing loads by using three dimensional finite element method of analysis [6].

2. The airy stress function

A stress function is a function from which the stress can be derived at any given point x, y. These stresses then automatically satisfy the equilibrium conditions.

Now let's examine such a stress function. The Airy stress function ϕ is defined by [7]

$$\sigma_x = \frac{\partial^2 \phi}{\partial y^2}, \quad \sigma_y = \frac{\partial^2 \phi}{\partial x^2} \quad \text{and} \quad \tau_{xy} = -\frac{\partial^2 \phi}{\partial x \partial y} \tag{1}$$

One can insert these stresses in the equilibrium conditions (1.1). One then directly see that they are satisfied for every how convenient... However, if one inserts the above definitions into the compatibility condition, we get

$$\frac{\partial^4 \phi}{\partial x^4} + 2\frac{\partial^4 \phi}{\partial x^2 \partial y^2} + \frac{\partial^4 \phi}{\partial y^4} = 0 \quad \text{or} \quad \square^4 \phi = 0 \tag{2}$$

This equation is called the biharmonic equation. It needs to be satisfied by every valid Airy stress function as well.

3. Pre-tensioned structures

Pre-tensioned high strength trusses using alloy steel bar are widely used as glass wall supporting systems because of the high degree of transparency. The breakage of glass panes in this type of system occurs occasionally, likely to be due to error in design and analysis in addition to other factors like glass impurity and stress concentration around opening in a spider system. Most design does not consider the flexibility of supports from finite stiffness of supporting steel or reinforced concrete beams [8]. The resistance of lateral wind pressure of the system makes use of high tension force coupled with the large deflection effect, both of which are affected by many parameters not generally considered in conventional structures. In the design, one must therefore give a careful consideration on various effects, such as support

settlement due to live loads and material creep, temperature change, pre-tension force, and wind pressure. It is not uncommon to see many similar glass wall systems fail in the wind load test chambers under a design wind speed. This paper presents a rigorous analysis and design of this type of structural systems used in a project in Hong Kong, China. The stability function with initial curvature is used in place of the cubic function, which is only accurate for linear analysis. The considerations and analysis techniques are believed to be of value to engineers involved in the design of the structural systems behaving nonlinearly [9].

4. Shape function of three dimensional pre-tensioned spherical dome: A model

In this paper, a prediction of the stresses of the dome structure model is made through various types of numerical modeling, taking in account the appropriate non-linearity for each material. For the nonlinear finite element analysis, the dome is idealized as an axisymmetric model and a three dimensional global model. In order to simulate the actual behavior of the dome, both numerical models are refined by comparison of the results of the two analyses and with the existing research results. Furthermore, more recently developed material models for dome are introduced to the model.

The shape function for three-dimensional pre-tensioned spherical dome logically provides a reasonable stresses estimate. These shape functions are based on an n-order in general approximation, which provides for a non-linear interpolation. For three-dimensional simulation this function offers advantages over the linear shape function currently used in two-dimensional simulations [9]

$$\phi(x,y,z) = A_o + A_1xy + A_2y^2 + A_3x^3 + A_4x^2y + A^5xy^2 + A_6y^3 + A_7x^4 + A_8x^3y + A_9x^2y^2 + A_{10}xy^3 + A_{11}y^4 + A_{12}z + A_{13}xyz + A_{14}xz^2 + \cdots + A_i x^n y^n z^n \quad (3)$$

A_o, A_1, A_2, A_3, A_4, A_5, A_6, A_7, A_8, A_9,… A_i Constants determined from the boundary conditions

Which is satisfy Airy Stress Function (Compatibility condition) equations (1, 2)

5. Tensor analysis

Tensors are geometric objects that describe linear relations between vectors, scalars, and other tensors. Elementary examples include the dot product, the cross product, and linear maps. Vectors and scalars themselves are also tensors. A tensor can be represented as a multi-

dimensional array of numerical values. The order (also degree or rank) of a tensor is the dimensionality of the array needed to represent it, or equivalently, the number of indices needed to label a component of that array. For example, a linear map can be represented by a matrix, a 2-dimensional array, and therefore is a 2nd-order tensor. A vector can be represented as a 1-dimensional array and is a 1st-order tensor. Scalars are single numbers and are zeroth-order tensors.

□= Vector differential operator (Del or Nabla)

Gradient φ = Grad φ =□ φ

Divergence φ =Div φ=□. φ

Curl φ =Rotation φ =Rot φ =□ Xφ

Compatibility of strain tensor

$$□□.\varepsilon_{ij} = □^{t}□.\varepsilon_{ij} - □□e - \Delta\varepsilon_{ij} = 0 \quad (4)$$

and

$$\varepsilon_{ij} = \frac{1+\nu}{E}\sigma_{ij} - \frac{\nu}{E}SI;\ \mathrm{I} = \mathrm{unity}\ ; = \frac{1-2\nu}{E}S \quad (5)$$

Where e=trace of strain, S=trace of stress, $□^{t}$=gradient transpose

Trace of stress

$$S = \sigma_x + \sigma_y + \sigma_z$$

Trace of strain

$$e = \epsilon_x + \epsilon_y + \epsilon_z$$

σ_{ij}= Stress tensor

ε_{ij} =Strain tensor

$$□.\varepsilon_{ij} = \frac{1+\nu}{E}□.\sigma_{ij} - \frac{\nu}{E}□S \quad (6)$$

$$\square e = \frac{1-2\nu}{E}\square S \quad (7)$$

$$\Delta\varepsilon_{ij} = \frac{1+\nu}{E}\Delta\sigma_{ij} \quad (8)$$

$$\square^{T}\square S = \square\square S \quad (9)$$

$$\square\square.\varepsilon_{ij} = \frac{1+\nu}{E}\square\square.S - \frac{\nu}{E}\square\square S \quad (10)$$

$$\square\square e = \frac{1-2\nu}{E}\square\square S \quad (11)$$

$$\square\square.S + \square^{T}\square.S - \Delta\varepsilon_{ij} - \frac{1}{1+\nu}\square\square S + \frac{\nu}{1+\nu}\Delta S.I = 0 \quad (12)$$

$$\sigma_{ik,jk} + \sigma_{jk,ik} - \Delta\sigma_{ij} - \frac{1}{1+\nu}\square\square S + \frac{\nu}{1+\nu}\Delta S.I = 0 \quad (13)$$

From Beltrami

$$\Delta S + \frac{1}{1-\nu}\square.f_i = 0 \quad (14)$$

f_i=body forces

External forces

$$T_{ij} = \sigma_{ij}n_j$$

Tensorial relation

$$\varepsilon_{ij} = \frac{1+\nu}{E}\sigma_{ij} - \frac{\nu}{E}\delta_{ij}S \quad (15)$$

$$\sigma_{ij} = \lambda\delta_{ij}e + 2G\varepsilon_{ij} \quad (16)$$

δ_{ij}=Kroniker delta (unit tensor)

I=unity ; $I = \begin{vmatrix} 1 & 0 & 0 \\ 0 & 1 & 0 \\ 0 & 0 & 1 \end{vmatrix}$

$$\delta_{ij} = \begin{cases} 0 & \text{for } i \neq j \\ 1 & \text{otherwise} \end{cases}$$

Modulus of rigidity

$$G = \frac{E}{2(1+\nu)}$$

E=Young's modulus

ν=Passion's ratio

Lame's coefficients

$$\lambda = \frac{E\nu}{(1+\nu)(1-2\nu)} \quad (17)$$

$$\gamma_{ij} = \frac{1}{2}(u_{i,j} + u_{j,i}) \quad (18)$$

γ_{ij} =Strain tensor

$u_{i,j}$ = Displacements gradient for Cartesian coordinate

$$\gamma_{xx} = \epsilon_x = \frac{\partial u}{\partial x}, \gamma_{yy} = \epsilon_y = \frac{\partial v}{\partial y}, \gamma_{zz} = \epsilon_z = \frac{\partial \omega}{\partial z} \quad (19)$$

$$\gamma_{xy} = \frac{1}{2}\left(\frac{\partial u}{\partial y} + \frac{\partial v}{\partial x}\right) \quad (20)$$

γ_{yz}

$$= \frac{1}{2}\left(\frac{\partial v}{\partial z} + \frac{\partial \omega}{\partial y}\right) \quad (21)$$

$$\gamma_{zx} = \frac{1}{2}\left(\frac{\partial \omega}{\partial x} + \frac{\partial u}{\partial z}\right) \quad (22)$$

x,y,z=1,2,3

u,v,ω=1,2,3

Ω_{ij} = Rotational strain tensor

$$\Omega_{ij} = \frac{1}{2}(u_{i,j} - u_{j,i}) \quad (23)$$

$$\Omega_x = \frac{1}{2}\left(\frac{\partial u}{\partial y} - \frac{\partial v}{\partial z}\right) \quad (24)$$

$$\Omega_y = \frac{1}{2}\left(\frac{\partial u}{\partial z} - \frac{\partial \omega}{\partial x}\right) \quad (25)$$

$$\Omega_z = \frac{1}{2}\left(\frac{\partial v}{\partial x} - \frac{\partial u}{\partial y}\right) \quad (26)$$

6. Result and discussion

The stresses of a spherical dome have then been analyzed using shape function. The outputs are calculated and plotted against the added loading. Dynamic analysis of three-dimensional dome structural is a direct extension of static analysis. The elastic stiffness matrices are the same for both dynamic and static analysis. It is only necessary to lump the mass of the structure at the joints. The addition of inertia forces and energy dissipation forces will satisfy dynamic equilibrium. The dynamic solution for steady state harmonic loading, without damping, involves the same numerical effort as a static solution.

The performance of this new formulation has been tested through a variety of linear and nonlinear mechanical problems. In all of these tests, the new shape function showed better performance than the previous formulation. In particular, the improvement is significant in the three-dimensional dome structural test. Figure(2-4) shows the geometry, loading ,boundary conditions ,orientation and coordinates system for this problem.

The radius is R=20m, the thickness t=0.7m, Young's modulus E=8.3×10^5 and Poisson's ratio **v**= 0.4. Due to symmetry the three dimensional pre-tensioned spherical dome is meshed using a single element through the thickness and with three unit loads along directions Ox, Oy and Oz The element is the standard, multi-node, full integration solid element. The results are

reported in Table 1 in terms of the normalized displacement at the load point and then the output used to simulate the model in the Nastran Program.

Table (1). Shape Functions for a Nine-Node 20 Element .

Optional Nodes	Shape Function $\phi(x, y, z)$	Normalized Displacement		
		u	v	w
3	xy	1	1	-1
4	xy^3	-1	1	0
5	xy^2	0	-1	-1
6	y^4	1	0	1
7	xy^3	0	1	0
8	xyz	-1	0	-1
9	xz^2	0	0	0

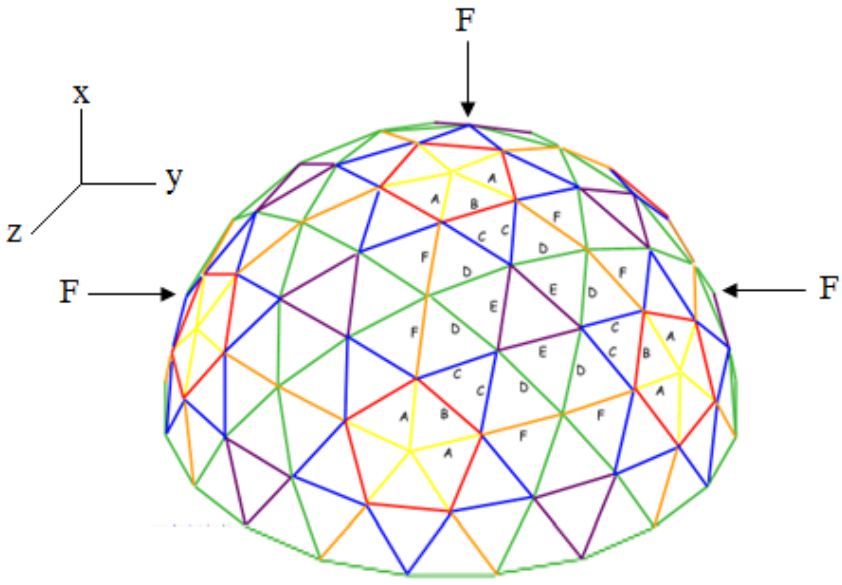

Figure(2). Dome .

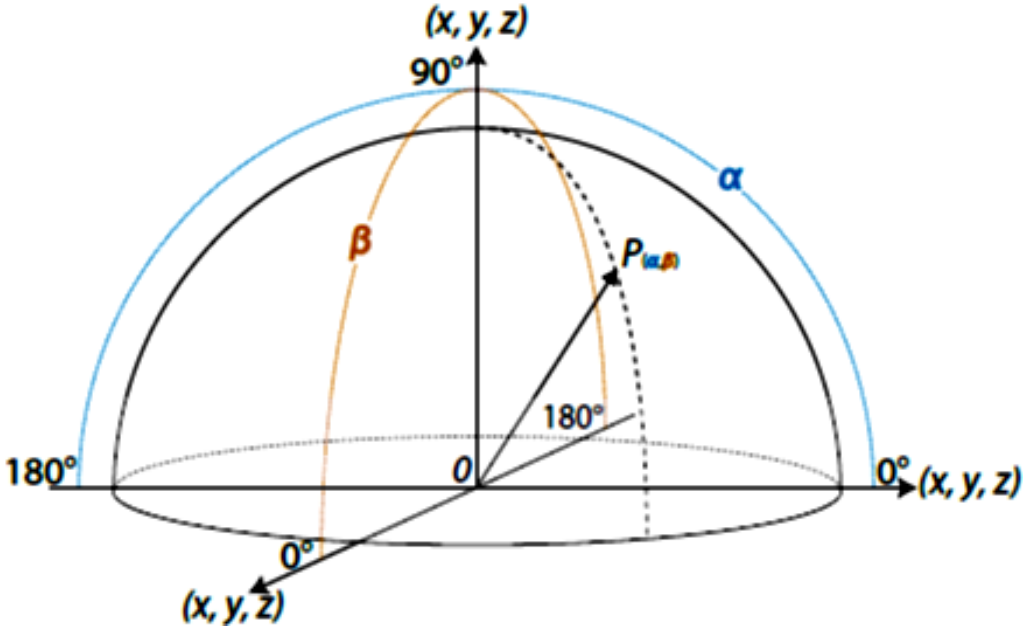

Figure(3). Spherical dome orientation.

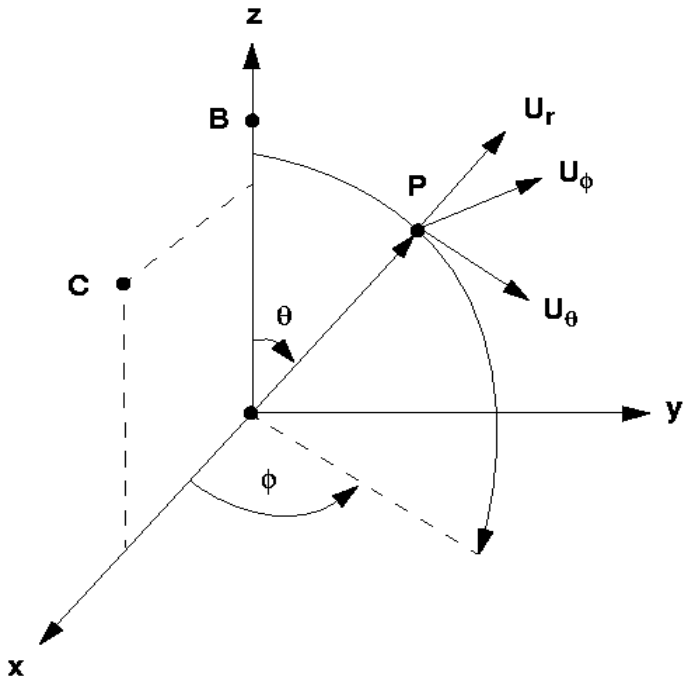

Figure (4). Spherical Coordinate Systems.

The solution of shape function is obtained with multi element; the nonlinear response to the initial radius is accurately recovered with (nxn) mesh of elements for a hemispherical dome. The model output used in the Nastran Program to build the dome structure, to simulate the dome stresses and deformation, and to draw stresses within total translation, within total rotation and maximum shear stresses, which is indicated in Figure (5-10)

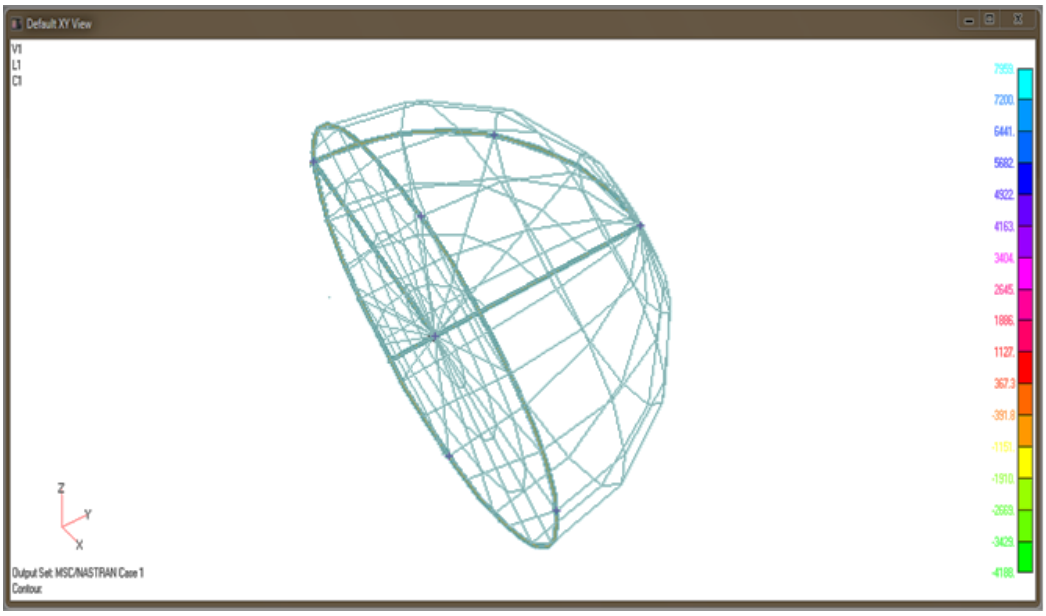

Figure(5). Output MSC NASTRAN Dome Building.

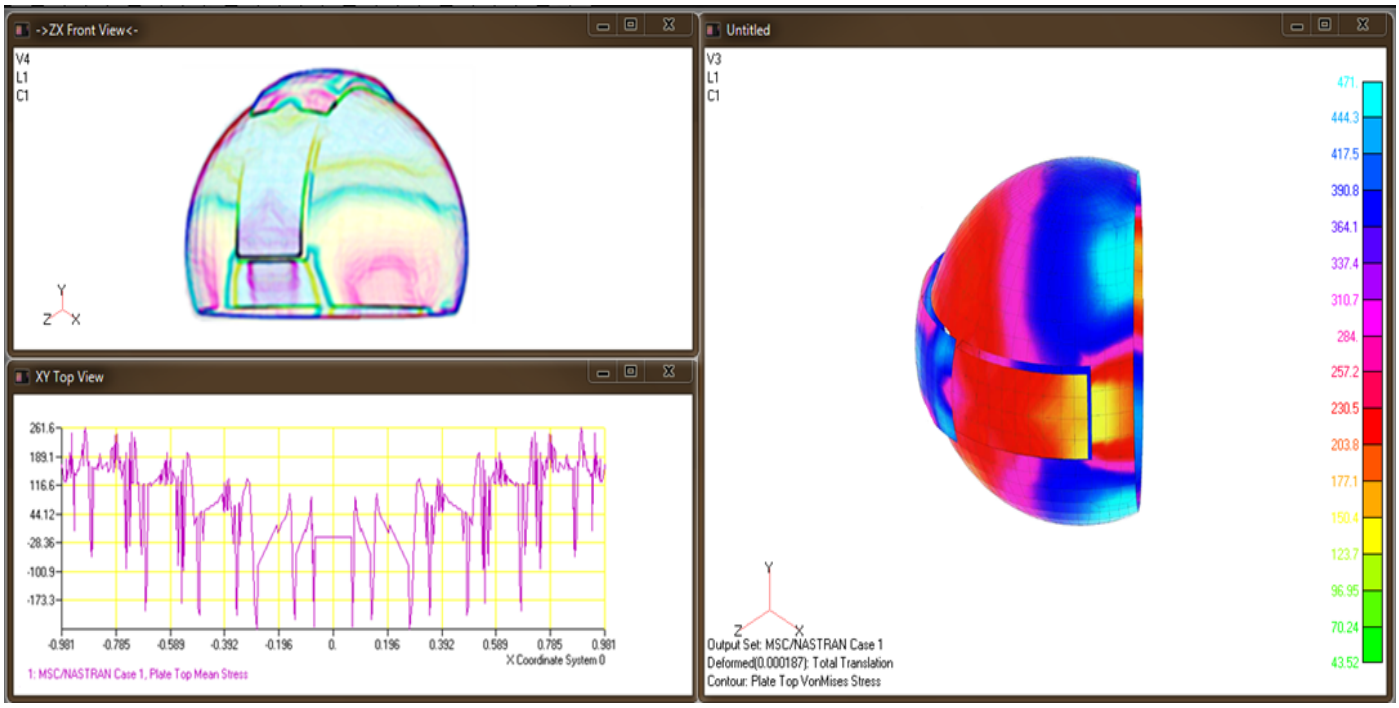

Figure(6). Output MSC NASTRAN Dome stresses and deformation.

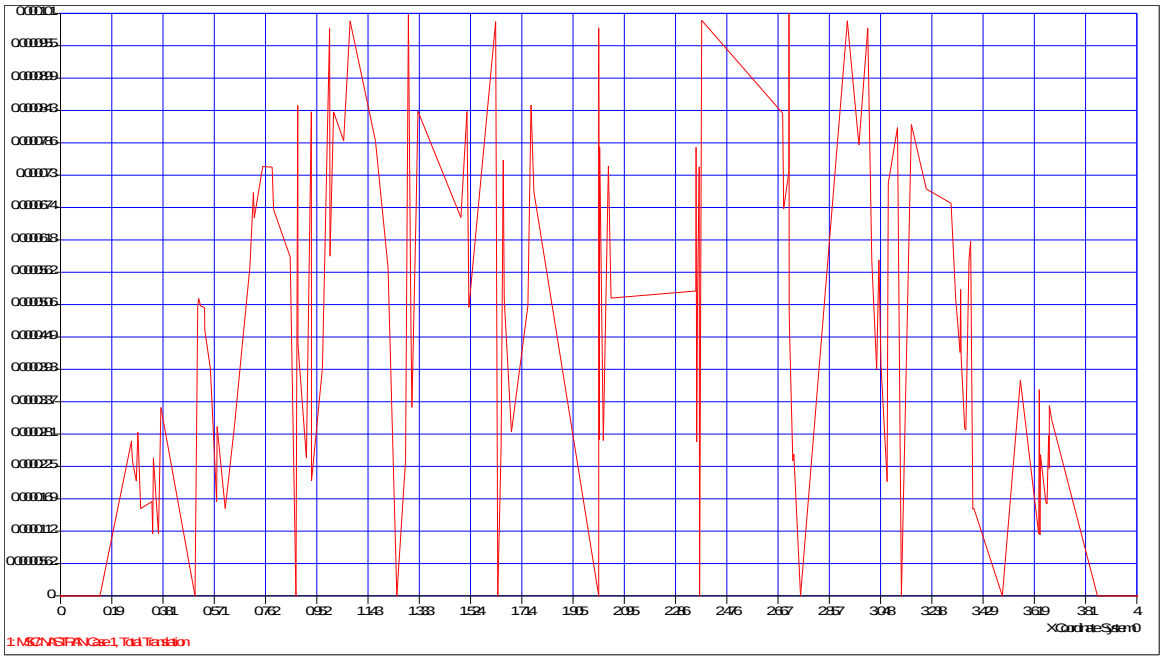

Figure(7). Stresses within total translation.

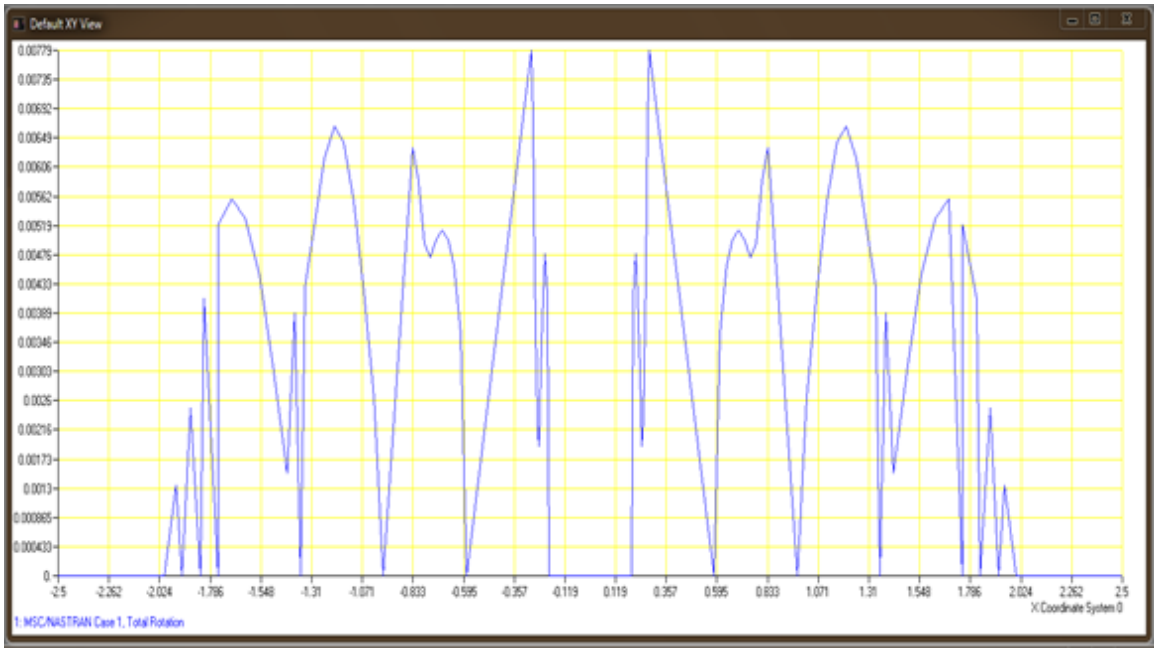

Figure(8). Stresses within total rotation.

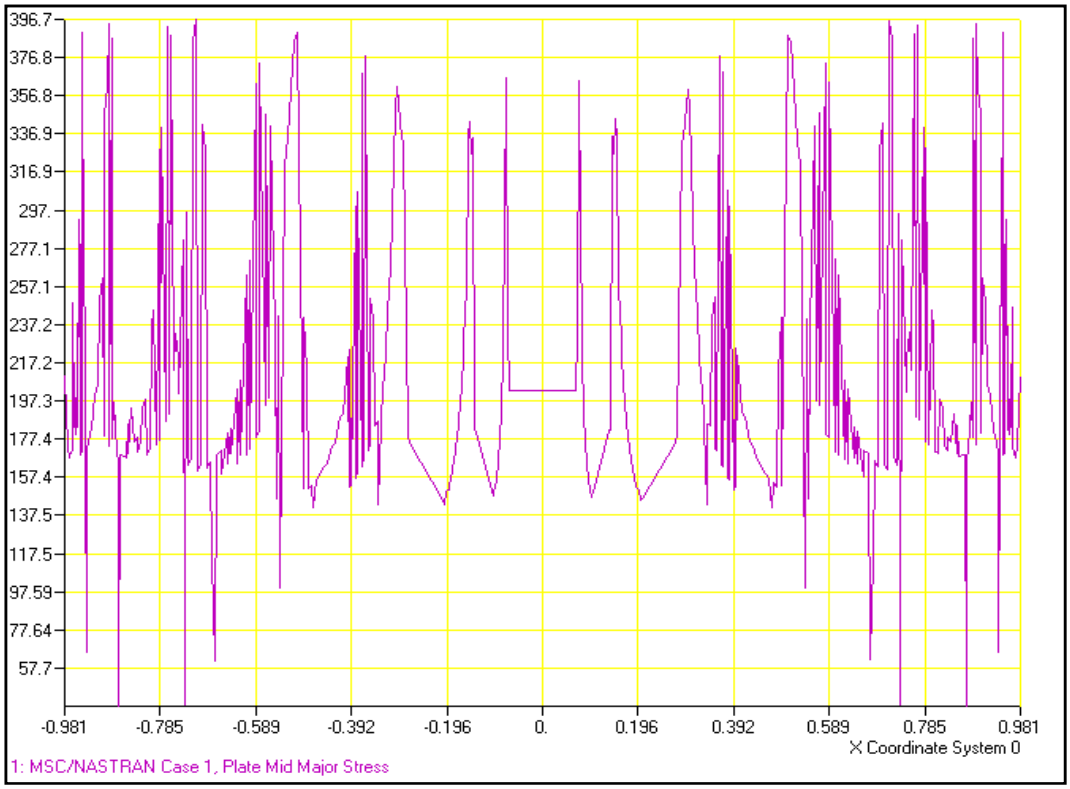

Figure(9). Stresses in the x-direction.

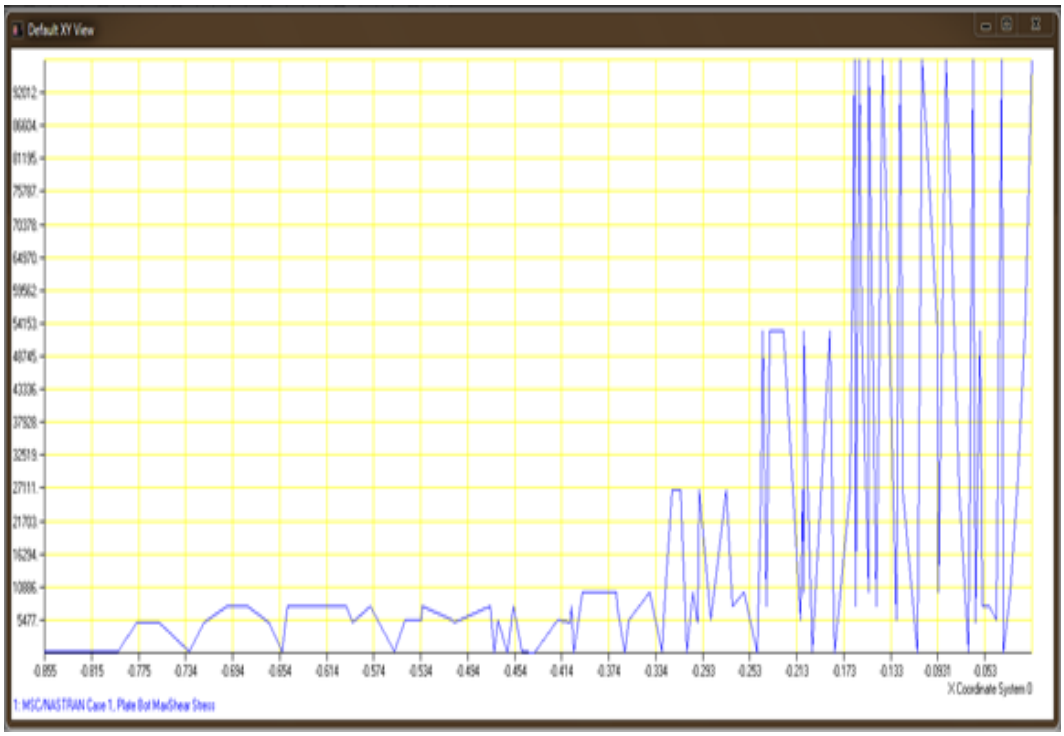

Figure(10). Max shear stresses.

7. Conclusion

This study demonstrated how to solve an elasticity problem using the proposed shape stress function. It showed how the method can be applied to find the stresses and displacements at any point on a 3-dimensional dome subjected to different boundary conditions. This led to how this stress function can be applied to any phase dome in finding the stresses and displacements at any point.

The aims of this paper is to enhance understanding of shape function of dome structures from theoretical point of view and to provide insights into the problems associated with computational modeling of their structural form and behaviour. The most commonly used computational approach is described, together With a brief evaluation of the method

1-Output stress resultants, shear forces and moments for dome structure elements is a required analysis output for any plate and shell type structure.

2- Displacements could be specified in a spherical coordinate system. This simplified the enforcement of boundary conditions on axisymmetric models.

3- Demonstrated how the stress function is applied to the spherical dome. On studying the graphical representation of the result, it can be seen that all stresses within dome surface are constant and the shear stress is zero when subjected to a hoop stress. The maximum stress occurs at the boundary of the dome intersecting the y-axis and is decreased along the boundary of the disc as it nears the x-axis. The maximum compressive stress occurs at the boundary intersecting with the x-axis and decreases as it nears the z-axis along the interfacing boundary.

4- The stresses in the spherical dome are three dimensional at the top of the spherical dome; the value of the circumferential strain is equal to that of the radial strain because the stretching is uniform in all directions at the apex. Furthermore, the circumferential strain is fixed at zero at the edge of the spherical dome, due to the clamping condition at the boundary.

8. References

[1] Roth, B., Whiteley, W., “Tensegrity Framework,” Transactions American Mathematics Society, Vol.265, pp. 419-446, 1981.
[2] Jayan B Bayat, “position analysis of planar tensegrity structures” , university of florida,2006
[3] Dharshini Rao Raaokavati,” Airy stress function for two dimensional inclusion problems”, University of Texas at Arlington, December 2005
[4] Edward L. Wilson,”Three-Dimensional Static and Dynamic Analysis of Structures”, Berkeley, California, USA, January 2002
[5] Chandrashekhra K. “Analysis of Thin Concrete Shells”, 2nd ed., new age international publishers, India, 1995.

[6] Jackson Mississippi "The Finding of Structural Evaluation of the 5 meter Diameter Dome", Report, San Jose, California 2002.
[7] L. Naff, T. F. Russell, and J. D. Wilson. "Test functions for three-dimensional control-volume mixed finite-element methods on irregular grids". In L. R. Bentley et al., editors, Proceedings of the XIII International Conference on Computational Methods in Water Resources, Calgary, Alberta, Canada, 25-29 June, 2000, pages 677–684. A. A. Balkema, 2000.
[8] Sadd, Martin H. (2005). "Elasticity: Theory, Applications and Numeric" , (pp. 123-259), Burlington, MA: Elsevier Academic Press.
[9] O. C. Zienkiewicz, R. L. Taylor, "Finite Element Method", Vol 1, the Basis, 2000.

9. Nomenclature

$\phi(x,y,z)$	Shape function, [dimensionless]
σ_x	Stress in x-direction, [N/m^2]
σ_y	Stress in y-direction, [N/m^2]
τ_{xy}	Shear stress in xy direction, [N/m^2]
T_{ij}	External forces, [N]
σ_{ij}	Stress tensor, [N/m^2]
ε_{ij}	Strain tensor, [N/m^2]
δ_{ij}	Kroniker delta (unit tensor), [dimensionless]
E	Young's modulus, [N/m^2]
ν	Passion's ratio, [dimensionless]
λ	Lame's coefficients, [dimensionless]
γ_{ij}	Shear Strain tensor, [dimensionless]
$u_{i,j}$	Displacements gradient for Cartesian coordinate, [mm]
Ω_{ij}	Rotational strain tensor, [dimensionless]
∇	Vector differential operator (Del or Nabla), [dimensionless]

Prediction of the Shear Strength of Concrete Beams Reinforced with Fiber Reinforced Polymer Bars Using Artificial Neural Networks Model

Mohammed A. Mashrei

Civil Engineering Department
College of Engineering
Thi_Qar University
moha74ed@yahoo.com.

Abstract

In this paper an Artificial Neural Networks (ANNs) model is developed to predict the shear strength of concrete beams reinforced with fiber reinforced polymer (FRP) bars. An experimented data set collected from the experimental studies on concrete beams reinforce with FRP bars are used in the artificial neural network. They are arranged in a format of six input parameters including the width and depth of beams, compressive strength of concrete, modulus of elasticity, reinforcement ratio of FRP and the shear span to depth ratio and one output parameter which is shear strength. A parametric study is carried out using ANN to study the influence of each parameter on the shear strength of concrete beams reinforced with fiber reinforced polymers; the results showed that the shear strength increases with increasing all parameters used in ANN model except the shear span to depth ratio. In this case, as the shear span to depth ratio decreases, the shear strength increase. The results of this study indicate that the ANN provides good prediction as compared to the experimental data and the empirical equations.

Keywords: concrete; beams; fiber reinforced polymers; Shear; Artificial Neural Networks.

حساب مقاومة القص للعتبات الخرسانية المسلحة بقضبان البوليمر باستخدام تقنيات الشبكات العصبية الصناعية

المستخلص

في هذا البحث تم استخدام تقنيات الشبكات العصبية الصناعية للتنبؤ بمقاومة العتبات الخرسانية والمسلحة تسليحا رئيسيا بقضبان البوليمر. تم الاستفادة من التجارب العملية لباحثين سابقين لاستخدامها في إنشاء الشبكة العصبية الصناعية حيث تم اخذ العوامل المؤثرة هندسيا على تصرف العتبات بشكل عام لبناء الشبكة. كانت العوامل المدخلة هي **العرض و السمك الفعل للنموذج، مقاومة الخرسانة**، معامل المرونة ونسبة التسليح لقضبان البوليمر بالإضافة إلى نسبة فضاء القص الى السمك الفعال للنموذج اما المخرجات فهي مقاومة القص للعتبات. كذلك تم في هذا البحث دراسة تأثير كل عنصر من العناصر المدخلة على مقاومة القص للعتبات المسلحة بقضبان البوليمر حيث بينت النتائج بان مقاومة

القص تزداد بزيادة كل من العرض و السمك الفعال للنموذج، مقاومة الخرسانة، معامل المرونة ونسبة التسليح لقضبان البوليمر وبنقصان نسبة فضاء القص الى السمك الفعال للنموذج .

أثبتت النتائج التي تم الحصول عليها من هذا البحث بان تقنية الشبكات العصبية طريقة موثوقة وجيدة لحساب مقاومة القص وذلك بعد مقارنتها مع بعض النتائج العملية والطرق المقترحة الأخرى.

1. Introduction

FRP bar is made from filaments or fibers held in a polymeric resin matrix binder. The FRP Bar can be made from various types of fibers such as Glass (GFRP) or Carbon (CFRP). FRP bars have a surface treatment that facilitates a bond between the finished bar and the structural element into which they are placed [1].

During the last two decades, fiber reinforced polymer (FRP) materials have been used in a variety of configurations as an alternative reinforcement for new and strengthening civil engineering structures. The attractiveness of the material lies mainly in their high corrosion resistance, high strength and fatigue resistance. In some cases, the non-magnetic characteristics became more important for some special structures. An important application of FRP, which is becoming more popular [2], is the use of FRP as reinforcement in concrete structures. The use of the FRP in concrete structures includes: (a) the internal reinforcing (rod or bar) which will be used instead of the steel wire (rod) equivalent; and (b) the external bonded reinforcement, which is typically used to repair/strengthen the structure by plating or wrapping FRP tape, sheet or fabric around the member.

There are fundamental differences between the steel and FRP reinforcements: the latter has a lower modulus of elasticity, The modulus of elasticity for commercially available glass and aramid FRP bars is 20 to 25 % that of steel compared to 60 to 75 % for carbon FRP bars [1] and linear stress–strain diagram up to rupture with no discernible yield point and different bond strength according to the type of FRP product. These characteristics affect the shear capacity of FRP reinforced concrete members. Due to the relatively low modulus of elasticity of FRP bars, concrete members reinforced longitudinally with FRP bars experience reduced shear strength compared to the shear strength of those reinforced with the same amounts of steel reinforcement. This fact is supported by the findings from the experimental investigations on concrete beams without stirrups and reinforced longitudinally with carbon and glass FRP bars [3, 4].

El-Sayed et al. [4], carried out an experimental study to investigate the shear strength of concrete beams without shear reinforcement (stirrups) and reinforced in the longitudinal direction with different types and ratios of FRP bars. They found that the ratio of shear

strength of concrete beams reinforced with FRP bars to that of beams reinforced with steel is proportional to the cube root of the axial stiffness ratio between FRP and steel reinforcing bars. El-Sayed et al. [5], They proposed equation to calculate the shear strength of concrete beams reinforced with FRP bars. They verified the proposed equation with many test results.

F.M. Wegian, H.A. Abdalla [6], presented an experimental investigation on the behavior of concrete beams reinforced with different FRP bars. Three beams were reinforced by GFRP, Isorod, two beams were reinforced by GFRP, C-bar, and two beams were reinforced by CFRP, Leadline. The ultimate behavior of the seven simply supported FRP reinforced concrete beams was used to evaluate their flexural and shear capacities. They concluded that the concrete beams reinforced with fiber reinforced polymers, behave linearly up to cracking, and linearly after cracking with reduced stiffness. Strains and deflections are generally higher in concrete beams reinforced with FRP bars than in concrete beams reinforced with steel. Omeman et al. [7], investigated the shear strength, deflection, and mode of failure of concrete short beams reinforced with CFRP bars and compared with that of similar beams reinforced with steel bars. The experimental study showed that using CFRP bars as tensile reinforcement in RC short beams had a significant effect on the shear strength and deflection of tested beams.

Soft computing is a new field appears in recent past to solve some problems such as decision-making, modeling and control problems. Soft computing is an emerging approach to computing with parallels the remarkable ability of the human mind to reason and learn in an environment of uncertainty and imprecision [8]. Soft computing consists of many complementary tools such as artificial neural networks.

Artificial neural networks have been used extensively in the area of civil engineering to solve many problems. Rafiq et al. [9] presented practical guidelines for designing Artificial Neural Networks for engineering applications. Hsu and Chung [10] developed a model of damage diagnosing for reinforced concrete structures with artificial neural network technique. Learning procedure for the network showed that the capability of the convergence is acceptable, and the test results showed the proposed technique to be efficient for the structural damage diagnosing purpose. Cladera A. [11] developed an artificial neural network to predict the shear strength of reinforced concrete members without stirrups reinforcement based on database available from experimental tests. Based on the artificial neural network results, a parametric analysis was carried out to study the influence of each parameter affecting the failure shear strength. Inel [12] developed an ANN model to estimate the strength of RC columns whose behavior is dominated by flexural failure. Experimental data of 237 rectangular columns from an existing database were

used. Abdallaa et al. [13] presented application of ANN for predicting the shear resistance of rectangular R/C beams. Six parameters that influence the shear resistance of beams are used as input for the ANN. It is concluded that ANN can predict the shear resistance of rectangular R/C beams, to a great degree of accuracy.

Most of the problems solved in civil and structural engineering using ANN predicts the behavior of structural elements such as beams and columns based on given experimental results that are used as a training, testing and verification data. Artificial neural networks (ANN) are the most commonly used in structural engineering applications where a set of input parameters are mapped through single or several hidden layers, using weights, into output parameters.

In this study an Artificial Neural Network (ANN) model is developed to predict the shear strength of concrete beams reinforced with FRP bars. The results obtained by ANN model are compared with experimental values and with those determined by other models to assess the efficiency of these models. The developed ANN model is also utilized to evaluate the influence of various variables which govern the behavior of such members. The study based on the available databases with 76 tested members. The data set is randomly split into two groups: the first group of 64 is used for training the neural network model, and the remaining 12 data (about 16% of the data) are used for testing the model.

2. Review of the design equations

Most of the shear design provisions incorporated in codes and guides are based on the design formulas of members reinforced with conventional steel considering some modifications to account for the substantial differences between FRP and steel reinforcement. These provisions use the well-known $V_c + V_s$ method of shear design, which is based on the truss analogy. This section reviews the concrete shear strength of members longitudinally reinforced with FRP bars (V_{cf}) [5, 14, 15].

a-American concrete institute (ACI 440.1R-03)

The equation for shear strength proposed by the American Concrete Institute (ACI 440.1R-03) [14], can be expressed as follows:

$$V_{cf} = \frac{\rho_f E_f}{90\beta_1 f_c'}\left(\frac{\sqrt{f_c'}}{6} b_w d\right) \leq \frac{\sqrt{f_c'}}{6} b_w d \qquad 1$$

b-Tureyen and Frosch equation [15]

This equation developed by Tureyen and Frosch [15]. It was developed from a model that calculates the concrete contribution to shear strength of reinforced concrete beams. The equation was simplified to provide a design formula applicable FRP reinforced beams as follows:

$$V_{cf} = \frac{2}{5}\left(\frac{\sqrt{f_c'}}{6}\, b_w\, c\right) \qquad 2$$

where $c = kd$= cracked transformed section neutral axis depth (mm).

$$k = \sqrt{2\rho_f n_f + (\rho_f n_f)^2} - \rho_f n_f$$

c- El-Sayed et al. equation [5]

They were applying the same procedure in ACI 440.1R-03 to derive Eq. 1 above, with some modification for proposing the Eq. below :

$$V_{cf} = 0.037\,(\frac{\rho_f E_f \sqrt{f_c'}}{\beta_1})^{1/3}\, b_w\, d \;\le\; \frac{\sqrt{f_c'}}{6}\, b_w\, d \qquad 3$$

According to ACI 440.1R-03, the factor β_1 in the denominator of Eq. 3 is a function of the concrete compressive strength. It can be simply expressed by the following equation:

$$0.85 \ge \beta_1 = 0.85 - 0.007(f_c' - 28) \ge 0.65$$

3. Shear database

From the review of literatures [4, 6, 7, 15-26], a number (76) of shear strength test are used for developing the ANN. The all specimens were simply supported and were tested in three-point loading. The main reinforcement of all specimens is FRP (carbon FRP bars, and glass FRP bars) and there is no transverse reinforcement. All specimens were failed in shear, in other words, the failure of specimens is due to the propagated the cracks from the support toward the point of load application in an inclined direction. The collection data are divided into two sets: a training set containing 64 members, and testing set comprised of 12 members.

Six input variables are selected to build the ANN model. These variables are width (b_w), and depth (d) of the beams, modulus of elasticity of FRP (E_f), compressive strength of concrete (f_c'), reinforcement ratio of FRP (ρ_f) and the shear span to depth ratio (a/d). The

output value is the shear strength of FRP beams. Table 1 summarizes the ranges of the different variables.

Table (1). Range of parameters in the database.

Parameters	Range
Width of beams (b_w) mm	89-1000
Effective depth of beams (d) mm	143-360
Shear span to depth ratio ($^{a}/_{d}$)	1.3-6.5
Compressive strength of concrete (f_c') MPa	24-81
modulus of elasticity of FRP (E_f) (GPa)	37-145
Reinforcement ratio of FRP (ρ_f)	0.25-2.63

4. Artificial Neural Network Model

Neural networks can be thought of as "computational system" that accept inputs and produces outputs [27]. Figure(1) shows a typical neural network structure consisting of three layers [27]:

●Input Layer: A layer of neurons that receives information from external sources, and passes this information to the network for processing. These may be either sensory inputs or signals from other systems outside the one being modeled.

●Hidden Layer: A layer of neurons that receives information from the input layer and processes them in a hidden way. It has no direct connections to the outside world (inputs or outputs information). All connections from the hidden layer are to other layers within the system.

●Output Layer: A layer of neurons that receives processed information and sends output signals out of the system.

Additionally bias, acts on a neuron like an offset. The function of the bias is to provide a threshold for the activation of neurons. The bias input is connected to each of the hidden and output neurons in a network**.**

The number of input neurons corresponds to the number of input variables into the neural network, and the number of output neurons is the same as the number of desired output variables. The number of neurons in the hidden layer(s) depends on the application of the network.

As inputs enter the input layer from an external source, the input layer becomes “activated” and emits signals to its neighbors (hidden layer) without any modification. Neurons in the input layer act as distribution nodes and transfer input signals to neurons in the hidden layer. The neighbors receive excitation from the input layer, and in turn emit an output to their neighbors (second hidden layer or output layer). Each input connection is associated with a quantity, called “a weight factor” or “a connection strength” [27].

The strength of a connection between two neurons determines the relative effect that one neuron can have on another. The weight is positive if the associated connection is excitatory and negative if the connection is inhibitory [27].

5. Shear strength of concrete beams with (FRP) bars using ANN

ANN is used to investigate the shear strength of concrete beams reinforced with FRP bars. The configuration and training of neural networks is a trail-and-error process due to such undetermined parameters as the number of nodes in the hidden layer, and the number of training patterns.

In the developed ANN, there is an input layer, where input data are presented to network and an output layer, with one neuron representing shear strength of concrete beams reinforced with FRP bars. One hidden layer as an intermediate layer is also included. The network with one hidden layer and four nodes in the hidden layer gave the optimal configuration with minimum mean square error (MSE).

Six input variables are: width (b_w), and depth (d) of the beams, modulus of elasticity of FRP (E_f), compressive strength of concrete (f_c'), reinforcement ratio of FRP (ρ_f) and the shear span to depth ratio (a/d).

The back-propagation neural network model used for this study is trained by feeding a set of mapping data with input and target variables. The main objective of training the neural network is to assign the connection weights by reducing the errors between the predicted and actual target values to a satisfactory level. This process is carried out through the minimization of the defined error function by updating the connection weights. Also, the number of hidden layers, number of hidden nodes, transfer functions, and normalization of data are chosen to get the best performance of the model. After the errors are minimized, the model with all the parameters including the connection weights is tested with a separate set of “testing” data that is not used in the training phase. At the end of the training, the neural network represents a model that should be able to predict the target value.

The network has trained continually through updating of the weights until error goal of $15.1*10^{-4}$ is achieved. Figure (2) shows the performance for training and generalization (testing). A resilient back propagation training algorithm is used to train the network, for 800 epochs to check if the performance (MSE) for either training or testing sets might diverge.

The network performance with resilient back propagation training algorithm have been tested for training and testing patterns, as shown in Figures (3 and 4). A good agreement has been noted in the predicting values compared with the actual (targets) values.

6. Parametric analyses based on ANN

Once the artificial neural network has been trained, a parametric analysis is used to study the influence of the various parameters on the shear strength of beams. The basic idea is to predict the effect of varying the value of only one variable while the remaining variables are kept constant with the same updated weights and bias matrices after being trained.

Figure(5) shows the effect of width of specimen on shear strength of concrete beams reinforced with FRP. It can be seen from this figure that the shear strength variation is non-linearly with width of specimen and as the width increases, the shear strength increase and this in agreement with the results obtained by Eqs. (1), (2) and (3).

In Figure6 the shear strength of concrete beams reinforced with FRP is plotted versus the depth of member (d mm). It can be clearly seen from the figure that the increase in depth of beams leads the shear strength to increase. which is in agreement with the experimental results of Omeman et al. [7] and the ACI 440.1R-03, Tureyen and Frosch and proposed by El-Sayed et al equations [4,14,15] respectively. The result in this study supports and proves that the beam's effective depth has a significant effect on the shear strength, so the shear strength is a function of the beam effective depth in addition to other parameters.

The results of five concrete beams reinforced with FRP with a compressive strength of concrete varying from 25 to 80 MPa showed that the shear strength increased as compressive strength of concrete (f_c') increased as shown in Figure (7). The conclusion of increasing shear strength with increasing f_c' is in agreement with the Canadian standard (CSA 2002) [28] and the American Concrete Institute (ACI) [14]. According to ACI the shear strength of beams reinforced with FRP can be estimated by using Eq. (1). Eqs. (2) and (3) also strongly supported this observation. Also El-Sayed et. al. [17] in experimental study, showed that the shear strength of concrete beams reinforced with FRP increased with increasing f_c'.

Figure (8) shows the influence of modulus of elasticity (E_f) of FRP on shear strength. As smaller to previous parameter when the E_f increases, the shear strength increase. El-Sayed

[18] concluded that the shear strength of concrete beams reinforced with FRP increased with increasing the modulus of elasticity of FRP with same amount of FRP. Also Esq. (1), (2) and (3) supported this conclusion.

The shear span to depth ratio has a very important influence on the shear strength of concrete beams reinforced with FRP. Figure (9) shows that the relationship between shear span to depth ratio ($^{a}/_{d}$) and shear strength is non-linear and also can be seen that the shear strength significantly increased with decreasing $^{a}/_{d}$. Figure (9) shows that the decreasing $^{a}/_{d}$ by 35% in other words, from 2 to 1.3 increased the shear strength by 184%. El sayed [18] found that the shear strength of concrete beams reinforced with carbon fire reinforced polymer increase with decreasing shear span to depth ratio. He found that when the decreasing $^{a}/_{d}$ by 23.1% (from 1.69 to 1.3), increased the shear strength by 90.8%. Also Figure(9) shows that the increasing in shear strength is insignificantly after $^{a}/_{d} > 2.5$ this may be attributed to the fact that the beam behaved as a deep beams when $^{a}/_{d} < 2.5$, in this case the arch action will be occurred. For such beams, a significant of redistribution of internal forces expected after cracking and a large part of shear force is transferred to support, however, the arch action enhance the shear strength of member [4, 18, 29].

In the present study, also a sensitivity notation has been conducted using ANN model to investigate the effect of longitudinal reinforcement ratio (ρ_f) on the shear strength of FRP reinforced concrete beams without stirrups. Figure (10) presents the effect of ρ_f on the shear strength of reinforced concrete beams. It is shown that the shear strength increases with increase the ratio of FRP (ρ_f). However, a linear relationship is seems in Figure(10). In general this prediction is agree with the experimental study conducted by different authors [7, 18, 26].

It is observed from these figures that the shear span to depth ratio ($^{a}/_{d}$) is the most important factor among the input variables.

7. Comparison between experimental and theoretical results

The predictions of shear strength of beams reinforced with FRP as that obtained from ANN, ACI 440.1R-03, Tureyen and Frosch equation, and proposed equation by El-Sayed et al., are compared with the experimental results and shown for both training and testing sets in Figures(11 and 12) and Table (2).

In Table (2) the ratios of experimental (V_e) to theoretical (V_i) predictions of the shear strength of beams reinforced with FRP along with their average and standard deviation are presented. The theoretical predications include those obtained by ANN (V_1), proposed equation by El-Sayed et al. (V_2), ACI 440.1R-03 (V_3), and Tureyen and Frosch equation (V_4). It can be seen that ANN model gives average values for testing set of V_e/V_1 of 0.97 and standard deviations of 0.1 which is much better than the values obtained from other methods. Figures (11 and 12) confirm the same conclusion that the predictions of ANN model are better than those of the other methods.

Also in Table (3) the correlation coefficient R of predicted shear strength that evaluated by ANN and the other methods are summarized. As shown in Table (3), the ANN produces a higher correlation coefficient R as compared with the other methods. Therefore the ANN can serve as reliable and simple tool for the prediction of shear strength of beams reinforced with FRP.

8. Conclusion

This research can be considered as contribution to an ongoing effort to develop artificial neural network system for solving the civil engineering problems. In this study the model based on Artificial Neural Network (ANN) are developed to predict the shear strength of beams reinforced with FRP. A database of a seventy six (76) tests data developed from the review of literature for the training and testing of model. Six variables are selected as input to ANN model with one target variable, shear strength of beams reinforced with FRP.

With the developed ANN, predictions of shear strength are made using back-propagation neural network as well as available methods, and they are also compared with experimental results. We found that the ANN prediction agree much better with the experimental values as compared to those from the other methods. The results of this study indicate that ANN provides a reliable and simple tool for the prediction of shear strength of beams reinforced with FRP. Also through the parametric study based on ANN, the network is able to learn about the effect of each input variables on the final outputs.

Table (2). Comparison Between Experimental and Analytical Results Obtained by Different Methods for Training and Testing Sets for Shear Strength reinforced with FRP.

No.	Shear Strength V_u (kN)					Ratio			
	Exp. V_e	ANN V_1	El-Sayed Eq. V_2	ACI 440 V_3	Tureyen and et al. Eq. V_4	$\frac{V_e}{V_1}$	$\frac{V_e}{V_2}$	$\frac{V_e}{V_3}$	$\frac{V_e}{V_4}$
	Training Set								
1	140	149.49	99.66	28.09	66.34	0.94	1.40	4.98	2.11
2	167	160.68	125.56	56.18	90.54	1.04	1.33	2.97	1.84
3	190	178.38	139.95	82.53	105.15	1.07	1.36	2.30	1.81
4	113	114.69	89.72	21.32	57.82	0.99	1.26	5.30	1.95
5	163	142.79	112.82	42.38	79.04	1.14	1.44	3.85	2.06
6	163	170.25	124.58	59.32	90.71	0.96	1.31	2.75	1.80
7	168	182.25	123.8	61.97	90.83	0.92	1.36	2.71	1.85
8	77.5	80.61	69.26	34.15	52.45	0.96	1.12	2.27	1.48
9	70.5	60.5	46.6	10.41	30.67	1.17	1.51	6.77	2.30
10	104	93.38	77.65	51.17	60.25	1.11	1.34	2.03	1.73
11	124.5	116.95	86.27	71.11	68.5	1.06	1.44	1.75	1.82
12	77.5	74.87	58.49	22.16	41.6	1.04	1.33	3.50	1.86
13	130	136.36	91.77	67.53	76.42	0.95	1.42	1.93	1.70
14	87	91.15	62.19	21.01	46.04	0.95	1.40	4.14	1.89
15	115.5	107.41	67.63	27.03	51.54	1.08	1.71	4.27	2.24
16	36.1	42.77	25.4	6.23	16.5	0.84	1.42	5.79	2.19
17	47	50.23	33.03	12.28	23.82	0.94	1.42	3.83	1.97
18	42.7	50.12	38.63	21.91	28.93	0.85	1.11	1.95	1.48
19	49.7	33.57	32	12.45	22.6	1.48	1.55	3.99	2.20
20	38.5	29.71	32	12.45	22.6	1.30	1.20	3.09	1.70
21	14	28.54	11.85	3.06	8.26	0.49	1.18	4.58	1.69
22	20	20.06	17.72	6.55	13.27	1.00	1.13	3.05	1.51
23	15.4	10.37	15.45	5.69	12.3	1.49	1.00	2.71	1.25
24	59.1	60.86	29.01	6.47	18.26	0.97	2.04	9.13	3.24
25	44.1	56.72	34.24	9.69	23.09	0.78	1.29	4.55	1.91
26	46.8	47.67	34.59	13.21	23.66	0.98	1.35	3.54	1.98
27	47.5	48	29.97	13.45	21.37	0.99	1.58	3.53	2.22
28	57.1	57.26	38.04	29.26	28.78	1.00	1.50	1.95	1.98
29	38	37.49	32.2	7.35	23.38	1.01	1.18	5.17	1.63
30	35.77	41.46	30.97	9.99	23.97	0.86	1.15	3.58	1.49
31	46.4	49.54	40.7	14.98	32.23	0.94	1.14	3.10	1.44
32	108.1	102.63	94.73	24.48	61.97	1.05	1.14	4.42	1.74
33	94.7	101.43	92.49	22.71	59.96	0.93	1.02	4.17	1.58
34	137	154.78	120.62	48.57	86.26	0.89	1.14	2.82	1.59
35	152.6	152.53	117.76	45.07	83.57	1.00	1.30	3.39	1.83
36	177	160.31	127	56.45	92.4	1.10	1.39	3.14	1.92
37	38.13	28.53	30.63	8.95	20.2	1.34	1.24	4.26	1.89

Table(2). Continued.

38	44.43	33.4	35.02	13.38	24.22	1.33	1.27	3.32	1.83
39	45.27	37.56	43.92	17.77	30.66	1.21	1.03	2.55	1.48
40	45.1	38.02	41.49	18.24	29.36	1.19	1.09	2.47	1.54
41	42.2	39.56	38.7	18.21	27.68	1.07	1.09	2.32	1.52
42	53.4	65	35.06	20.28	23.92	0.82	1.52	2.63	2.23
43	36.1	42.58	25.04	6.98	15.11	0.85	1.44	5.17	2.39
44	40.1	50.04	30.12	12.15	19.42	0.80	1.33	3.30	2.06
45	26.8	30.64	23.8	5.74	14.52	0.87	1.13	4.67	1.85
46	28.3	28.29	24.01	5.67	14.72	1.00	1.18	4.99	1.92
47	28.5	33.45	23.75	5.76	14.46	0.85	1.20	4.95	1.97
48	27.6	26.74	24.1	5.64	14.81	1.03	1.15	4.89	1.86
49	185.2	191.16	19.93	13.34	14.87	0.97	9.29	13.88	12.45
50	154.9	138.61	20.31	13.07	15.37	1.12	7.63	11.85	10.08
51	91.5	101.61	20.46	13	15.57	0.90	4.47	7.04	5.88
52	185.5	184.17	25.67	26.08	20.48	1.01	7.23	7.11	9.06
53	298.1	300.76	36.34	25.8	28.16	0.99	8.20	11.55	10.59
54	468.2	466.03	48.22	32.84	36.55	1.00	9.71	14.26	12.81
55	226.9	226.76	22.02	12.22	17.67	1.00	10.30	18.57	12.84
56	179.5	194.63	65.33	32.56	47.91	0.92	2.75	5.51	3.75
57	164.5	153.92	43.66	9.72	27.79	1.07	3.77	16.92	5.92
58	175	167.49	50.96	15.45	34.38	1.04	3.43	11.33	5.09
59	233.5	251.09	84.87	71.38	66.61	0.93	2.75	3.27	3.51
60	196	184.3	56.72	21.31	39.74	1.06	3.46	9.20	4.93
61	372	351.68	76.25	51.76	58.37	1.06	4.88	7.19	6.37
62	269	285.74	50.96	15.45	34.38	0.94	5.28	17.41	7.82
63	42.6	48.51	69.42	16.25	47.46	0.88	0.61	2.62	0.90
64	86.1	83.92	93.61	19.05	62.25	1.03	0.92	4.52	1.38
AVERAGE						1.01	2.30	5.32	3.17
STDEV						0.158	2.31	3.94	2.98
	Testing Set								
65	142	149.23	110.44	41.3	77.3	0.95	1.29	3.44	1.84
66	60	64.1	52.46	15.78	35.95	0.94	1.14	3.80	1.67
67	174	169.09	99.82	86.88	84.69	1.03	1.74	2.00	2.05
68	47.2	47.07	34.56	15.69	25.03	1.00	1.37	3.01	1.89
69	9.8	9.42	9.82	2.63	7.39	1.04	1.00	3.73	1.33
70	50.15	44.46	35.37	20.16	26.78	1.13	1.42	2.49	1.87
71	32.53	36.93	26.5	7.31	19.94	0.88	1.23	4.45	1.63
72	114.8	105.88	99.87	28.41	66.67	1.08	1.15	4.04	1.72
73	31.73	31.67	25.84	8.9	17.55	1.00	1.23	3.57	1.81
74	29.2	37.52	23.58	5.88	14.29	0.78	1.24	4.97	2.04
75	162.3	170.3	23.12	19.79	17.98	0.95	7.02	8.20	9.03
76	195	219.37	76.25	51.76	58.37	0.89	2.56	3.77	3.34
AVERAGE						0.97	2.01	3.93	2.73
STDEV						0.10	1.72	1.62	2.27

Table (3). Comparison summary of correlation R.

Type	Correlation R	
	Training	Testing
ANN	0.995	0.993
El-Sayed Eq.	0.62	0.63
ACI 440	0.51	0.78
Tureyen and et al. Eq.	0.4	0.69

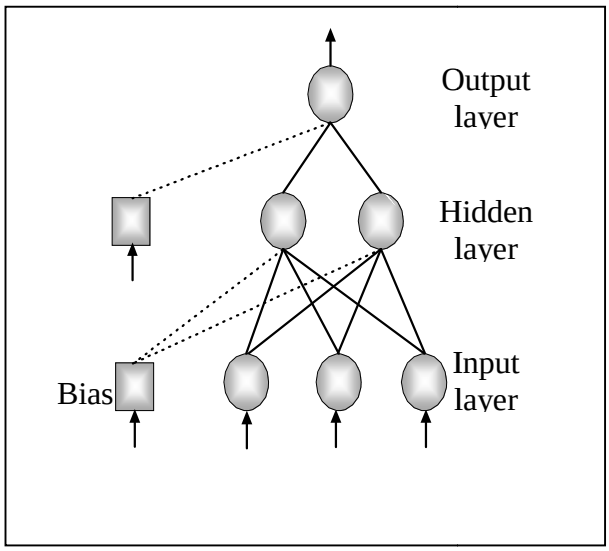

Figure (1). Structure of a typical multilayer neural.

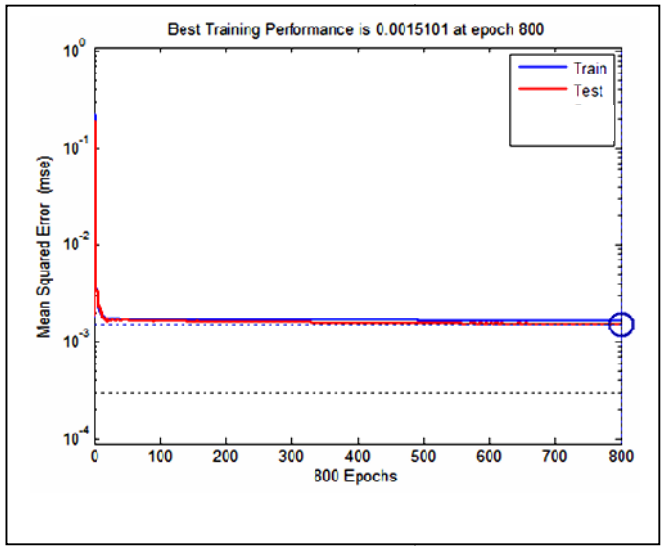

Figure (2). Convergence of the ANN for training and testing sets.

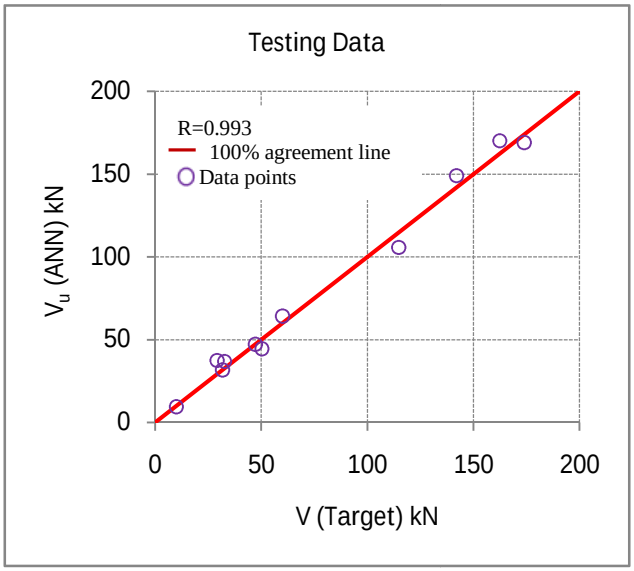

Figure(3). Comparison between ANN results and target results for training patterns sets.

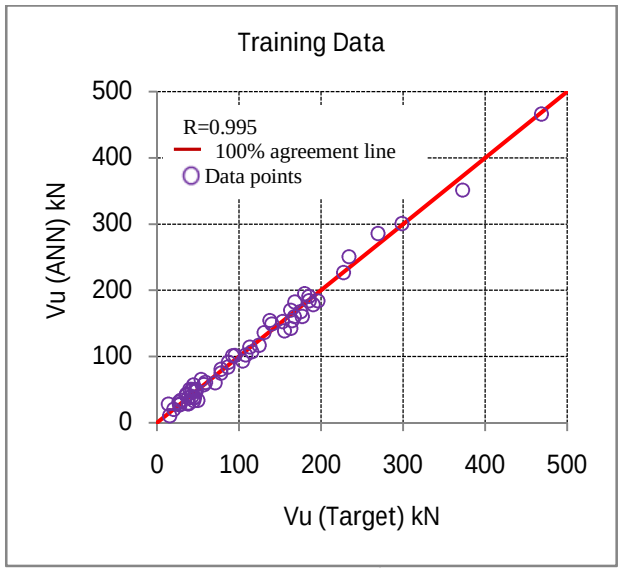

Figure(4). Comparison between ANN results and target results for testing patterns sets.

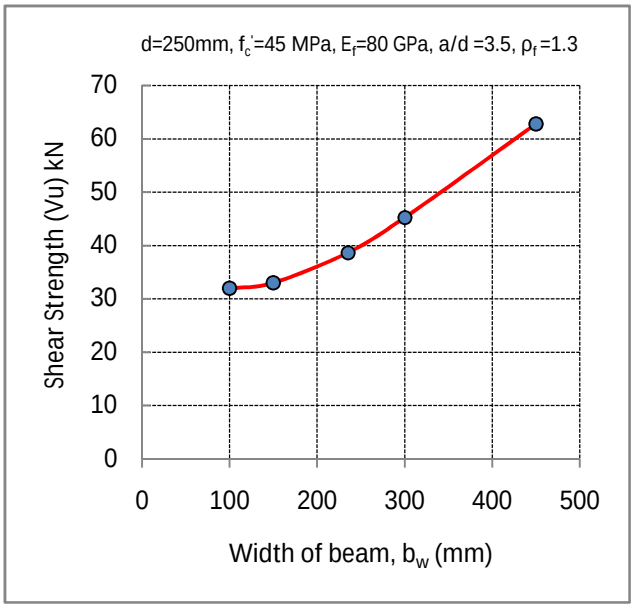

Figure(5). Effect the width of beams on shear strength of FRP beams.

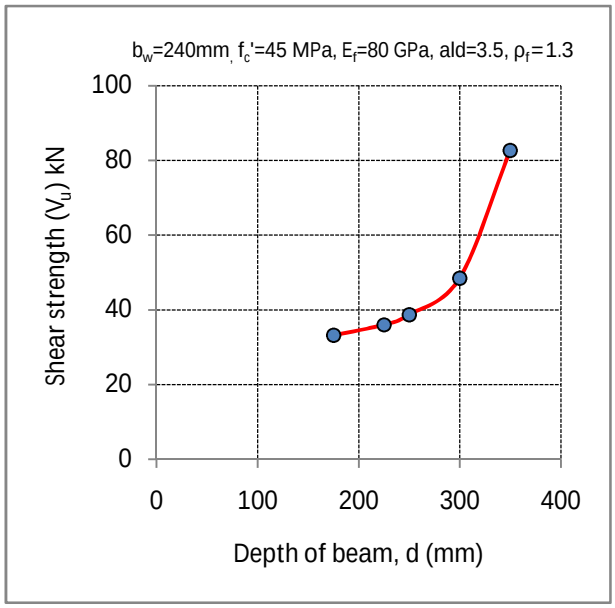

Figure(6). Effect the depth of beams on shear strength of FRP beams.

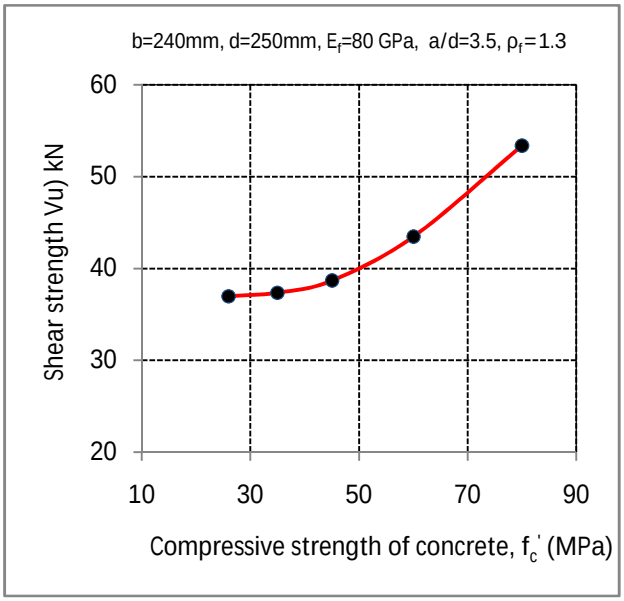

Figure(7). Effect of the compressive strength of concrete on shear strength of FRP beams .

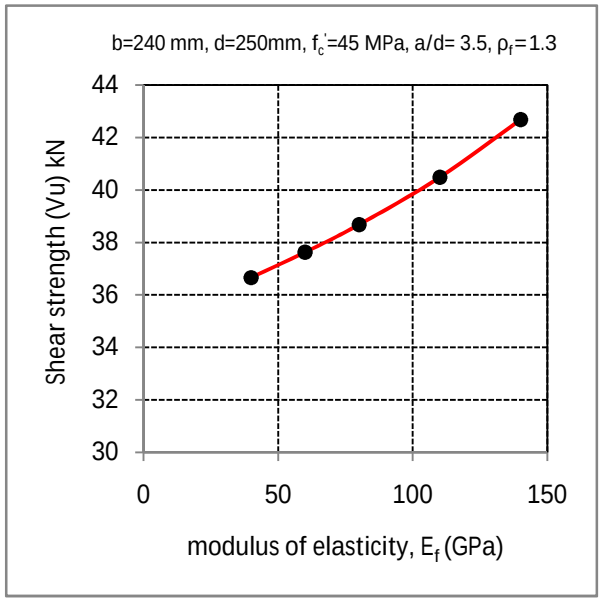

Figure(8). Effect of the modulus of elasticity (E_f) on shear strength of FRP beams .

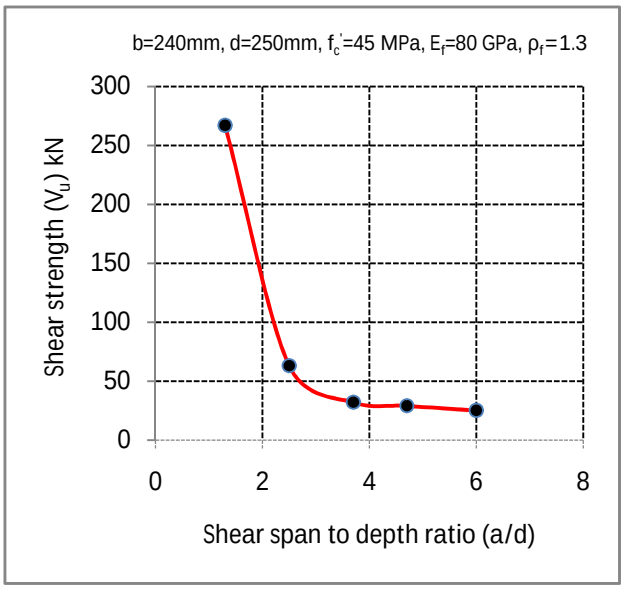

Figure(9). Effect the shear span to depth ratio on shear strength of FRP beams.

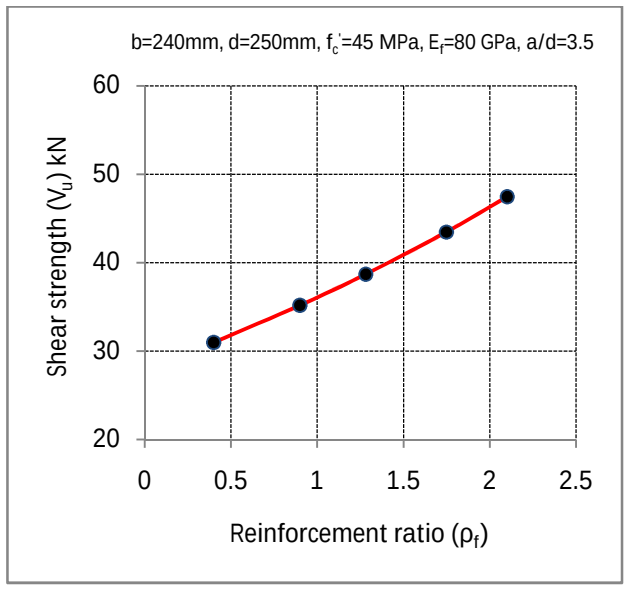

Figure(10). Effect of the reinforcement ratio on shear strength of FRP beams.

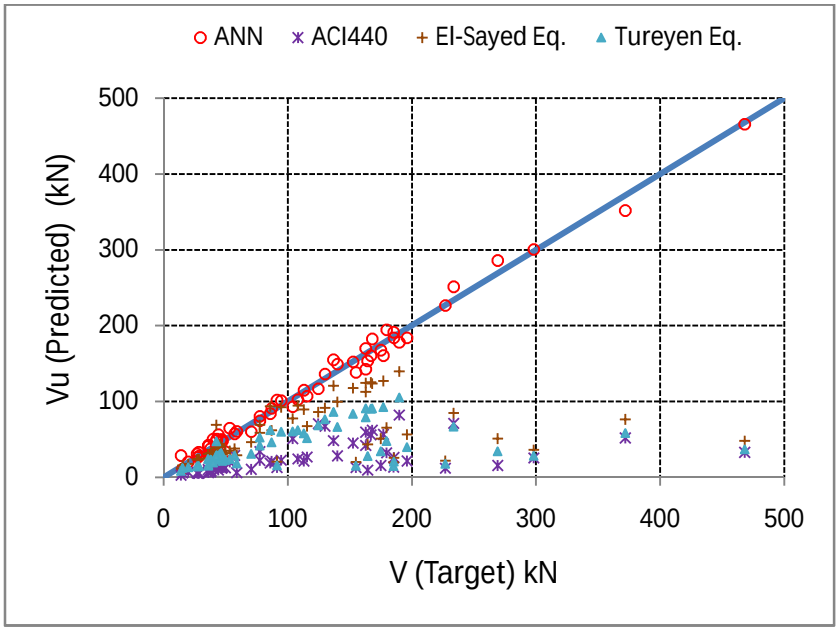

Figure (11). Comparison experimental and predicted values for training data Set.

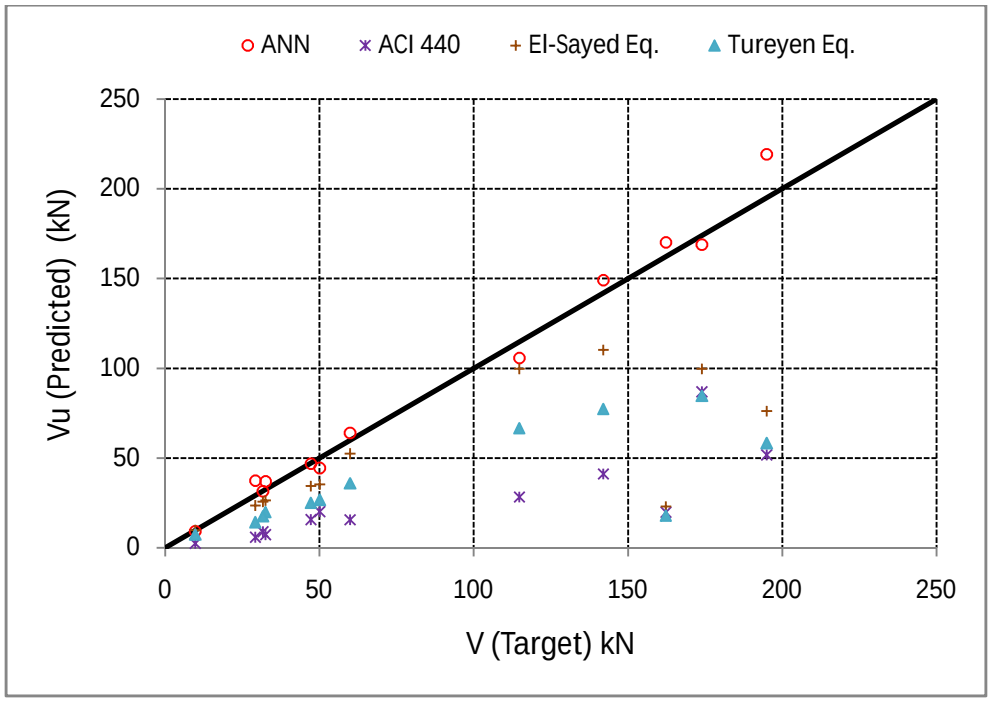

Figure (12). Comparison experimental and predicted values for testing data Set.

9. References

[1] Bank .L.C., 2006, "Composites for Construction: Structural Design with FRP Materials", Book, John Wiley .

[2] Tan, K.H., 2003, "Fibre-Reinforced Polymer Reinforcement for Concrete Structures", Book, World Scientific Pub Co., 1528 pp.

[3] El-Sayed, A. K., El-Salakawy, E. F., and Benmokrane, B., 2004, "Evaluation of Concrete Shear Strength for Beams Reinforced with FRP Bars", 5th Structural Specialty Conference of the Canadian Society for Civil Engineering, CSCE, Saskatoon, Saskatchewan, Canada, June, 10p.

[4] El-Sayed, A. K., El-Salakawy, E. F., and Benmokrane, B., 2006, "Shear Strength of FRP Reinforced Concrete Beams without Transverse Reinforcement", ACI Structural Journal, 103 (2), pp.235-243.

[5] El-Sayed A.K., El-Salakawy E.F., and Benmokrane B., 2005," Shear Strength of Concrete Beams Reinforced with FRP Bars: Design Method, ACI-SP-230, USA, Nov, pp.955-974.

[6] Wegian F.M., Abdalla H.A., 2005, " Shear capacity of concrete beams reinforced with fiber reinforced polymers; Composite Structures, 71, pp. 130–138.

[7] Omeman Z., Nehdi M., El-Chabib H., 2008," Experimental study on shear behavior of carbon-fiber-reinforced polymer reinforced concrete short beams without web reinforcement", Canadian Journal of Civil Engineering, 35, pp.1-10.

[8] Jang R.S., Sun T. C., Mizutani E., 1997, " Neuro-Fuzzy and Soft Computing A Computational Approach to Learning and Machine intelligence", Book.

[9] Rafiq, M.Y., Bugmann, G. and Easterbrook, D.J., 2001,"Neural Network Design for Engineering Applications" Journal of Computers and Structures,79 (17), pp. 1451-1552.

[10] Hsu D.S., and Chung H.T., 2002, "Diagnosis of Reinforced Concrete Structural Damage Base on Displacement Time History using the Back-Propagation Neural Network Technique", Journal of Computing in civil engineering, 16(1), pp.49-58.

[11] Cladera A., Mar A.R., 2004, "Shear design procedure for reinforced normal and high-strength concrete beams using artificial neural networks", Part II: beams with stirrups, Journal Engineering Structure, 26, pp. 927-936.

[12] Mehmet Inel, 2007, "Modeling Ultimate Deformation Capacity of RC Columns Using Artificial Neural Networks", Engineering Structures.; 29, pp. 329–335.

[13] Abdallaa J.A., Elsanosib A., Abdelwahab A., 2007, "Modeling and Simulation of Shear Resistance of R/C Beams Using Artificial Neural Network", Journal of the Franklin Institute 344, pp. 741-756.

[14] Guide for the Design and Construction of Concrete Reinforced with FRP Bars (ACI 440.1R-03), Reported by ACI Committee 440, 2003.

[15] Tureyen, A. K. and Frosch, R. J., 2003, “Concrete Shear Strength: Another Perspective” ACI Structural Journal, 100 (5), pp. 609-615.

[16] El-Sayed, A. K., El-Salakawy, E. F., and Benmokrane, B., 2005, “Shear Strength of One-way Concrete Slabs Reinforced with FRP Composite Bars”, Journal of Composites for Construction, ASCE, 9(2), pp.147-157.

[17] El-Sayed, A. K., El-Salakawy, E. F., and Benmokrane, B., 2006, “Shear Capacity of High-Strength Concrete Beams Reinforced with FRP Bars”, Submitted to ACI Structural Journal,,103(3), pp.383-389.

[18] El-Sayed, A. K., 2006, "Concrete Contribution to the Shear Resistance of FPR-Reinforced Concrete beams" PhD Thesis, Sherbrook University,.

[19] Gross, S. P., Dinehart, D. W., Yost, J. R., and Theisz, P. M., 2004, “Experimental Tests of High-Strength Concrete Beams Reinforced with CFRP Bars”, Proceedings of the

4th International Conference on Advanced Composite Materials in Bridges and Structures (ACMBS-4), Calgary, Alberta, Canada, July 20-23, 8p.

[20] Gross, S. P., Yost, J. R., Dinehart, D. W., Svensen, E., and Liu, N.,2003, "Shear Strength of Normal and High Strength Concrete Beams Reinforced with GFRP Reinforcing Bars", Proc. of the Int. Conference on High Performance Materials in Bridges, ASCE, 426-437.

[21] Razaqpur, A. G., Isgor, B. O., Greenaway, S., and Selley, A.,2004, "Concrete Contribution to the Shear Resistance of Fiber Reinforced Polymer Reinforced Concrete Members", Journal of Composites for Construction, ASCE, 8(5), pp. 452-460.

[22] Tariq, M., and Newhook, J. P.,2003, "Shear Testing of FRP reinforced Concrete without Transverse Reinforcement," Proceedings of CSCE 2003-Anuual Conference, Moncton, NB, Canada, 10p.

[23] Tureyen, A. K., and Frosch, R. J.,2002, "Shear Tests of FRP-Reinforced Concrete Beams without Stirrups", ACI Structural Journal, 99(4), pp.427-434.

[24] Yost, J. R., Gross, S. P., and Dinehart, D. W. 2001, "Shear Strength of Normal Strength Concrete Beams Reinforced with Deformed GFRP Bars", Journal of Composites for Construction, ASCE, 5(4), pp. 263-275.

[25] Deitz, D. H., Harik, I. E., and Gesund, H.,1999, "One-Way Slabs Reinforced with Glass Fiber Reinforced Polymer Reinforcing Bars", Proceedings of the 4th International Symposium, Fiber Reinforced Polymer Reinforcement for Reinforced Concrete Structures, MI., pp. 279-286.

[26] Alkhrdaji, T., Wideman, M., Belarbi, A., and Nanni, A.,2001, "Shear Strength of GFRP RC Beams and Slabs", Proceedings of the International Conference, Composites in Construction-CCC 2001, Porto/Portugal, pp. 409-414.

[27] Baughman, D.R. and Liu, Y.A., 1995, "Neural Network in Bioprocessing and Chemical Engineering", Book, Academic Press, San Diego, CA.

[28] CSA. 2002. Design and construction of building components with fiber-reinforced polymers. Standard S806-02. Canadian Standards Association.

[29] Yang, K.H., Chung, H.S., Lee, E.T., and Eun, H.C., 2003, "Shear Characteristics of High-Strength Concrete Deep Beams without Shear Reinforcements. Engineering Structures, 25(10), pp 1343–1352.

10.Nomenclature

V_u: Shear strength.

V_{cf}: The shear resistance of members reinforced with FRP bars as flexural reinforcement.

V_c: The shear strength provided by the concrete.

V_s: The shear strength provided by steel.

b_w: Width of the specimen.

d: Effective depth of the specimen.

E_f: Modulus of elasticity of fiber reinforced polymers

ρ_f: Reinforcement ratio of flexural FRP.

n_f: ratio of the modulus of elasticity of FRP bars to the modulus of elasticity of concrete.

f'_c: Compressive strength of concrete.

f_y: Yield strength of the mesh wire.

a/d: Shear span to depth ratio.

β_1: function of the concrete compressive strength (f'_c).

Experimental Investigation of Variation in Mechanical and Microstructural Properties Along the Length of Similar AA6063 FSW.

Adnan A. Ugla

Mechanical Engineering Department

College of Engineering

Thi-Qar University

Abstract

In this paper, 6063-T4 Al-alloy sheets with dimensions (6x90x200) mm were joined via friction stir welding (FSW). Tow sheets were but welded with square mating edges. The rotating welding tool made of tool steel heat-treated to HRC 60**.** The temperature distribution had been investigated experimentally with constant revolution speed and constant linear speed. A digital reader of twelve channels was used to read and record the temperature with time at each channel as an excel table. Nine K-type thermocouples were positioned along the weld length. The mechanical properties were evaluated (such as tensile strength , microhardness, and microstructure tests) at room temperature in several positions along the length of the joint. The results show that the max. temperature was conducted at the end of the weld to be 375C˚. The relationships between the peak temperature and the time, distance from start, microhardness, tensile strength, and microstructure were discussed. The hardness of the stirred zone was more than the base metal hardness due to refinement of grains by friction stir process. The strength and hardness of the FSW were as min. at the end of the weld due to increasing in heat input to the joint at this region which lead to grain growth at the microstructure of last region.

Keywords: friction stir welding, Temperature distribution, mechanical properties, friction stir process.

المستخلص

في هذا البحث استعملت سبيكة المنيوم من نوع (6063-T4 Al –alloy) على شكل الواح بالأبعاد (6 x 90 x 200) ملم، تمت تهيئتها بشكل تقابلي و بحافات قائمة ثم تم وصلها باستعمال طريقة اللحام بالاحتكاك والتحريك (FSW). أداة اللحام المستعملة تم تصنيعها من فولاذ العدة المقسى الى حد HRC 60. تم عملياً دراسة توزيع درجات الحرارة بثبوت السرعة الدورانية و الخطية لأداة اللحام. تم استعمال قارئ و مسجل درجات الحرارة من النوع الرقمي ذو اثنتي عشر قناة

و الذي يقرأ الحرارة مع الزمن ويتم عرضها على جهاز الحاسوب على شكل جدول ببرنامج معالج الجداول Excel .استعملت في البحث تسعة مزدوجات حرارية من النوع K **وزعت بشكل متساوي على طول وصلة اللحام**. بعد ذلك تم تقييم المواصفات الميكانيكية على طول وصلة اللحام مثل اختبار الشد و الصلادة المجهرية و كذلك فحوصات البنية المجهرية. النتائج أظهرت ان درجة الحرارة العظمى التي حصلت خلال عملية اللحام كانت 375م° في آخر منطقة من عملية اللحام. بعد ذلك تمت مناقشة العلاقات بين تنوع درجات الحرارة و الوقت و المسافة عن بداية اللحام و الصلادة المجهرية و كذلك البنية المجهرية. **ان صلادة منطقة اللحام** (stirred zone) كانت أعلى من صلادة المعدن الأساس وهذا نتج عن عملية التنعيم في الحجم الحبيبي الذي حصل نتيجة عملية الاحتكاك و الدعج والتحريك.**ان مقاومة للشد العظمى و كذلك الصلادة** كانتا كأقل قيمة عند آخر منطقة في اللحام بسبب الزيادة في الحرارة الداخلة الى هذه المنطقة نتيجة الحرارة المتراكمة و التي أدت إلى زيادة في الحجم الحبيبي في هذه المنطقة.

1. Introduction

Friction stir welding (FSW) is an efficient solid joining process that has numerous potential applications in many domains including aerospace, automotive and shipbuilding industries as well as in the military. It combines frictional heating and stirring motion to soften and mix the interface between the two metal sheets, in order to produce fully consolidated welds. One of its main qualities lies in the possibility of joining materials previously difficult to weld, and to offer excellent mechanical properties [1]. The weld is made by inserting a usually threaded pin or nib into the faying surface of the butt welded parts. The nib is typically slightly shorter than the thickness of the workpiece and its diameter is approximately the thickness of the workpiece . The pin is mounted in a shoulder that may be three times the diameter of the nib. The nib and shoulder are pressed against the workpiece, rotated at several hundred revolutions per minute, and advanced along the faying surface. FSW has been primarily used on aluminium alloys (e.g. alloy series 2000, 6000, 7000 and numerous Aluminum – Lithium alloys) and produces nearly defect-free welds for such demanding applications as space hardware at lower cost than conventional fusion welds [2,3]. The low distortion solid –phase welds exhibit metallurgical and mechanical fusion welds achieved by arc processes and additional studies have concluded that the FSW process could significantly improve weld quality and lower production costs associated with welding [4]. The problems related to the presence of brittle inter-dendritic and eutectic phases are eliminated [5-6]. The thermo-mechanical affected zone is produced by friction between the tool shoulder and the plate top surface, as well as plastic deformation of the material in contact with the tool [4]. Systematic welding trials have covered various Aluminum Alloys according to the (2XXX(Al-Cu), 5XXX (Al-Mg), 6XXX(Al-Mg-Si), 7XXX (Al-Zn) and 8XXX (Al-Li) series alloys and each a high level of weld quality and process repeatability has been observed [7].

In the present paper, 6063 Al- alloy sheets (with 6 mm thickness) were joined via friction stir welding (FSW), and the temperature distribution had been investigated experimentally (with constant revolution speed and constant linear speed) along the weld length. The mechanical properties were evaluated by means of tensile and hardness tests at room temperature along the weld length in addition the material microstructure and the different phases were investigated by means of optical observation in different sections along the length of the produced joints.

2. Experimental procedure

2-1. Materials

The material under investigation was a 6063 Al-Mg-Si alloy as rolled sheets of 6 mm thickness with the composition shown in Table (2-1)

Table (2-1).Chemical composition of Al-Mg-Si alloy [8,9].

Element composition %	Si	Fe	Cu	Mn	Mg	Zn	Cr	Al
ASTM Standard	0.2-0.6	0.35	0.1	0.1	0.45-0.9	0.1	0.1	Rem.
As measured	0.21	0.15	0.03	0.01	0.40	0.01	0.01	Rem.

In order to investigate mechanical properties of the workpiece before welding process, a series of tensile tests had been performed to determine the max. tensile strength and elongation. Tensile specimens were machined according to ASTM standard. Tensile results for the material before welding process are listed in Table (2-2), while standard tensile test results for different classes are given in Table (2-3).

Table (2-2).Tensile test results for present work.

6063 Al-alloy	Ultimate tensile strength MPa	Hardness HV Mpa	Elongatio %
	142	63.5	18

Table (2-3). Standard tensile test results for Al-Mg-Si alloy [8].

Temper	Proof strength 0.2% MPa	Tensile strength MPa	Elongation %	Hardness HV
0	50	100	27	85
T4	90	160	21	50
T6	210	240	14	80

From tables above, it is obvious that the selected alloy was solution heat-treated and naturally aged to a substantially stable condition, hence the selected alloy is 6063-T4.

2-2. Configuration of tool and workpiece

A schematic of the welding sequence for a FSW process is shown in Figure (2-1). A specially cylindrical (heat-treated to HRC 60 tool steal) tool with a probe extending from the shoulder. The probe may have a diameter one-third of the cylindrical tool and typically has a length slight less than the thickness of the workpiece [10]. A welding tool comprised of a shank, a shoulder and pin is fixed in a milling machine holder and is rotate along its longitudinal axis. Workpiece material is held firmly in place in a fixture as shown in Figure (2-2). Two 6063-T4 Al-alloy plates, each with a dimension of 200x90x6 mm were butt welded in the adapted vertical milling machine perpendicularly to the rolling direction Figure (2-3). The two plates, with square mating edges, are fixed on a rigid backing-plate, and a clamp or anvil prevents the workpiece from spreading or lifting during welding. The rotating welding tool is slowly plunged into the workpiece until the shoulder of the welding tool touched the upper surface of the plate material.

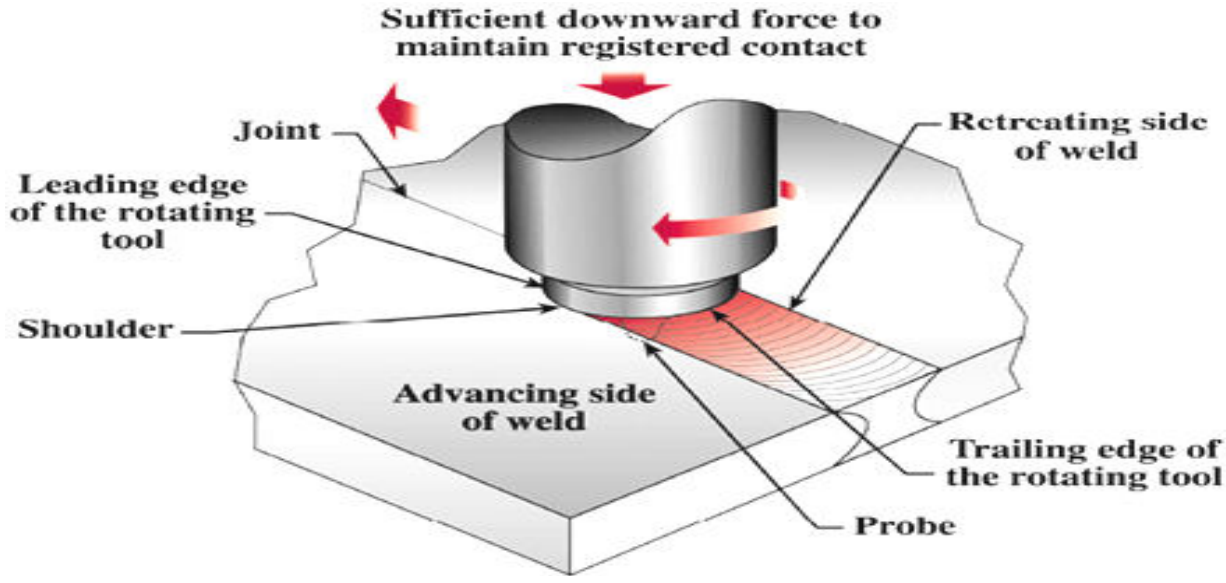

Figure (2.1). Schematic representation of FSW of a butt joint [4].

Figure(2-2).Shows (a) thermocouple reader connect with 9- K type thermocouples,(b) thermocouples distributes along the workpiece surface, and (C) The tool move with rotational speed 1400 rpm and travel speed 110 mm / min.

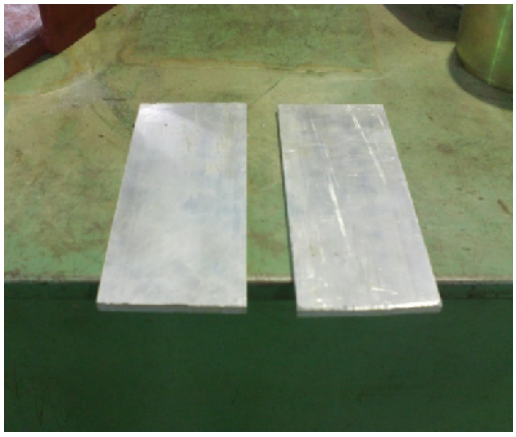

Figure (2-3).Two 6063-T4 Al-alloy plates to be welded before and after FSW.

The tool rotate at the selected revolutional speed for about (30-45) seconds dwell period for preheating [11]. Then the welding tool is forcibly traversed along the joint line until the end of the weld is reached. After that the welding tool has been retracted and the pin of the welding tool leaves a hole in the workpiece at the end of the weld. Table 2-4 shows the processing conditions with constant the revolutionary pitch (welding speed/rotating speed).

Table (2-4). The welding conditions.

Rotating speed RPM	Welding speed mm/min	Revolutionary pitch mm/rev.
1400	110	0.0785

2-3. Measurement of temperature distribution

Nine positions were pointed out on one face of the plates to be welded on the same side and equal distance along the line of the welding as shown in Figure (2-4).

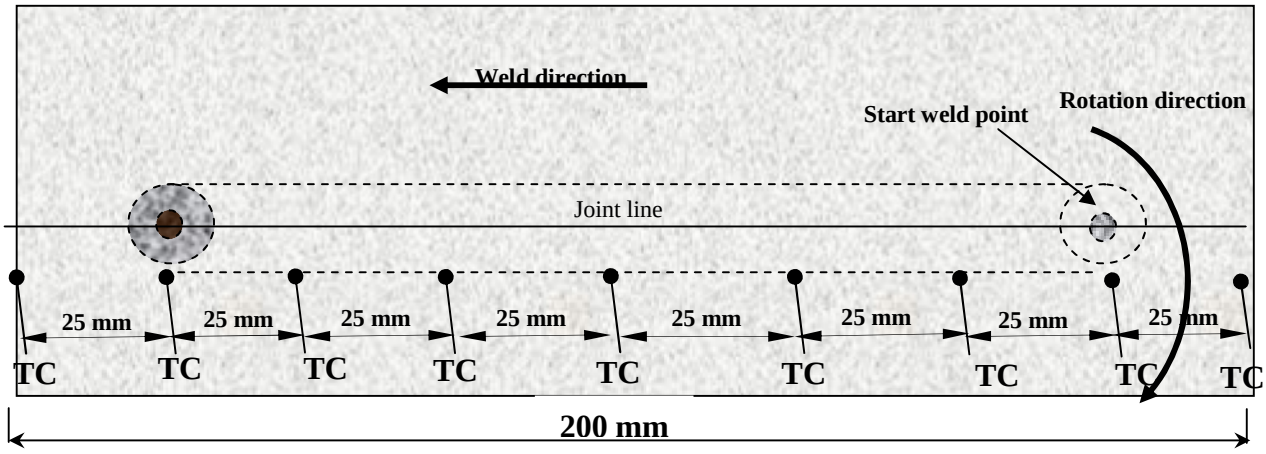

Figure (2-4). Layout of the thermocouples on the workpiece surface.

K-type thermocouples with diameter of 1mm were used. The sensing head of the thermocouples is approximately 1mm long. A drill machine was used to make holes of 1 mm diameter with 1mm depth in the nine positions [12,13]. The rotational speed and the moving speed direction of the tool are shown in Figure (2-4) and the thermocouples are lined on the same side of the setup workpiece with a distance (11 mm) from the joint line, which means that the thermocouples are positioned at the rim of the shoulder when the tool passes by the thermocouples without destroyed them. A digital reader of twelve channels was used to read and save the temperature readings at the same time. Nine-thermocouples were connected to the reader. In the start it read the temperature of the surrounding , then the temperatures will increase during the tool movement and the reader will save these temperatures every one second. The readings were saved in separated Ram which can be inserted in computer to display on the monitor as an axel table.

2-4. Mechanical tests

In order to investigate mechanical and microstructural properties of welded joints and to evaluate the effect of cumulative temperature on the properties, some of destructive tests have been conducted.

2-4-1 Tensile test

Tensile specimens were machined from the welds according to ASTM sub-size specimen geometry shown in Figure (2-5). The tensile tests were performed in order to evaluate the mechanical properties in the different welding positions which were calculated in longitudinal direction. The test was carried out at room temperature using testing machine in a direction transversal to the welding line (transverse specimens). The results of tensile strength and microhardness were averaged of three specimens at each location.

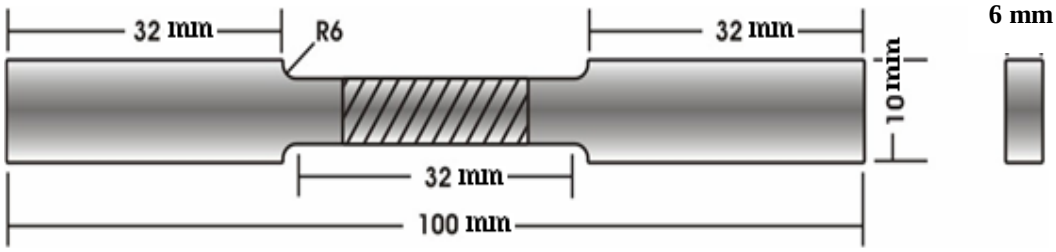

Figure (2-5). ASTM sub-size sample for tensile test.

2-4-2 Microstructure test

Microstructure investigation of welded joints specimens for the microstructure analyses were prepared by standard metallographic techniques and etched with killer's reagent to reveal the grain structure. The microstructure and different phases were observated in the centre of the joint (stirred zone).

2-4-3 Microhardness test

The same specimens of metallurgical tests were prepared for the microhardness measurements were made at mid-section of the joint every (25mm). Microhardness was employed with load (0.5 Kg) by using a (Micro - Veckers Hardness system CV-400 DM) microhardness tester accordance with ASTM.

3. Results and discussions

3-1 Temperature-Time history with moving heat source

Variation of peak temperature is shown in Figure (3-1), which represents a temperature – distribution along the longitudinal direction for nine nodes shown in Figure (2-4). Region 1 shows plunging and dwell period in which the tool rotate at the same position for 35 seconds with rotational speed of 1400 rpm to increase the base metal temperature (pre-heating) as shown in Figure (3-2 a). Region 2 represents the variation of temperature during tool movement. It is obvious that the temperature increase at the beginning due to increase of heat input by dwell, then the temperature decrease and then it increase. The reason of the first increasing in temperature is that the tool is staying near dwell starting position and when the tool moves it will enter the cold area as shown in Figure (3-2 b), therefore, the temperature reduces. After that the effect of heat accumulation will contribute by raising the temperature Figure (3-2 c). Figure (3-1) shows that the temperature at the end of the tool movement is the highest. Figure (3-3) shows the temperature variation which record by using thermocouple reader by means thermocouple distribution along the length of welded joint. It was obvious that the temperature rises slightly until get max. at the location 8 due to cumulative heat with movement of tool during welding along the joint length as shown in Figure (3-2 d).

3-2 Microhardness test results

Hardness profiles for each sample along the weld length are shown in Figure (3-4). From the figure it was obvious that there is an increase in the hardness across the welds compared to the value of the base metal (HV_{500g}=63.5). It is thought that the increase in hardness was due to equiaxed structure or reprecipitation of the solid solution. Furthermore, it can see that hardness value decrease with an increasing in the distance which mean that the temperature become max. at this position (375 C˚). The hardness variation along the weld length with variation in temperature during welding time as shown in Figure (3-4) and Figure (3-5). The decrease in hardness at position 8 (HV_{500g}= 60.6) may belong to the dissolution of precipitates into solution and subsequently the weld cooling rates do not favour nucleation and grains are growing in all the stirred zone as shown in paragraph (3-4).

3-3 Tensile test results

Figure (3-6) shows the ultimate tensile strength at selected positions with constant distance (25 mm) along the weld length. Many of researchers [10,14,15] emphasized that there is a reverse effect between the max. tensile strength and travel speed of the tool, and they show that the max. tensile strength decreases with increasing of rotational speed of the tool, the reason may belong to the heat input to the workpiece so that the strength decrease with increase of heat input (increase rotational speed or decrease of travel speed) and it increase with decrease of input heat (decrease rotational speed or increase of travel speed). In the present case the rotational speed and travel speed were taken as constant values (constant revolutionary pitch) Table (2-4). From the Figure (3-7) it is obvious that the tensile strength decrease with the length of welded joint in the direction of welding. It is believed that the decrease in weld strength with increasing the distance along weld direction was attributed to increase in heat input per unit length of weld due to cumulative heat during welding, therefore, the position (8) had temperature 375C˚ and the position 2 developed high temperature (315 C˚) due to dwell period, for this reason the tensile strengths were min. at these positions, because the high temperature at these positions resulted in more over aging of the weld zone and produce change in microstructure.

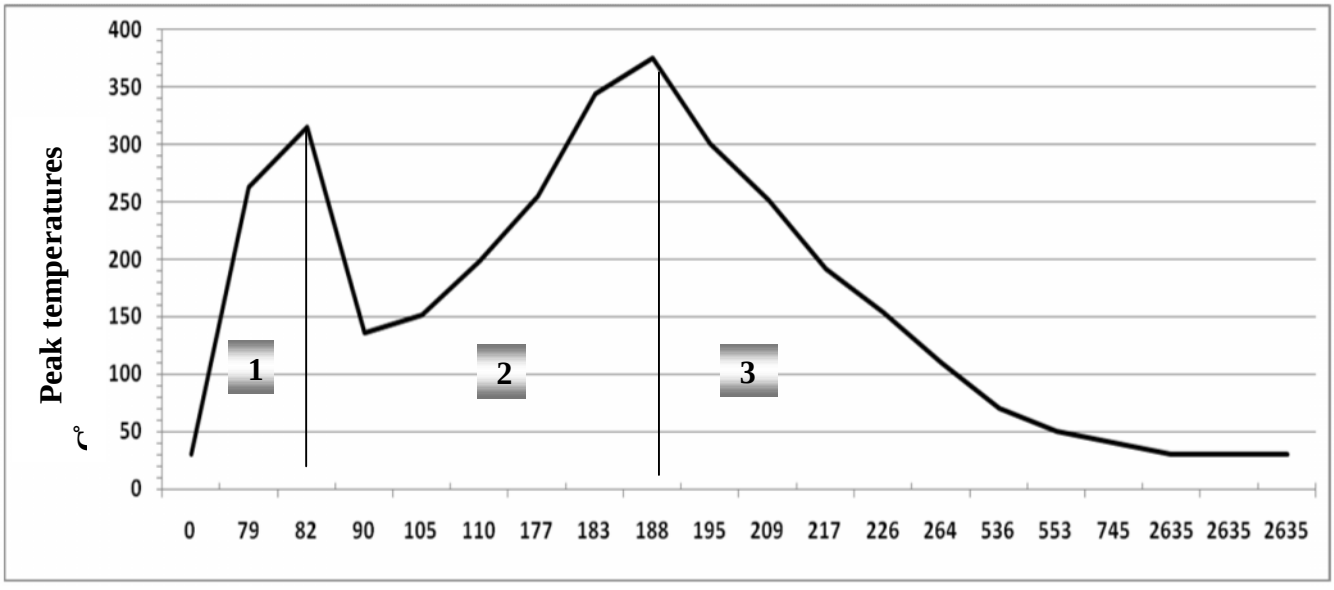

Figure (3-1). Peak temperature variation during welding and cooling.

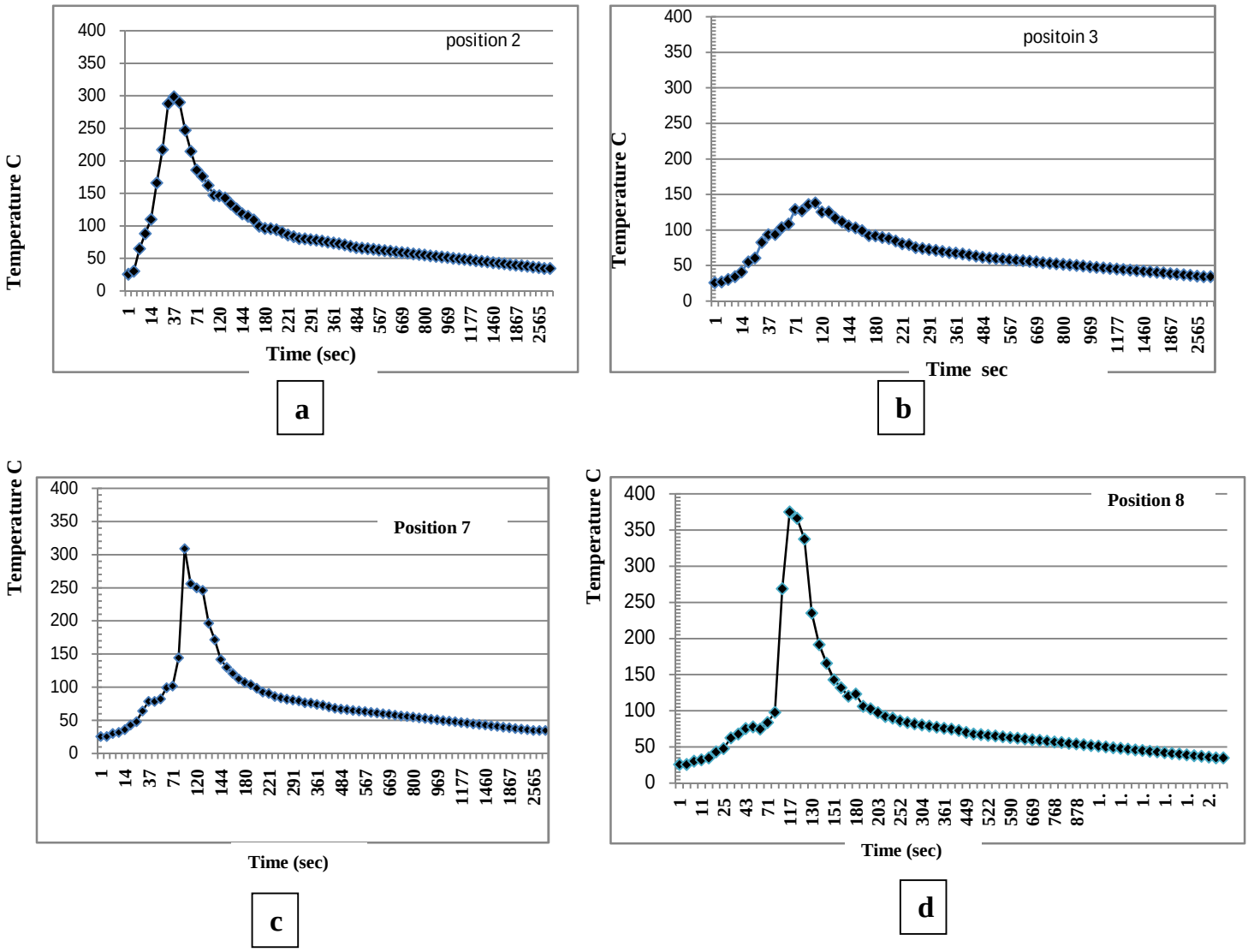

Figure (3-2). Thermal history in thermocouple positions (2, 3, 7 and 8) along the weld length show temperature profile versus welding time.

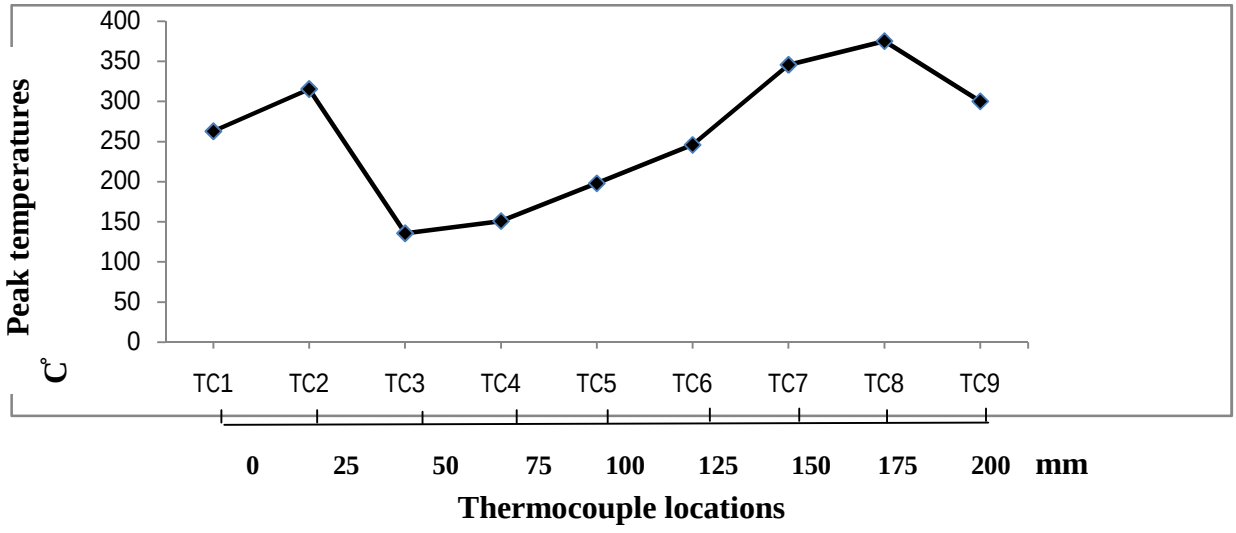

Figure (3-3). Peak temperatures profile in FSW along the weld length.

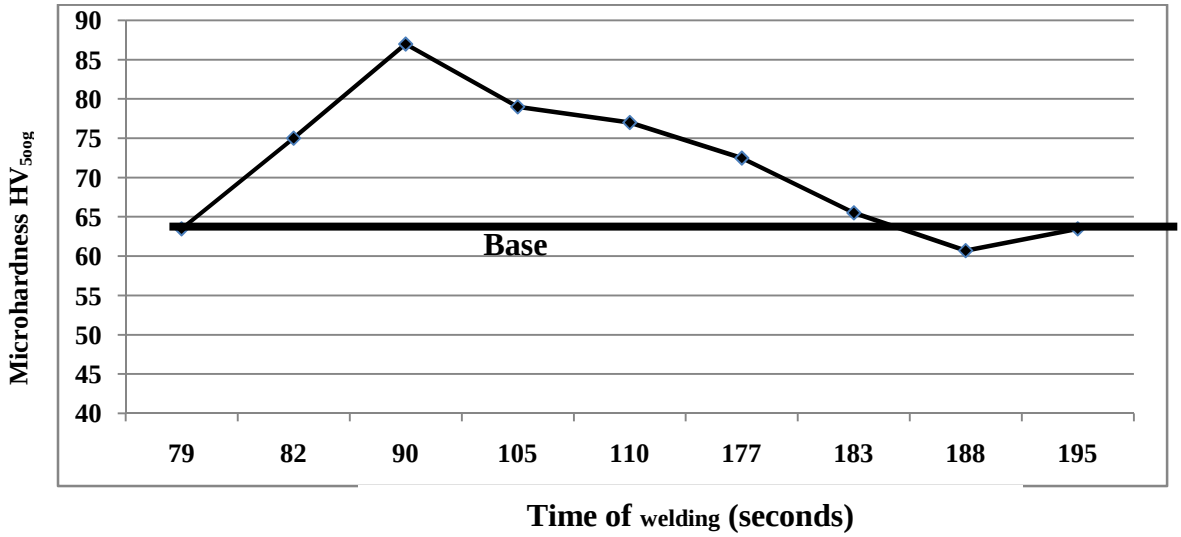

Figure (3-4). Microhardness variation during FSW period.

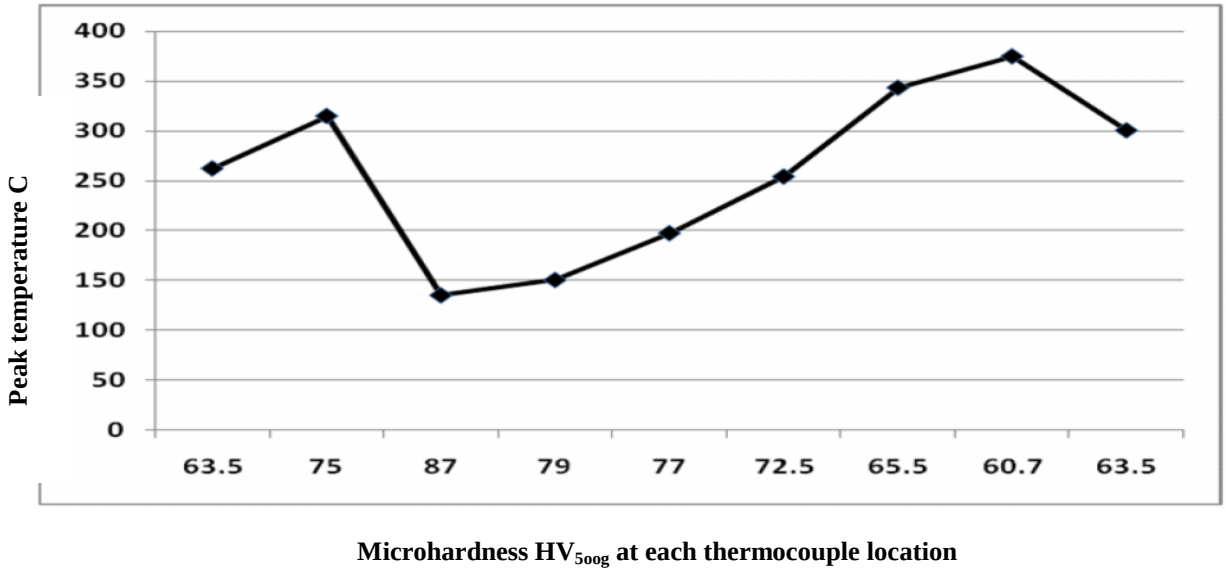

Figure (3-5). Microhardness variation versus temperatures.

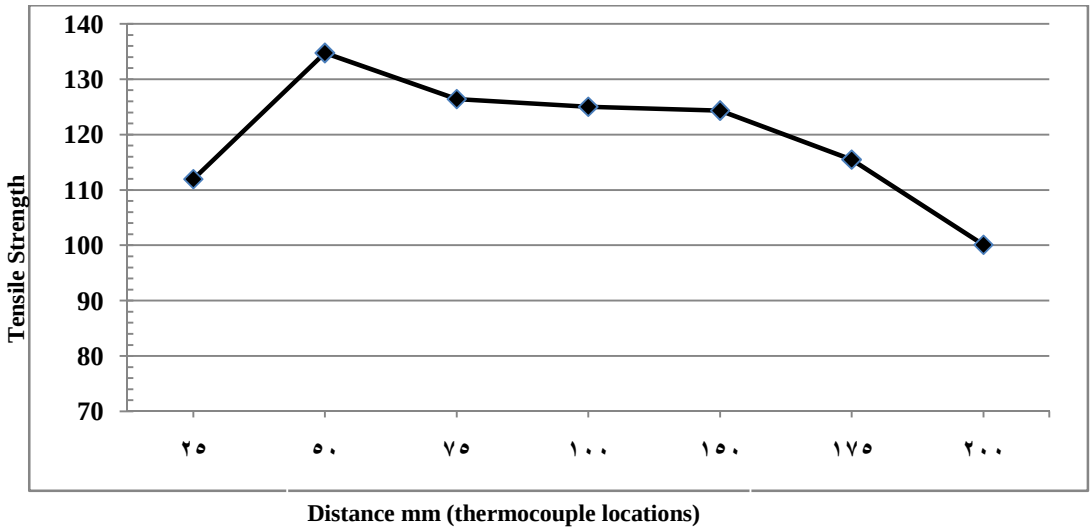

Figure (3-6). Max. tensile strength variation along weld length.

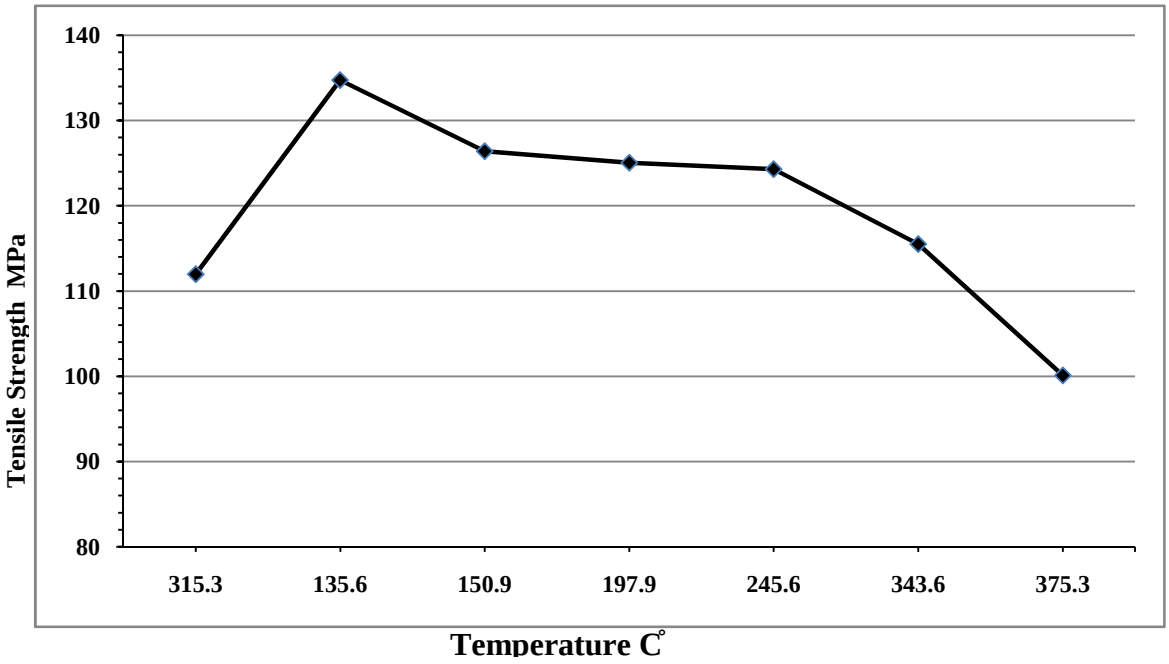

Figure (3-7). Max. tensile strength versus peak temperature at each certain position along weld length.

3-4 Microstructure test results

Figure (3-8) shows the microstructure of the base metal before welding. It is obvious that the base metal exhibited elongated grains due to rolling process.

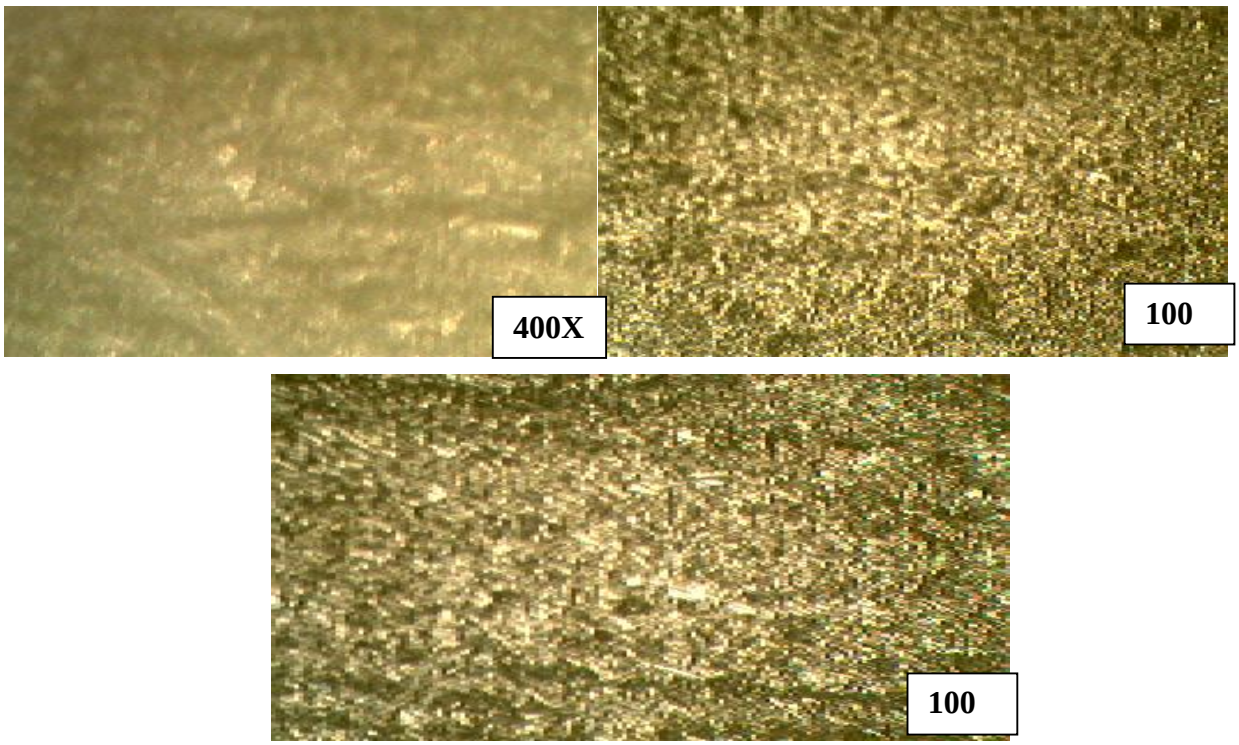

Figure (3-8). Show the elongated grains of the base metal microstructure.

Figure (3-9) shows the microstructure of the weld zone in FS zone along the length of the joint. From the figure it was clear that the grains had produced at the stirred zone to get refined grains at the weld centre due to friction stir process see Figure (3-9 positions 3, 4, 5, and 6). But the cumulative heat during FSW which reaches to about 375C˚ at end of tool movement affect the grains to grow, therefore, the grains are equiaxed and large Figure (3-9 positions 7&8). It is known that the Al-Si-Mg alloy may be recrystallized and grow at temperature range (200-330)C˚ [16]. The experimental rsults show that the achieved temperature during FSW exceeded 370 C˚. Although the growth time was short respective to that allowed for grain-growth in Al-structure see Figure (3-2 d), furthermore, it leads to overage of the grains and growth which affect the properties of the joint along the weld length as discuss in paragraphs (3-1, 3-2, and 3-3). From the results it is necessary to carry out heat treatments for homogenization the properties along the weld length in FSW processes.

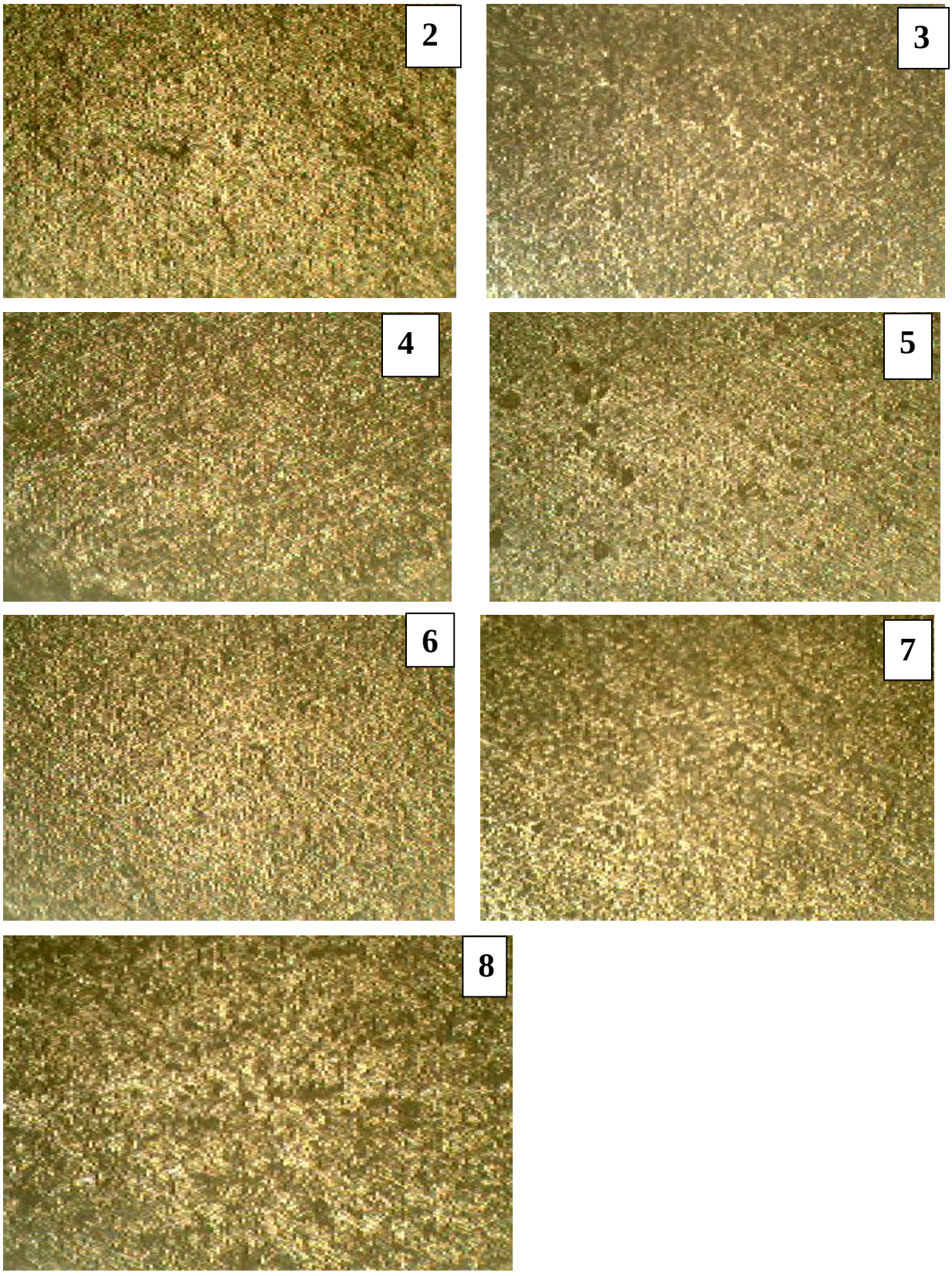

Figure (3-9). Microstructures of stirred zone along the weld length 100X. The sample (2) represents the beginning of plunging and stirring (first dwell) and the sample (8) represent the end of weld (second dwell).

4- Conclusions and further recommendations

4-1 Conclusions:

According to the results of the present work several conclusions can be written:

1- The 6063-T4 Al-alloy can be readily friction stir welded.
2- Maximum temperature in FSW will appear at the end of the tool movement due to cumulative heat.
3- Mechanical properties variate along the length of joint as a result of variation in heat input to the weldment.
4- Refinement of the weld zone grains was very clear which lead to increase of microhardness of the stirred zone above the base metal hardness.
5- Grain growth appear at the end of the weld due to high temperature at this region , which cause decreasing in mechanical properties (hardness and strength).
6- The max. tensile strength of the FSW is about (--)% of the base metal strength and strength values variate along the weld length, where the min. value of tensile strength is pointed at the end of weld (second dwell).

4-2 Recommendations:

1- Make a mathematical model for temperature distribution (theoretical procedure) and compare with the present experimental work.
2- Use robotic welding machine by which can control the change in rotational speed and travel speed in order to control on the heat input to the workpiece as constant amount by decreasing the rotational speed or increasing the travel speed, to withstand the cumulative heat effect.
3- Use the same procedure but for other types of joints (such as fillet or lap) by using the same material.
4- Use low carbon steel instead of Al and compare the results of variation in properties along the weld length.

5. References

[1] Assidi , M., Fourment, L., Guerdoux, S., and Nelson, T**.,** 2010**," Friction Model for Friction Stir Welding Process Simulation: Calibrations from Welding experiments."** International Journal of Machine Tools &Manufacture ,No. 50, PP143-155.

[2] Guerra , M., Schmidt, C.,McClure, J.C., Murr, L.E., and Nunes, A.C., 2003 **,"Flow Patterns During Friction Stir welding"**, Materials characterization, No. 49, PP 95 – 101.

[3] Cavaliere , P., Santis, A. De, Panella, F., Squillace, A., 2009, **"Effect of Welding Parameters on Mechanical and Microstructural Properties of AA6082-AA2024 Joints Produced by Friction Stir Welding."**Materials and Design, No. 30, PP 609-616.

[4] Farahmand , Bahram, 2001, **"Fracture Mechanics of Metals, Composites , Welds, and Bolted Joints application of LEFM , EPFM, and FMDM Theory"**, Kluwer Academic Publishers, Bston, Dordrecht, London,pp(287-298).

[5] Cavaliere , P., Cabibbo , F. Panella , Squillace , A**.** , 2009,**"2198 Al-Li Plates Joined by Friction Stir Welding: Mechanical and Microstructural behaviour."**Materials and Design, No. 30, PP 3622-3631.

[6] Rhodes , C.G., Mahoney, M.W., Ringel , W. H., 1997, **"Effects of Friction Stir Welding on Microstructure of 7075-Al"**, Scripta Mater, No. 36, PP 69-75.

[7] Dawes , C. J., 1999, "**TALAT Lecture 4410 Friction Stir Welding"** The Welding Institute. Abinton Hall, Cambridge. TWI.

[8] Aluminum Association , MATTER Project, 2001.

[9] Ross , Robert B. , 1980, " **Metallic Materials Specifications Handbook**" 3rd Edition, London, New York E.F.N. Spon.

[10] Yousif , M. Akab , 2007, **"Investigation of mechanical and Microstructural characteristic of Friction Stir Welded Joints."**Ph. D. Thesis, University of Baghdad.

[11] Al-Bayaty , S. D. Ridha**,** 2008,**"Theoretical and Experimental study for Measurements of Residual Stresses Induced By Friction Stir Welding and Investigation of Stress Relieve By Vibration in Aluminum Alloy"** Ph. D. Thesis, University of Baghdad.

[12] Hussein , S.G., 2008**, "Experimental Investigation of Temperature Distribution for Stir Friction Welding"**, M.Sc. Thesis, University of Baghdad.

[13] Yeong , M. H. , Zong, W.K.,Yuang , C.C., and Hung, H.Hsu, 2008**, "Experimental Study on Temperature Distributions Within The Workpiece During Friction Stir Welding of Al-Alloy"**, International Journal of Machine Tools &Manufacture, No. 48, PP 778-787.

[14] Vural , M., Ogur,A., Cam,G., Ozarpa , C. , 2007,"**On the Friction Stir Welding of Aluminium Alloy EN AW 2024-0 and EN AW 5754-H22**" International Journal NO. 28, pp 49- 54.

[15] Liu , H.J., Fujii , H., Maeda, M., Nogi , K. , 2003, "**Michanical properties of Friction Stir Welding Joint of 1050-H24 Al-Alloy**" Science and technology of welding and Joining Vol. 8, No. 6,.

[15]الخزرجي، د. قحطان خلف ،1989، "**المعاملات الحرارية للمعادن والسبائك الحديدية و اللاحديدية**" وزارة التعليم العالي و البحث العلمي، جامعة بغداد ،

Designing Different Shapes of Microstrip Antenna Using Genetic Algorithm

Sadiq K. Ahmed[1] , Zaid A. Abed Al-Hussein[1], Manaf K. Hussein[2]
[1]Department of Electrical Engineering, Al-Mustansiriya University
E-mail: zideassad79@yahoo.com [2] College of Engineering,
E-mail:manaf_kazim@yahoo.com

Abstract

In this work, Genetic Algorithm (GA) models have been built to design a microstrip antennas in various forms such as rectangular, equilateral triangle and hexagon patch antenna. The design problem can be defined to obtain the resonant frequency for a given the thickness of dielectric material and dimension of geometrical structure. This approach has a few advantages: giving a clearer and simpler representation of the problem, simplifying chromosome construction, and totally avoiding binary encoding and decoding to simplify software programming. The antenna designed using GA is implemented using MATLAB program and the analysis of antenna is implemented using Microwave Office software 7.1 produced in 2007.

المستخلص

في هذا البحث ، تم بناء الخوارزمية الجينية لتصميم الهوائيات الشريطية لاشكال مختلفة من الرقع منها المستطيلة والمثلثة متساوية الاضلاع والسداسية. مسألة تصميم تلك الاشكال يمكن تعرفها للحصول على التردد الرنيني بوجود سمك المادة العازلة والابعاد الهندسية للتركيب. هذه الطريقة تملك عدة فوائد منها: تعطي تمثيل واضح وبسيط للمسألة وبساطة تركيب الكروموسوم وتجنب بشكل كامل تشفير وحل النظام الثنائي لتبسيط البرنامج. صمم الهوائي باستخدام الخوارزمية الجينية والتي نفذت باستخدام برنامج الماتلاب وتم تحليل الهوائي باستخدام الميكرويف أوفس 7.2 المنتج عام 2007 .

1. Introduction

Microstrip antenna is one of the most popular type of antennas, since it is light weight, simple geometries, inexpensive to fabricate and can easily be made conformal to host body [1, 2]. These attractive features have increased the applications of the microstrip antennas recently and simulated greater efforts to investigate their performance. Microstrip antenna has very narrow bandwidth which is not exceed several of percent from the resonant frequency and the antenna operates in a vicinity of the resonant frequency. This needs very accurate

calculations for various design parameters of microstrip patch antennas. Patch dimensions for various microstrip patches is a vital parameter in deciding the utility of a microstrip antennas. CAD Models are generally developed using analytical, electromagnetic simulation, and measurement based methods. Accurate and efficient models for circuit components are essential for cost-effective circuit design.

Genetic Algorithm has a wide range in different applications. The antenna is one of these application .Chattoraj et al. (2006) have used genetic algorithm to the optimization of gain for a microstrip antennas with and without dielectric superstrate [3]. Chattoraj et al. (2007) have used genetic algorithm (GA) to the optimization of gain of microstrip antenna, fabricated on ferrite substrate, biased externally by a steady magnetic field [4]. Cengiz et al. (2008) have used GA to optimize the spacing's between the elements of the linear array to produce a radiation pattern with minimum SLL and null placement control[5].Yang et al. (2009) have produced the genetic algorithm in combined with Finite Element to design a single-patch broadband microstrip antenna [6].Yongsheng et al.(2009) have discussed the optimal design of line-tapered multimode interference devices using a genetic algorithm [7]. Reza et al. (2010) have investigated the effects of adaptive genetic algorithms (AGAs) on performance of optimization for tapered microstrip filter[8].

In this paper, the optimization of rectangular, triangular and hexagon is realized microstrip antenna responding to some constraints (frequency of the fundamental mode) some more advanced techniques, which give a global minimum, have been retained. One of these new approaches, more and more used, based on genetic algorithm (GA) method is well suited to our needs. The GA method, which is able to optimize different natural variables, is the most versatile approach. It can optimize the physical (dimension of the patch, thickness of substrate, and electric parameters (relative permittivity)).

2. Types of microstrip antennas

A microstrip antenna in its simplest configuration consists of a radiating patch on one side of dielectric substrate, which has a ground plane on the other side. The patch conductors, normally of copper and gold, can assume virtually any shape [1-2]. In this paper rectangular, triangular and hexagon microstrip antenna Figure (1) are designed using GA.

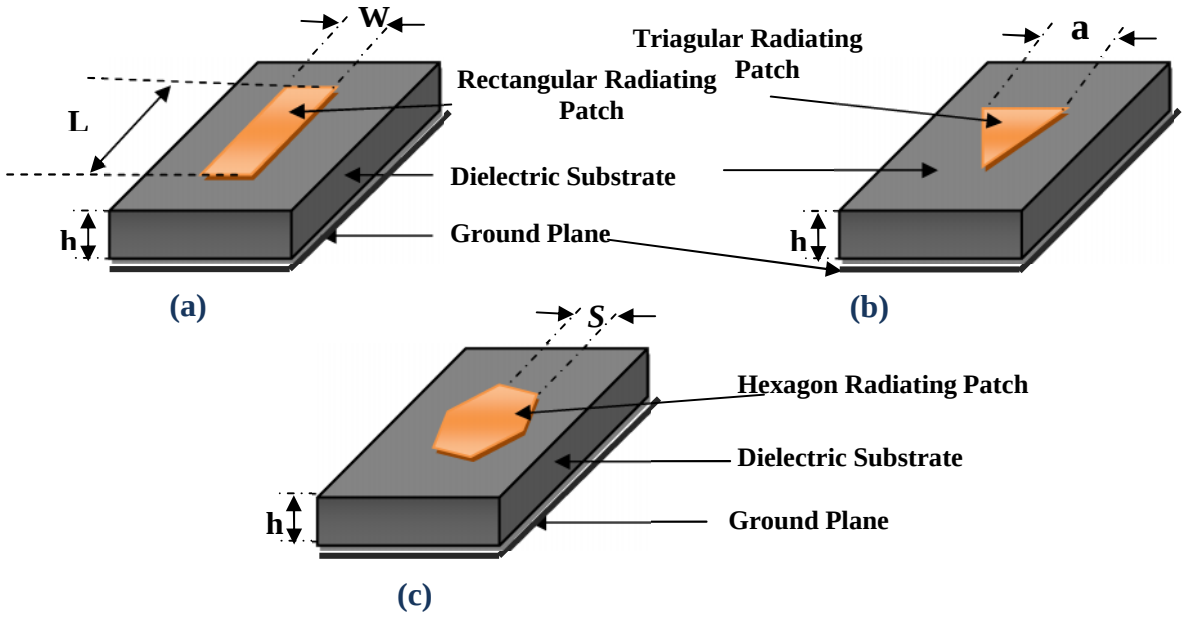

Figure (1). Microstrip antenna structure - a) Rectangular, b) Triangular, c) Hexagon .

3. Gentic algorithms (ga)

One of the most fundamental principal in our world is the search for an optimal state. Optimization is the process of modifying the inputs or characteristics of a device, mathematical process to obtain minimum or maximum of the output [9]. Genetic Algorithm is an Artificial Intelligence based methodology for solving problems. It is a non-mathematical, Non-deterministic, but stochastic process or algorithm for solving optimization problems [10, 11]. It is considered a sophisticated search algorithm for complex, poorly understood mathematical search spaces [12]. Genetic Algorithm (GA) is an optimization technique that attempts to replicate natural evolution processes in which the individuals with the considered best characteristics to adapt to the environment are more likely to reproduce and survive [12,13]. These advantageous individuals mate between them, producing descendants similarly characterized, so favorable characteristics are preserved and unfavorable ones destroyed, leading to a progressive evolution of the species. Artificial genetic algorithm aims to improve the solution to a problem by keeping the best combination of input variables. It starts with the definition of the problem to optimize, generating an objective function to evaluate the possible candidate solutions (chromosomes), the objective function is the way of determining which individual produces the best outcome. The next step is to generate an initial random population of *n* individuals called chromosomes that are symbolized by real weighting vector, where each position of the chromosome is called a gene and denotes a specific characteristic

(input variable). Therefore the combination of all the different characteristics of the real weights in the vector represents an individual who is a candidate for the solution [13].

Each chromosome is evaluated in the objective function and the best individuals are selected to survive for mating (parents), while the worse ones are discarded to make room for new descendants.

Random mutation is used to alter a certain percentage of the genes of the chromosomes. The purpose of mutation is to introduce diversity into the population, allowing the algorithm to avoid local minima by generating new gene combinations in the chromosomes. Finally, after mutation is done the new generation of chromosomes is evaluated with the objective function and used in the next iteration of the described algorithm.

The GA process could be simplified as following: 1) Initialize a random pool of Individuals. 2) Evaluate each Individual. 3) Choose couples (Mating). 4) Breed them together (Crossover). 5) Evaluate each Individual. 6) Selection. 7) Mutation. 8) If the pool has converged, or a number of pre-determined cycles have been completed, finish the cycle. If not, return to step #3[13,14].

In this paper coding and decoding avoided , operation directly works with complex numbers to simplify computing programming and to speed up computation. The resonance frequency of the antenna is obtained from the output of the GA for a chosen dielectric substrate and patch dimensions at the input side Figure (2).

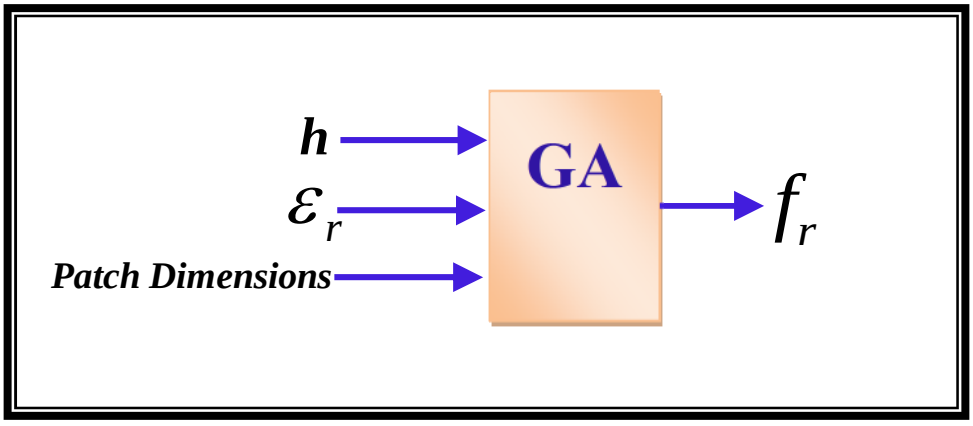

Figure.(2) GA Model for microstrip antenna design.

3-1-Construction of chromosomes

The using of genetic algorithms for design a microstrip antenna is corresponding to living beings and vectors represent chromosomes. Genetic algorithms were invented to manipulate a string of binary coding. Conventional genetic algorithms encode the parameters

in binary chromosomes and perform binary genetic operation. In this paper, chromosomes are represented directly by real weighting vector [12].

$$d = [d_1 d_2 d_3 \ldots d_n .. d_N] \quad (1)$$

Where d_n (known as a genetic material in a GA) which represents the dimensions of radiator (Length, width, radius,…) , height of the substrate material, and its relative permittivity.

3-2- Initial population

For fast convergence of genetic algorithms , the initial population was included.

3-3- Fitness function

In order to show the feasibility of this paper, the case of a rectangular, triangular and hexagon microstrip antenna form were studied.

3-3-1 Rectangular patch

It is assumed that the antenna has length (L), width (W), thickness (h) posed on a substrate of permittivity (ε_r). The objective is to find the values of the four parameters :(L, W, h, and ε_r), so that the antenna satisfies the constraint (a resonant frequency is assumed to be 10 GHz). The resonant frequency of TM_{nm} mode of the rectangular radiant element is[1]:

$$f_{nm} = \frac{c}{2(L + 2\Delta\ell)\sqrt{\varepsilon_e}} \quad (2)$$

Where:

c is velocity of light in free space($3*10^8$ m/s)

ε_e is effective dielectric constant

$$\varepsilon_e = \frac{\varepsilon_r + 1}{2} + \frac{\varepsilon_r - 1}{2}\left(1 + \frac{12h}{W}\right)^{-1/2} \quad (3)$$

$\Delta\ell$ is line extension

$$\Delta\ell = 0.412\,h\,\frac{(\varepsilon_e + 0.3)(W/h + 0.264)}{(\varepsilon_e - 0.258)(W/h + 0.8)} \quad (4)$$

3-3-2 Equilateral triangular patch

It is about an antenna of length side (a), thickness (h) posed on a substrate of permittivity (ε_r). The objective is to find the values of the three parameters :(a, h, and ε_r), so that the antenna satisfies the constraint (a resonant frequency of 10 GHz).

The resonant frequency of TM mode of the triangular radiant element is[1]:

$$f = \frac{2 * c}{3 a_e \sqrt{\varepsilon_e}} \tag{5}$$

Where:

$$\varepsilon_e = \frac{\varepsilon_r + 1}{2} + \frac{\varepsilon_r - 1}{4}\left(1 + \frac{12h}{a}\right)^{-1/2} \tag{6}$$

Effective length of the patch is equal to.

$$a_e = a + \frac{h}{\sqrt{\varepsilon_r}} \tag{7}$$

3-3-3 Hexagon patch

It is about an antenna of length side (*s*), thickness (*h*) posed on a substrate of permittivity (ε_r). The objective is to find the values of the three parameters: :(*s*, *h*, and ε_r), so that the antenna satisfies the constraint (a resonant frequency equal to 10 GHz)[1].

The resonant frequency of TM_{11} mode of the Hexagon radiant element is:

$$f_{nm} = \frac{1.1K_{nm} * c}{2\pi s\sqrt{\varepsilon_r}} \tag{8}$$

K_{mn} is the m^{th} zero of the derivative of the Bessel function of order n and is equal to 1.84118 for TM_{11} –mode.

3-4- Selection

The selection operator distinguishes the better individuals from the worse individuals using their fitness. It's is an important function in genetic algorithms (GAs), based on an evaluation criterion that returns a measurement of worth for any chromosome in the context of the problem. It is the stage of genetic algorithm in which individual genomes are chosen from the string of chromosomes. The commonly used techniques for selection of chromosomes are Roulette wheel, rank selection and steady state selection [9, 15]. In this approach Roulette Wheel selection is used in which parents are selected according to their fitness and the better chromosomes are the more chances to be selected.

3-5- Crossover

Crossover is another process that involves exchange of genetic materials between two parent chromosomes to make child chromosome. The simplest way how to do this is to choose randomly some crossover point and then everything before this point copies from the first parent and then everything after a crossover point copies from the second parent. There are many types of crossover, single point, two points, uniform and arithmetic crossover. In this paper a single point crossover is used with crossover probability is equal to 85%. One crossover point is selected at random position; the parts of two parents after the crossover position are exchanged to form two offspring [15, 16] as shown in Figure (3).

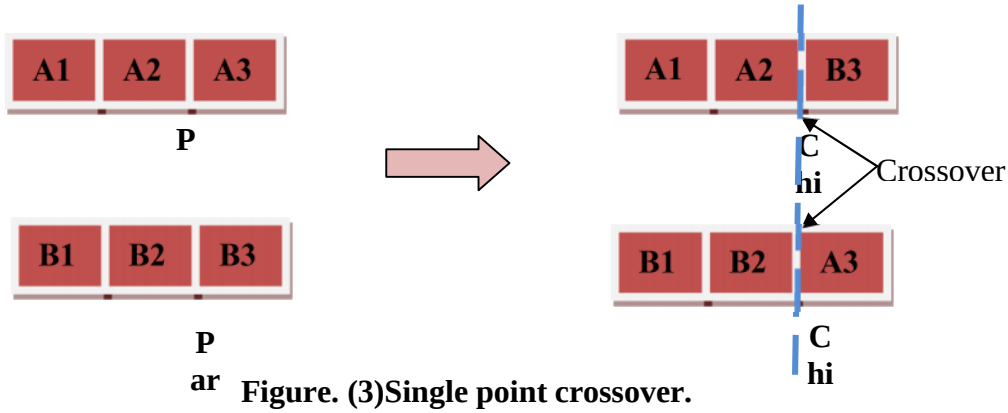

Figure. (3)Single point crossover.

3-6- Mutation

A common view in the GA community is that the crossover is the major instrument of variation and innovation in GA, with mutation insuring the population against permanent fixation at any particular locus and thus playing more of backgrounds role. The appreciation of the role of mutation is growing as the GA community attempts to understand how GA solves complex problems. After a crossover is performed, mutation takes place. This is to parent falling all solutions in population into a local optimum of solved problem. Mutation changes randomly the new offspring (children).There are many types of accomplishing mutation (binary mutation, and real mutation). Real mutation is used according to the following equation, as [15,16]:

$$d_i' = \begin{cases} r(L_o, U_p) & \text{if } z' \le P_m \\ d_i & \text{otherwise} \end{cases} \qquad (9)$$

Where: $\mathbf{z'}$ **:** is random number, $\mathbf{r(L_o,U_p)}$: is random number with limited range (L_o,U_p).

$\mathbf{d_i}$: is the value of gene before mutation. $\mathbf{d_i'}$:is the value of gene after mutation.

$\mathbf{P_m}$: is probability of mutation equal to (0.5%-1%) .

4. Results and discussion

The genetic characteristics are as follows:

*Real value chromosomes, the numbers of chromosomes by population are 100 chromosomes.

* The probability of crossover is 90% and probability of mutation is 1%.

Figure(4) shows the chromosome representation for the three types of microstrip antenna which means the representation of the variables that required to be optimized through the GA, while Figure (5) shows the genetic algorithm for the design of microstrip antenna using MATLAB program. A rectangular, equilateral triangular, and hexagon patches that desiged using genetic algorithm have been constructed and analysis in Microwave Office software 7.1.

Tables (1, 2 and 3) show the design of rectangular ,equilateral triangular and hexagon patches microstrip antenna using GA program and microwave office. The genetic algorithm has been proved to be useful for the design of different types of microstrip antenna (rectangular ,triangular and hexagon patches) that gives good accuracy in compared with MWO as shown in third, fourth, and fifth columns in tables(1,2,and3).

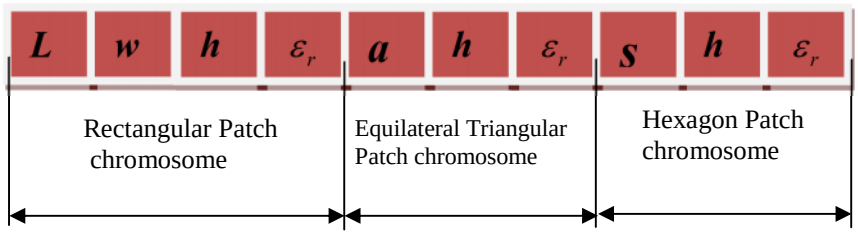

Figure (4). Chromosome representation for microstrip antenna.

Analysis of rectangular

Figure (6) shows the construction of rectangular microstrip antenna using microwave office. Figure (7) shows polar pattern in H-planes and it is found the HPBW in H-plane is equals to 62 degrees. Figure (8) shows the relation between VSWR and frequency. Figure (9) shows the polar pattern in E and it is found the HPBW in E-plane is equal to 61 degrees .

Analysis of triangular

Figure(10) shows the construction of triangular microstrip antenna using microwave office. Figure (11) shows polar pattern in H-planes and it is found the HPBW is equal to 64 degrees. Figure(12) shows the relation between VSWR and frequency. Figure (13) shows polar pattern in E and it is found the HPBW in E-plane is equal to 66 degrees .

Analysis of Hexagon

Figure(14) shows the construction of hexagon microstrip antenna using microwave office. Figure (15) shows polar pattern in H-planes and it is found the HPBW is equal to 67 degrees. Figure (16) shows the relation between VSWR and frequency. Figure (17) shows polar pattern in E-plane and it is found the HPBW is equal to 63 degree. From the above achieved results, using genetic algorithm is practically acceptable and it's successfully implemented for designing the microstrip antenna with different shapes.

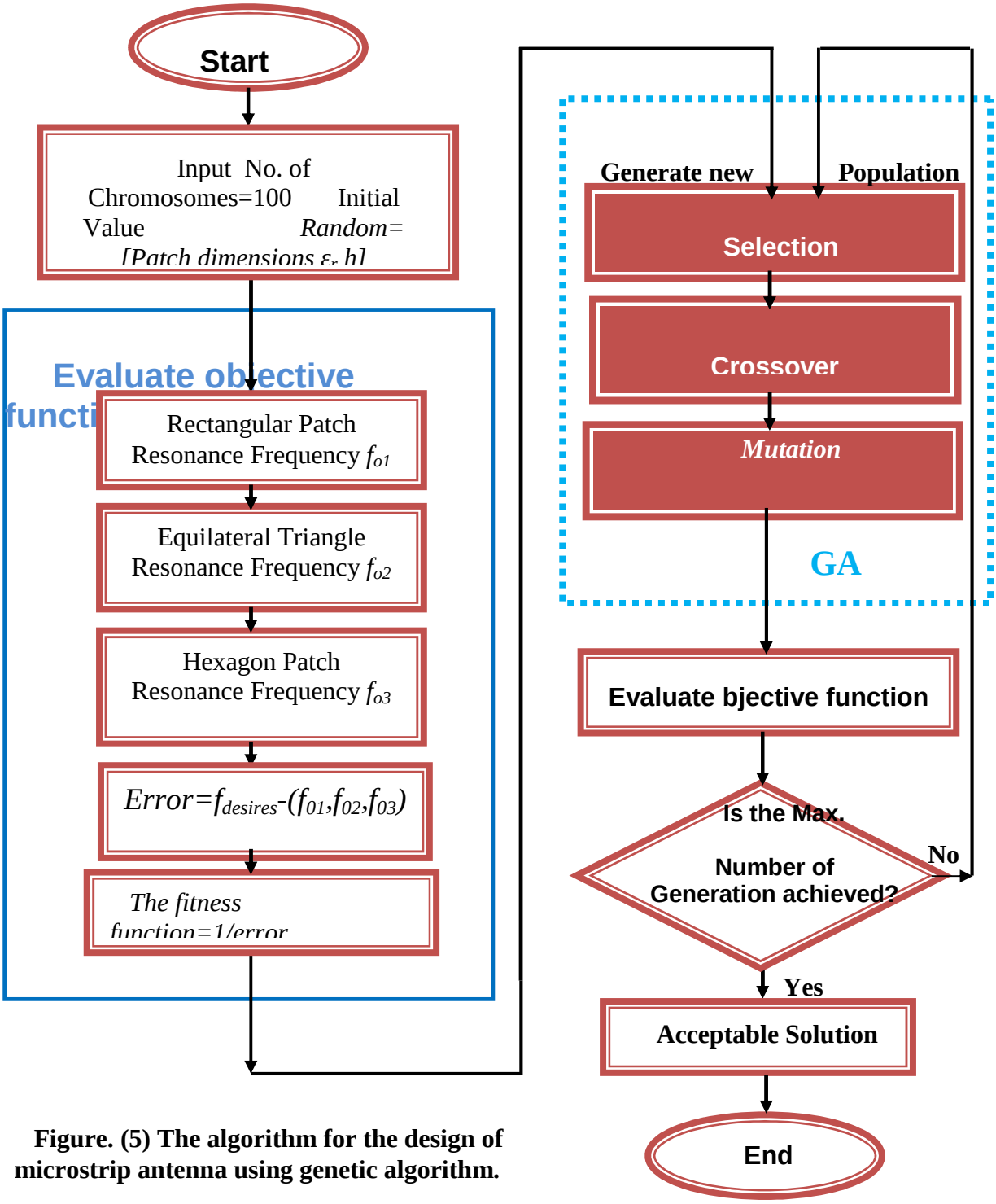

Figure. (5) The algorithm for the design of microstrip antenna using genetic algorithm.

Table (1). Design of rectangular microstrip antenna using GA.

Substrate Material(ε_r)	Height (h) in cm	Width (W) in cm	Length (L) in cm	Center frequency in GHz Using GA	Center frequency in GHz Using MWO	Accuracy%
2.6791	0.316	1.7922	0.6811	10.012	10.1	99.13%
2.7051	0.0957	0.3773	0.9038	10.011	9.9	98.88%
2.6556	0.8104	1.3152	0.3551	10.003	9.19	91.15%
2.4676	0.0605	1.1414	0.9348	9.91	9.94	99.70%
2.6011	0.0943	1.7951	0.8632	10.047	10.1	99.48%
2.3248	0.2763	0.6208	0.8361	9.9495	9.78	98.27%
2.2498	0.0812	0.41	0.9999	9.9033	9.88	99.76%
2.0152	0.2848	1.5129	0.834	9.9591	9.71	97.43%
2.7089	0.2848	0.2517	0.834	9.976	9.8	98.20%
3.0328	0.0782	0.4629	0.8631	9.932	9.88	99.47%
3.0328	0.0782	0.4101	0.8631	9.9836	9.67	96.76%

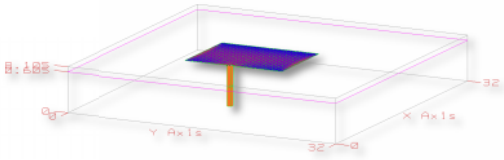

Figure.(6) The construction of rectangular microstrip antenna using microwave office.

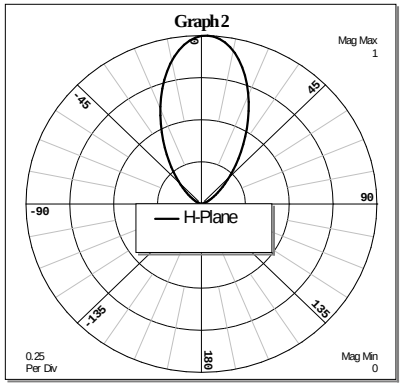

Figure (7). Polar pattern in E-planes of rectangular microstrip antenna using microwave office.

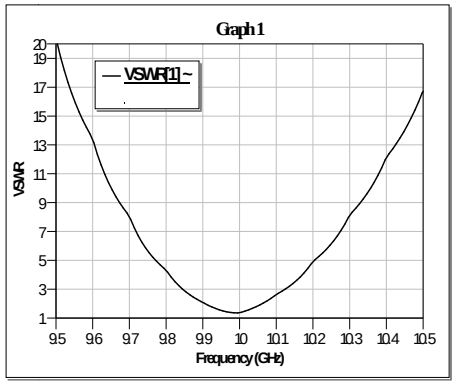

Figure(8). Shows the relation between VSWR and frequency of rectangular microstrip antenna using microwave office.

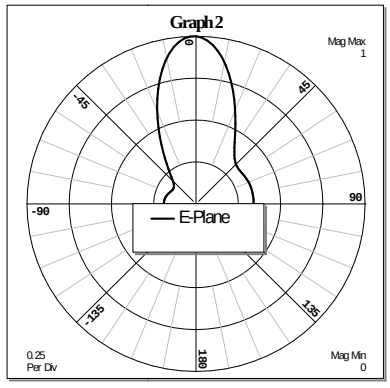

Figure (9).Polar pattern in H-planes of rectangular microstrip antenna using microwave office.

Table (2). Design of equilateral triangular microstrip antenna using GA .

Substrate Material (ε_r)	Height (h.) in cm	Length of Sides (a) in cm	Center frequency in GHz Using GA	Center frequency in GHz MWO	Accuracy%
2.6791	0.306	1.2238	9.903	9.7	97.91%
2.2435	0.1849	1.3423	10.135	9.77	96.26%
2.0886	0.2049	1.3822	10.043	9.81	97.62%
3.5023	0.1624	1.1386	10.062	9.75	96.80%
2.4451	0.0469	1.3665	10.06	9.99	99.30%
3.3242	0.1362	1.1810	9.997	9.81	98.09%
3.0716	0.1156	1.2275	10	10	100.00%
3.4813	0.0661	1.1775	9.998	9.5	94.76%
2.8977	0.3151	1.1694	10.001	9.3	92.46%
2.2433	0.0421	1.4273	9.999	9.98	99.81%
2.2747	0.056	1.4132	10.005	9.9	98.94%

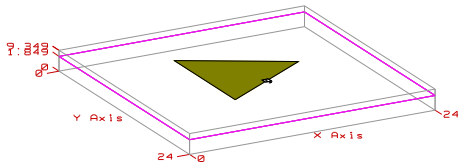

Figure.(10) The construction of triangular microstrip antenna using microwave office.

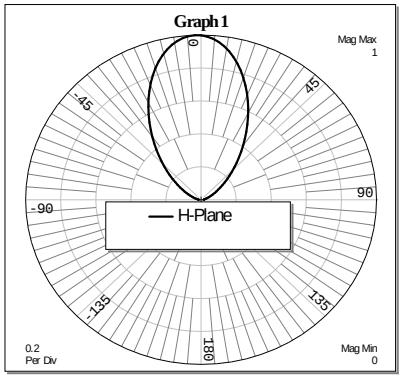

Figure(11).Polar pattern in H - planes of triangular microstrip antenna using microwave office.

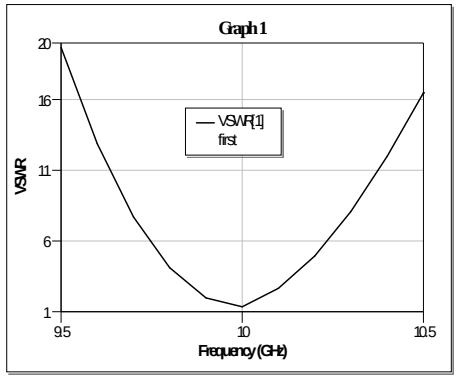

Figure (12). Shows the relation between VSWR and frequency of triangular microstrip antenna using microwave office.

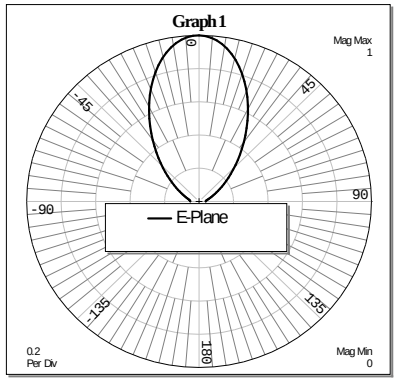

Figure(13). Polar pattern in E - planes of triangular microstrip antenna using microwave office.

Table (3). Design of hexagon microstrip antenna using GA .

Substrate Martial(ε_r)	Height (h.) in cm	Length of Sides (s) in cm	Center frequency Using GA	Center frequency Using MWO	Accuracy%
2.1788	0.294	0.6746	10.021	9.8	97.74%
2.4181	0.425	0.6384	10.052	10.1	99.52%
2.8642	0.5746	0.5845	10.088	9.87	97.79%
2.1214	0.0443	0.6836	10.023	10.2	98.26%
2.6669	0.1584	0.6105	10.01	9.94	99.30%
2.6224	0.0466	0.6154	10.013	10.13	98.85%
2.6082	0.2747	0.6137	10.069	10	99.31%
2.473	0.0458	0.6292	10.086	9.988	99.02%
2.5656	0.0475	0.62	10.048	10.11	99.39%
2.2016	0.5698	0.6709	10.024	9.89	98.65%

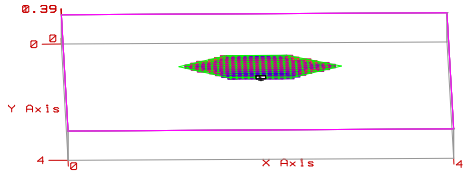

Figure(14). The Construction of Hexagon Microstrip Antenna Using Microwave Office.

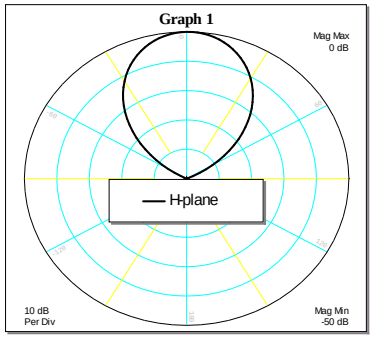

Figure(15). Polar pattern in H -planes of triangular microstrip antenna using microwave office.

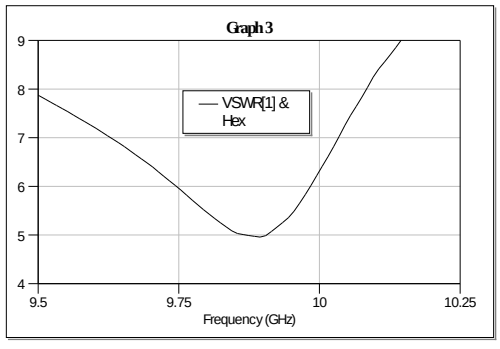

Figure(16).Shows the relation between VSWR and frequency of hexagon microstrip antenna using microwave office.

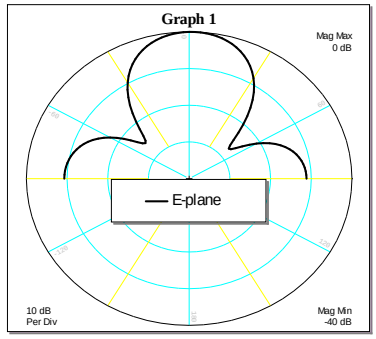

Figure (17) Polar pattern in E -planes of triangular microstrip antenna using microwave office.

5. Conclusions

1- The genetic algorithm has been proved to be useful for the design of different types of microstrip antenna. A simple and flexible genetic algorithm GA is proposed as a general tool for design of microstrip antenna in various forms such as rectangular, equilateral triangle and hexagon patch antennas. The design procedure is to determine the resonance frequency in terms of patch dimensions, dielectric constant (ε_r) and thickness h.

2- The output of the GA (the resonance frequency , patch dimensions ,dielectric constant (ε_r), and thickness h) is examined against the simulation which done in MWO 2007 software.

6. References

[1] Bahil I.J., and Bhartia P., "Microstrip Antennas", Artech House,1980.

[2] Balanis C.A. ,"Moderen Antenna Handbook",John Wiley and sons, tenth edition, 2008.

[3] N. Chattoraj, Jibendu Sekhar Roy," Application of Genetic Algorithm to the Optimization of Microstrip Antennas with and without Superstrate". Microwave Review.V12,(2006),No2.

[4] N. Chattoraj and Jibendu Sekhar Roy," Application of Genetic Algorithm to the Optimization of Gain of Magnetized Ferrite Microstrip Antenna". Engineering Letters. V14, (2007), EL_14_2_15.

[5] Y. Cengiz and H. Tokat ," Linear Antenna Array Design with Use of Genetic , Memetic and TABU Serach Optimization Algorithm" Progress In Electromagnetic Research C, Vol. 1, (2008).pp: 63–72.

[6] Si-Yang Sun, Ying-Hua Lu," Design of Broadband Microstrip Antenna Utilizing Genetic Algorithm", IEICE,(2009).

[7] X. Yongsheng, J. Zhou, Shujing Li, and L. Huang, " Optimization of line-tapered MMI devices uses a genetic algorithm". Chinese Optical Letters . Vol.7,(2009), No.11.

[8] A. Reza D., Gholamreza D. and Mohammad Hossein S. ," New Design Method of UWB Microstrip Filters Using Adaptive Genetic Algorithms with Defected Ground Structures". International Journal of Microwave Science and Technology. Vol.2010, (2010),671515.

[9] R. Malhotra, Narinder S. and Yaduvir S.," Genetic Algorithms: Concepts, Design for Optimization of Process Controllers", Computer and Information Science, Vol. 4, March (2011), No.2.

[10] S. Mehrjoo, Hassan A. and Hossein K.," A Novel Hybrid GA-ABC based Energy Efficient Clustering in Wireless Sensor Network". Canadian Journal on Multimedia and Wireless Networks Vol. 2, April (2011), No.2.

[11] I. Abiodun M., L. Olawale N. and A. Adebowale P." The Effectiveness of Genetic Algorithm in Solving Simultaneous Equations". International Journal of Computer Applications (0975 – 8887), Vol.14, February (2011), No.8.

[12] Y. Wang, Shangce G., Hang Yu and Zheng T.," Synthesis of Antenna Array by Complex-valued Genetic Algorithm". IJCSNS International Journal of Computer Science and Network Security, Vol.1, January (2011), No.1.

[13] A. Correa, Andrés G., and Camilo L.," Genetic Algorithm Optimization for Selecting the Best Architecture of a Multi-Layer Perceptron Neural Network: A Credit Scoring Case", SAS Global Forum, Data Mining and Text Analytics, (2011).

[14] J. Jin, H. L. Wang, W. M. Zhu, and Y. Z. Liu ," Array Patterns Synthesizing Using Genetic Algorithm" Progress In Electromagnetic Research Symposium, Cambridge, USA, March 26-29, (2006).

[15] K. Keng Yan, and Yilong ,"Side Lobe Reduction in Array Pattern Synthesis Using Genetic Algorithms ،" IEEE, Antenna and propagation, Vol.45, July(1997).No.7. pp:1117

[16] M. Obitko, "Introduction to Genetic Algorithms", Hochschule for Technik and Wirtschaft Dresden, September (1998).

System Response Analysis of Linear Time Invariant Multistage Feedback Amplifier Network

Muneer Aboud Hashem

Electrical Engineering Department

College of Engineering

Al.Mustansiriya University

Abstract

The analysis of voltage series multistage feedback amplifier network is achieved by evaluating the nodal admittance matrix of the equivalent circuit representing the replacing of each transistor in a stage by its high frequency small-signal model and the performing of the high order voltage transfer function of the system. The main reasons of treating such a wide-band amplifier network are of its stabilized voltage gain and its ability to amplify the pulses occurring in a television signal. The frequency response of the system is calculated and confirmed. System dynamics and variation of input signal are obtained by calculating the response of a continuous time system. The discrete-time equivalent to the analogue system allows the system designer to choose an appropriate pulse transfer function to investigate the performance of the system suitable for a given specifications and requirements. The software powerful MAT-LAB version 7.2 techniques is used for treating the single expression transfer function obtained by assigning numerical values and the response of the system in time and frequency domain.

تحليل استجابةِ نظامِ شبكةِ مضخّمِ تعليقاتِ الوقتِ الخطيِّ المتعددة المراحلِ الثابتة

المستخلص

يتناول البحث تحليل شبكة مضخم التغذية العكسية متعدد المراحل عن طريق حساب مصفوفة الدخل العقدية للدائرة المكافئة للمضخم المتمثلة بتبديل كل ترانزستور في المرحلة التي تمثله بنموذج التذبذب العالي صغير الإشارة وانجاز وظيفة نقل فولتية الطلب العالية للنظام.والسبب الرئيسي لمعالجة شبكة المضخم ذات النطاق الترددي العريض هو فولتية الكسب المستقرة لهذا المضخم وقابليته على تكبير النبضات التي تظهر في الإشارات التلفازية.أن الاستجابة الترددية للنظام ثم حسابها وتأكيدها وقد أمكن الحصول على ديناميكية النظام وتغيرات إشارة الإدخال وبحساب استجابة النظام للوقت المستمر.أن الوقت المفصل للنظام المكافئ للنظام التماثلي يسمح لمصمم النظام باختيار وظيفة نقل نبضي لبحث أداء النظام للتلاؤم مع أي مواصفات أو متطلبات معينة. وقد تم استخدام تقنية البرامج الفعالة MAT-LAB النسخة7.2 لوظيفة النقل الأحادية المقطع المستحلة عن طريق تخصيص قيم عددية لاستجابة النظام في مديات الزمن و التردد.

1. Introduction

In a network design problems, numerical values are assigned to network elements and the simulation process resulted in a single expression transfer function to give the designer an ability to study the effect of network parameters on the network function in addition to the repeated usage of the information used.

The analysis of complex systems or networks can be facilitated through some insight into the internal structure of the elements constituting the system.

The wide-band voltage amplifier considered in the analysis of a multistage feedback amplifier network has an improved bandwidth through the usage of an additional stage and a flat response for minimum distortion in the signal. The negative feedback used in this network stabilizes the closed-loop gain of the amplifier at a lower and predictable gain level [1]. The voltage-series multistage feedback amplifier [2], depicted in Figure 1, is used in the analysis. The treatment of the network is based on the investigation of the behavior of the network under fixed parameters values. The advantages of treating such a network lie in the ability of controlling the gain by introducing a feedback through resistor combinations and the use of the feedback makes the system response insensitive to external disturbances and internal variation in the system parameters. The analysis is considered in the high frequency region and the flat response of the low pass filter network is obtained.

The descriptive and procedural side with the aid of additional facilities for examining the network gives a general and accurate circuit suitable for extension, modification and modular organization to the designer for future developments.

Complicated and tedious features of the network can be minimized by replacing each transistor in a single amplifier stage by its small-signal hybrid-π model valid in any topology as indicated in Figure (2), where the resistor R is

$$R = R_{c1} \| R_5 \| R_6$$

The nodal admittance matrix that describes the network is given by

$$\left[\frac{1}{r_{bb'}} + \frac{1}{r_{be'}} + s(C_e + C_c)\right]V_1 - \left(\frac{1}{r_{be'}} + sC_e\right)V_3 - sC_cV_2 = V_s / r_{bb'} \qquad (1)$$

$$\left(\frac{1}{r_{bb'}} + \frac{1}{R} + sC_c\right)V_2 - sC_cV_1 - \frac{1}{r_{bb'}}V_4 = -g_m(V_1 - V_3) \qquad (2)$$

$$\left(\frac{1}{r_{be'}}+\frac{1}{R_1}+\frac{1}{R_2}+sC_e\right)V_3-\left(\frac{1}{r_{be'}}+sC_e\right)V_1-\frac{1}{R_2}V_o=g_m\left(V_1-V_3\right) \qquad (3)$$

$$\left[\frac{1}{r_{bb'}}+\frac{1}{r_{be'}}+s\left(C_e+C_c\right)\right]V_4-\frac{1}{r_{bb'}}V_2-sC_cV_o=0 \qquad (4)$$

$$\left(\frac{1}{R_{c2}}+\frac{1}{R_2}+sC_c\right)V_o-\frac{1}{R_2}V_3-sC_cV_4=-g_mV_4 \qquad (5)$$

To characterize the input-output relationships of the LTI (linear time invariant) system described by the nodal admittance matrix above the transfer function can be found as

$$\frac{V_o}{V_s}=\frac{N}{D}=\frac{\begin{vmatrix} \frac{1}{r_{bb'}}+\frac{1}{r_{be'}}+s\left(C_e+C_c\right) & -sC_c & -\frac{1}{r_{be'}}-sC_e & 0 & \frac{1}{r_{bb'}} \\ g_m-sC_c & \frac{1}{r_{bb'}}+\frac{1}{R}+sC_c & -g_m & -\frac{1}{r_{bb'}} & 0 \\ -g_m-\frac{1}{r_{be'}}-sC_e & 0 & g_m+\frac{1}{r_{be'}}+\frac{1}{R_1}+\frac{1}{R_2}+sC_e & 0 & 0 \\ 0 & -\frac{1}{r_{bb'}} & 0 & \frac{1}{r_{bb'}}+\frac{1}{r_{be'}}+s\left(C_e+C_c\right) & 0 \\ 0 & 0 & -\frac{1}{R_2} & g_m-sC_c & 0 \end{vmatrix}}{\begin{vmatrix} \frac{1}{r_{bb'}}+\frac{1}{r_{be'}}+s\left(C_e+C_c\right) & -sC_c & -\frac{1}{r_{be'}}-sC_e & 0 & 0 \\ g_m-sC_c & \frac{1}{r_{bb'}}+\frac{1}{R}+sC_c & -g_m & -\frac{1}{r_{bb'}} & 0 \\ -g_m-\frac{1}{r_{be'}}-sC_e & 0 & g_m+\frac{1}{r_{be'}}+\frac{1}{R_1}+\frac{1}{R_2}+sC_e & 0 & -\frac{1}{R_2} \\ 0 & -\frac{1}{r_{be'}} & 0 & \frac{1}{r_{bb'}}+\frac{1}{r_{be'}}+s\left(C_e+C_c\right) & -sC_c \\ 0 & 0 & -\frac{1}{R_2} & g_m-sC_c & -\frac{1}{R_{c1}}+\frac{1}{R_2}sC_c \end{vmatrix}}$$

where (6)

$$N = (1/r_{bb'})[(-1/r_{bb'})(g_m - sC_c)\{(-g_m)(-g_m - 1/r_{b'e} - sC_e) - (g_m - sC_c)(g_m + 1/r_{b'e} + 1/R_1 + 1/R_2 + sC_e\} + (-g_m - 1/r_{b'e} - sC_e)(-1/R_2)\{(1/r_{bb'} + 1/R + sC_c)(1/r_{bb'} + 1/r_{b'e} + s(C_e + C_c)) - (-1/r_{bb'})(-1/r_{bb'})\}] \quad (7)$$

and

$$D = (1/r_{bb'} + 1/r_{b'e} + s(C_e + C_c))[(1/r_{bb'} + 1/R + sC_c)(g_m + 1/r_{b'e} + 1/R_1 + 1/R_2 + sC_e)(1/r_{bb'} + 1/r_{b'e} + s(C_e + C_c))(1/R_{c1} + 1/R_2 + sC_c) - (-sC_c)(g_m - sC_c)\} + (-1/R_2)(-1/R_2)\{(-1/r_{bb'})(-1/r_{bb'}) - (1/r_{bb'} + 1/R + sC_c)(1/r_{bb'} + 1/r_{b'e} + s(C_e + C_c)\} - (-1/r_{bb'})\{(-g_m)(-1/R_2)(g_m - sC_c) + (-1/r_{bb'})(g_m + 1/r_{b'e} + 1/R_1 + 1/R_2 + sC_e)(1/R_{c1} + 1/R_2 + sC_c)\}] + (-sC_c)[(g_m - sC_c)(g_m + 1/r_{b'e} + 1/R_1 + 1/R_2 + sC_e)\{(-sC_c)(g_m - sC_c) - ((1/r_{bb'} + 1/r_{b'e} + s(C_e + C_c))(1/R_{c1} + 1/R_2 + sC_c)\} + (-g_m)(-g_m - 1/r_{b'e} - sC_e)\{((1/r_{bb'} + 1/r_{b'e} + s(C_e + C_c))(1/R_{c1} + 1/R_2 + sC_c) - (-sC_c)(g_m - sC_c)\} + (-1/R_2)\{(g_m - sC_c)(-1/R_2)(1/r_{bb'} + 1/r_{b'e} + s(C_e + C_c)) + (-1/r_{bb'})(-g_m - 1/r_{b'e} - sC_e)(-sC_c)\}] + (-1/r_{b'e} - sC_e)[(1/r_{bb'} + 1/R + sC_c)(-g_m - 1/r_{b'e} - sC_e)\{(-sC_c)(g_m - sC_c) - (1/r_{bb'} + 1/r_{b'e} + s(C_e + C_c))(1/R_{c1} + 1/R_2 + sC_c)\} + (-1/r_{bb'})\{(g_m - sC_c)(-1/R_2)(g_m - sC_c) + (-1/r_{bb'})(-g_m - 1/r_{b'e} - sC_e)(1/R_{c1} + 1/R_2 + sC_c)\}] \quad (8)$$

For hybrid-π parameters value, the magnitudes used for the elements of the hybrid-π model at room temperature are;

$g_m = 50\,\text{mA/V}$, $r_{bb'} = 100\,\Omega$, $r_{b'e} = 1\,\text{K}\Omega$, $C_e = 4\,\text{pF}$, $C_c = 98\,\text{pF}$

where g_m is the transistor transconductance, $r_{bb'}$ is the ohmic base spreading resistance, $r_{b'e}$ is the input resistance, C_e is the sum of the emitter diffusion capacitance and the emitter junction capacitance, and C_c is the collector junction capacitance. The magnitudes for the other elements of the network are;

$R_1 = 140\,\text{K}\Omega$, $R_2 = 50\,\text{K}\Omega$, $R_{c1} = 12\,\text{K}\Omega$, $R_{e1} = 5\,\text{K}\Omega$, $R_3 = 49\,\text{K}\Omega$, $R_4 = 32\,\text{K}\Omega$, $R_{c2} = 4.5\,\text{K}\Omega$, $R_{e2} = 5\,\text{K}\Omega$, $R_1 = 125\,\Omega$, $R_2 = 5.2\,\text{K}\Omega$, $C_1 = 6\,\mu\text{F}$, $C_2 = 6\,\mu\text{F}$, $C_3 = 10\,\mu\text{F}$, $C_4 = 48\,\mu\text{F}$, $C_5 = 48\,\mu\text{F}$, $C_6 = 6\,\mu\text{F}$.

2. Transfer function analysis

According to the above magnitudes, the transfer function $TF_{A(s)}$ of the continuous-time multistage feedback amplifier network is given by

$$TF_A(s) = 5.3686\times10^7 \frac{\left(s-7.4716\times10^9\right)\left(s+1.3852\times10^9\right)\left(s-0.8553\times10^9\right)}{\left(s+1.9874\times10^9\right)\left(s+0.6597\times10^9\right)\left(s+0.2101\times10^9\right)\left(s+0.0425\times10^9\right)} \quad (9)$$

where s is a complex variable.

The partial fraction expansion [3] of $TF_{A(s)}$ has the form

$$TF_A(s) = \frac{0.1894\times10^9}{s+1.9874\times10^9} + \frac{1.3023\times10^9}{s+0.6597\times10^9} - \frac{3.8542\times10^9}{s+0.2101\times10^9} + \frac{2.4162\times10^9}{s+0.0425\times10^9} \quad (10)$$

Clearly, the amplifier has three zeros

$z_1 = 7.4716\times10^9$ $z_2 = -1.3852\times10^9$ $z_3 = 0.8553\times10^9$

and four poles

$p_1 = -1.9874\times10^9$ $p_2 = -0.6597\times10^9$

$p_3 = -0.2101\times10^9$ $p_4 = -0.0425\times10^9$

The zeros and poles lie in the high frequency band. The frequency response characteristics of the amplifier are obtained by the Bode plot. The adjusting of these characteristics by using several design criteria gives acceptable transient-response characteristics [4], the high frequency response can also be improved by using current amplifier [5]. Substituting $s = j\omega$ in Eq. 9 gives

$$TF_A(j\omega) = \frac{40.5937\left(1-j\frac{\omega}{7.4716\times10^9}\right)\left(1+j\frac{\omega}{1.3852\times10^9}\right)\left(1-j\frac{\omega}{0.8553\times10^9}\right)}{\left(1+j\frac{\omega}{1.9874\times10^9}\right)\left(1+j\frac{\omega}{0.6597\times10^9}\right)\left(1+j\frac{\omega}{0.2101\times10^9}\right)\left(1+j\frac{\omega}{0.0425\times10^9}\right)} \quad (11)$$

where ω is the angular frequency. With the aid of MATLAB numeric computation software [6], the Bode magnitude and phase plot are depicted in Figs. 3 and 4. It can be seen that the

peak gain is $32.2\,\text{dB}$ at $\omega = 0.0848\times10^{6}$ rad/sec $(f = 13.5\,\text{KHz})$, where f is the frequency. The $-3\,\text{dB}(28.84\,\text{or}\,29.2\,\text{dB})$ occurs at $\omega = 4.05\times10^{7}$ rad/sec $(f = 6.455\,\text{MHz})$.

3. Confirmation

A calculations can be made to confirm the value of the peak gain obtained from the Bode plot with that evaluated above in the following procedure;

1- Evaluation of the output resistances and the voltage gain of each transistor.
2- Obtaining the voltage gain of the amplifier without feedback.
3- Determination of the feedback network.
4- Calculation of the voltage gain of the amplifier with feedback.

According to the stated procedure,

$$R_{L1} = R_{c1}\|R_3\|R_4\|h_{ie2} = 12\,\text{K}\Omega\|49\,\text{K}\Omega\|32\,\text{K}\Omega\|1.1\,\text{K}\Omega = 957\,\Omega$$

$$R_{L2} = R_{c2}\|(R_1 + R_2) = 4.5\,\text{K}\Omega\|(125\,\Omega + 5.2\,\text{K}\Omega) = 2.438\,\text{K}\Omega$$

where R_{L1}, R_{L2}, h_{ie2} are the output resistance of Q_1, the output resistance of Q_2, the input resistance with output short-circuited hybrid parameter of Q_2, respectively. The values of the voltage gain of Q_1 and Q_2 are A_{v1} and A_{v2} are given by, (neglecting the reverse –open-circuit voltage amplification hybrid parameter h_{re} and the output conductance with input open-circuited hybrid parameter h_{oe}), so

$$A_{v1} = \frac{-h_{fe1}R_{L1}}{h_{ie1} + (1 + h_{fe1})(R_1\|R_2)} = \frac{-50(957\,\Omega)}{1.1\,\text{K}\Omega + (51)(125\,\Omega\|5.2\,\text{K}\Omega)} = -6.427$$

$$A_{v2} = \frac{-h_{fe2}R_{L2}}{h_{ie2}} = \frac{-50(2.438\,\text{K}\Omega)}{1.1\,\text{K}\Omega} = -110.81$$

$$A_{vt} = A_{v1}\times A_{v2} = -6.427\times-110.81 = 712.17$$

where h_{fe1} and h_{fe2} are the short-circuit current gain hybrid parameters of Q_1 and Q_2, respectively, h_{ie1} is the input resistance hybrid parameter of Q_1, and A_{vt} is the voltage gain of the amplifier without feedback. The value of the feedback network, β, is given by

$$\beta = R_1/(R_1 + R_2) = 125\,\Omega/(125\,\Omega + 5.2\,\text{K}\Omega) = 0.0234$$

The voltage gain of the amplifier with feedback is

$$A_{vf} = \frac{A_{vt}}{1+\beta A_{vt}} = \frac{712.17}{1+(0.0234)(712.17)} = 40.326 = 32.11\,\text{dB}$$

since $|A_{vf}| < |A_{vt}|$ the feedback is negative. The gain can also be confirmed from Eq. 9 as

$$\frac{5.3638\times10^{7} z_1 z_2 z_3}{p_1 p_2 p_3 p_4} = \frac{5.3638\times10^{7} \times 7.4716\times10^{9} \times 1.3852\times10^{9} \times 0.8553\times10^{9}}{1.9874\times10^{9} \times 0.6597\times10^{9} \times 0.2101\times10^{9} \times 0.0425\times10^{9}}$$

$$= 40.59 = 32.16\,\text{dB}.$$

4. Continuous time responses

Complete information about dynamic characteristics of the system can be obtained by exciting it with an impulse input and measuring the output. The transfer function stated previously; however, contain same information about system dynamics as the response of a linear system to a unit-impulse input when the initial conditions are zero. The unit-impulse response is obtained by taking the inverse Laplace transform to Eq. 10.

$$h_A(t) = 0.1894\times10^{9} \exp\left(-1.9874\times10^{9} t\right) + 1.3023\times10^{9} \exp\left(-0.6597\times10^{9} t\right) - 3.8542\times10^{9} \exp\left(-0.2101\times10^{9} t\right) + 2.4162\times10^{9} \exp\left(-0.0425\times10^{9} t\right) \quad (12)$$

where $h_A(t)$ is a function of time t.

The amplifier at high frequencies responds to rapid variations in signals, the step input is of the most available sudden function applied to the amplifier. The input-output relationship of the amplifier $TF_{st-A}(s)$ subjected to a step input is given by

$$TF_{st-A}(s) = \frac{1}{s}\left(\frac{0.1894\times10^{9}}{s+1.9874\times10^{9}} + \frac{1.3023\times10^{9}}{s+0.6597\times10^{9}} - \frac{3.8542\times10^{9}}{s+0.2101\times10^{9}} + \frac{2.4162\times10^{9}}{s+0.0425\times10^{9}}\right) \quad (13)$$

$$= \frac{0.0953}{s} - \frac{0.0953}{s+1.9874\times10^{9}} + \frac{1.974}{s} - \frac{1.974}{s+0.6597\times10^{9}} - \frac{18.3445}{s} + \frac{18.3445}{s+0.2101\times10^{9}} + \frac{56.8517}{s} - \frac{56.8517}{s+0.0425\times10^{9}} \quad (14)$$

Taking the inverse Laplace transform yields the unit step response of the system given by

$$h_{st-A}(t) = 0.0953\left[1-\exp\left(-1.9874\times10^{9}t\right)\right] + 1.974\left[1-\exp\left(-0.6597\times10^{9}t\right)\right] - 18.3445\left[1-\exp\left(-0.2101\times10^{9}t\right)\right] + 56.8517\left[1-\exp\left(-0.0425\times10^{9}t\right)\right] \quad (15)$$

For gradual changing function, the unit ramp function is a good test signal. The input-output relationship of the amplifier $TF_{ra-A}(s)$ subjected to a unit ramp input is given by

$$TF_{ra-A}(s) = \frac{1}{s^{2}}\left(\frac{0.1894\times10^{9}}{s+1.9874\times10^{9}} + \frac{1.3023\times10^{9}}{s+0.6597\times10^{9}} - \frac{3.8542\times10^{9}}{s+0.2101\times10^{9}} + \frac{2.4162\times10^{9}}{s+0.0425\times10^{9}}\right) \quad (16)$$

$$= -\frac{0.0479\times10^{9}}{s} + \frac{0.0953}{s^{2}} - \frac{0.0479\times10^{9}}{s+1.9874\times10^{9}} + \frac{2.9923\times10^{9}}{s} + \frac{1.974}{s^{2}} - \frac{2.9923\times10^{9}}{s+0.6597\times10^{9}} + \frac{87.3136\times10^{9}}{s} - \frac{18.3445}{s^{2}} - \frac{87.3136\times10^{9}}{s+0.2101\times10^{9}} - \frac{1337.6885\times10^{9}}{s} + \frac{56.8517}{s^{2}} - \frac{1337.6885\times10^{7}}{s+0.0425\times10^{9}} \quad (17)$$

Taking the inverse Laplace transform yields the unit ramp response of the system as a function of time given by

$$h_{ra-A}(t) = 0.0953t - 0.0479\times10^{9}\left[1-\exp\left(-1.9874\times10^{9}t\right)\right] + 1.974t - 2.9923\times10^{9}\left[1-\exp\left(-0.6597\times10^{9}t\right)\right] - 18.3445t + 87.3136\times10^{9}\left[1-\exp\left(-0.2101\times10^{9}t\right)\right] + 56.8517t - 1337.6885\times10^{9}\left[1-\exp\left(-0.0425\times10^{9}t\right)\right] \quad (18)$$

The unit impulse, step and ramp responses of the multistage feedback amplifier are depicted in Figs. 5, 6 and 7, respectively. The type of transient response is determined by the closed-loop poles, while the shape of the transient response is primarily described by the closed-loop zeros. The poles of the high order transfer function of the multistage feedback amplifier does not possess complex-conjugate values so the system is non oscillatory. It can be seen also from Figs. 5 and 6 that the system is stable since the magnitudes of the poles lie in the left-half s-plane [7] and the response will die out because the exponential terms in Eqs. 12 and 15 will approaches zero as time increases.

5. Discrete-time system

To simulate the continuous-time amplifier, the impulse invariant method is used [8]. So the design of the discrete-time amplifier from the continuous-time amplifier is as follows; the z-transform of the unit sample response system, $TF_D(z)$ is given by

$$TF_D(z)=\frac{0.1894\times10^9}{1-e^{-1.9874\times10^9 T_S}z^{-1}}+\frac{1.3023\times10^9}{1-e^{-0.6597\times10^9 T_S}z^{-1}}-\frac{3.8542\times10^9}{1-e^{-0.2101\times10^9 T_S}z^{-1}}+\frac{2.4162\times10^9}{1-e^{-0.0425\times10^9 T_S}z^{-1}} \quad (19)$$

where $z=e^{sT_S}$ is a complex variable, T_S is the sampling period and $n=0,1,2....$ is an integer. Clearly the discrete-time system described by Eq. 19 is stable [9] and $TF_D(z)$ approximates the system performance. The unit sample response of the analogue amplifier has a unit sample response equivalent to the unit sample response $h_D(n)$ obtained from Eq. 21 as

$$h_D(n)=0.1894\times10^9\exp\left(-1.9874\times10^9 T_S\right)^n+1.3023\times10^9\exp\left(-0.6597\times10^9 T_S\right)^n-3.8542\times10^9\exp\left(-0.2101\times10^9 T_S\right)^n+2.4162\times10^9\exp\left(-0.0425\times10^9 T_S\right)^n \quad (20)$$

The unit sample response system [10] for $T_S=2$ nS and the parallel realization of Eq. 19 are shown in Figs. 8 and 9. It is interesting to compare the magnitude response of two amplifiers, for the analogue amplifier the magnitude response, $M_A(\omega)$ is

$$M_A(\omega)=\frac{0.1894\times10^9}{\sqrt{\omega^2+\left(1.9874\times10^9\right)^2}}+\frac{1.3023\times10^9}{\sqrt{\omega^2+\left(0.6597\times10^9\right)^2}}-\frac{3.8542\times10^9}{\sqrt{\omega^2+\left(0.2101\times10^9\right)^2}}+\frac{2.4162\times10^9}{\sqrt{\omega^2+\left(0.0425\times10^9\right)^2}} \quad (21)$$

and for the discrete-time amplifier, the magnitude response $M_D(\omega)$ is

$$M_D(\omega)=\frac{0.1894\times10^9}{\sqrt{1-2e^{-1.9874\times10^9T_S}\cos(\omega T_S)+\left(e^{-1.9874\times10^9T_S}\right)^2}}+\frac{1.3023\times10^9}{\sqrt{1-2e^{-0.6597\times10^9T_S}\cos(\omega T_S)+\left(e^{-0.6597\times10^9T_S}\right)^2}}$$

$$-\frac{3.8542\times10^9}{\sqrt{1-2e^{-0.2101\times10^9T_S}\cos(\omega T_S)+\left(e^{-0.2101\times10^9T_S}\right)^2}}+\frac{2.4162\times10^9}{\sqrt{1-2e^{-0.0425\times10^9T_S}\cos(\omega T_S)+\left(e^{-0.0425\times10^9T_S}\right)^2}} \quad (22)$$

The magnitude responses of the two amplifiers are depicted in Figs. 10 and 11. Due to the sampling operation, the amplitude response of the discrete-time system is scales by $1/T_S$. Therefore, a multiplication of $TF_D(z)$ by $1/T_S$ is required to approximate the amplitude response of the discrete-time system to the amplitude response of the analog system [11]. Thus the unit sample response, $TF_{iD}(z)$, of the impulse invariant discrete-time system equivalent to $h_A(t)$ is given by

$$TF_{iD}(z)=\frac{0.1894\times10^{9}T_S}{1-e^{-1.9874\times10^{9}T_S}z^{-1}}+\frac{1.3023\times10^{9}T_S}{1-e^{-0.6597\times10^{9}T_S}z^{-1}}-\frac{3.8542\times10^{9}T_S}{1-e^{-0.2101\times10^{9}T_S}z^{-1}}+\frac{2.4162\times10^{9}T_S}{1-e^{-0.0425\times10^{9}T_S}z^{-1}} \quad (23)$$

The dc response for the analogue system is

$$TF_A(0)=\frac{0.1894\times10^{9}}{1.9874\times10^{9}}+\frac{1.3023\times10^{9}}{0.6597\times10^{9}}-\frac{3.8542\times10^{9}}{0.2101\times10^{9}}+\frac{2.4162\times10^{9}}{0.0425\times10^{9}}$$
$$=40.576=32.6155\,\text{dB}$$

For the discrete-time amplifier, since for any variable x , if the sampling frequency is high, T_S is small, and

$$\exp(-xT_S)=1-(-xT_S)=1+xT_S$$

with this approximation,

$$TF_D(0)=TF_A(0)$$

with good agreement. The input $X(z)$ and the output $Y(z)$ relationship of the discrete-time amplifier is given by

$$TF_D(z)=\frac{Y(z)}{X(z)}=\frac{5.37\times10^{7}-6.088\times10^{7}z^{-1}+4.5246\times10^{8}z^{-2}-4.5502\times10^{7}z^{-3}}{1-1.8615z^{-1}+1.0591z^{-2}-0.1805z^{-3}+0.003z^{-4}} \quad (24)$$

and the corresponding difference equation is

$$y[n]-1.8615y[n-1]+1.0592y[n-2]-0.1805y[n-3]+0.003y[n-4]=5.37\times10^{7}x[n]$$
$$-6.088\times10^{7}\,x[n-1]+4.5246\times10^{8}x[n-2]-4.5502\times10^{7}x[n-3] \quad (25)$$

Taking the Fourier transform of this equation gives

$$TF_D(j\omega)=\frac{Y(j\omega)}{X(j\omega)}$$
$$=\frac{5.37\times10^7-6.088\times10^7(j\omega)^{-1}+4.5246\times10^8(j\omega)^{-2}-4.5502\times10^7(j\omega)^{-3}}{1-1.8615(j\omega)^{-1}+1.0591(j\omega)^{-2}-0.1805(j\omega)^{-3}+0.003(j\omega)^{-4}} \quad (26)$$

The phase response of the discrete-time system can be determined as

$$=\tan^{-1}\angle[5.37\times10^7\sin(4\omega)-6.088\times10^7\sin(3\omega)+4.5246\times10^8\sin(2\omega)-3.5502\times10^7\sin(\omega)]/[5.37\times10^7\cos(4\omega)-6.088\times10^7\cos(3\omega)+4.5246\times10^8\cos(2\omega)-3.5502\times10^7\cos(\omega)]-\tan^{-1}\angle[\sin(4\omega)-1.8615\sin(3\omega)+1.0591\sin(2\omega)-0.1805\sin(\omega)]/[\cos(4\omega)-1.8615\cos(2\omega)+1.0591\cos(2\omega)-0.1805\cos(\omega)] \quad (27)$$

From the observation of the frequency response of the discrete-time system and the frequency response of the analog system, it can be seen that the first is periodic function of ω while the last is aperiodic. The unit step and ramp sample responses for the discrete-time amplifier are given by

$$h_{st-D}(n)=0.0953\left[(1)^n-\left(e^{-1.9874\times10^9T_S}\right)^n\right]+1.974\left[(1)^n-\left(e^{-0.6597\times10^9T_S}\right)^n\right]$$
$$-18.3445\left[(1)^n+\left(e^{-0.2101\times19^9T_S}\right)^n\right]+56.8517\left[(1)^n-\left(e^{-0.0425\times10^9T_S}\right)^n\right] \quad (28)$$

and

$$h_{ra-D}(n)=0.0953n-0.0479\times10^9\left[(1)^n-\left(e^{-1.9874\times10^9T_S}\right)^n\right]+1.974n-2.9923\times10^9$$
$$\left[(1)^n-\left(e^{-0.6597\times10^9T_S}\right)^n\right]-18.3445n+87.3136\times10^9\left[(1)^n-\left(e^{-0.2101\times19^9T_S}\right)^n\right] \quad (29)$$
$$+56.8517n-1337.6885\times10^9\left[(1)^n-\left(e^{-0.0425\times10^9T_S}\right)^n\right]$$

and both are depicted in Figs. 12 and 13, respectively for $T_S=2$ nS.

6. Conclusions

The analysis of a linear time invariant voltage series multistage feedback amplifier network at high frequencies was performed. The nodal admittance matrix of the five nodes network was constructed. An additional stage to the amplifier is possible to increase the voltage gain but this complicates the nodal admittance matrix. The transfer function resulted from the solution of the linear equations representing the system is the key function and it is useful for both design and synthesis technique by selecting numerical values in the simulation process. The value of the peak gain resulted from the nodal analysis and then evaluated from the transfer function's Bode plot was $32.2\,\mathrm{dB}\,(40.738)$ is confirmed with that calculated from the evaluating the voltage gain in each stage (with the feedback network) which was $32.11\,\mathrm{dB}\,(40.326)$ and the small difference between the two values occurs because of the simulation process in the MATLAB. The transfer function has three zeros and four poles due to the four capacitors in the network. The system exhibits high performance due to small time domain quantities and the transient response of the system was nonoscillatory, in addition to the system is stable since all the poles lies to the left of the imaginary axis. The impulse invariant method is used to simulate the amplifier and a same magnitude is obtained for both the continuous-time and discrete-time system. The steady state time which was 0.15×10^{-6} s was the same in continuous and discrete time system. The step and ramp response for the discrete-time system is analogous to the continuous-time system.

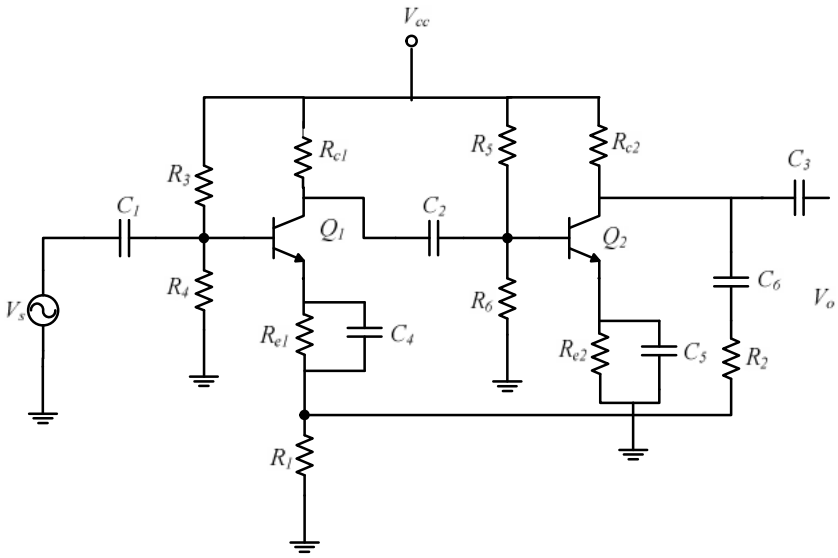

Figure (1). Multistage feedback amplifier network.

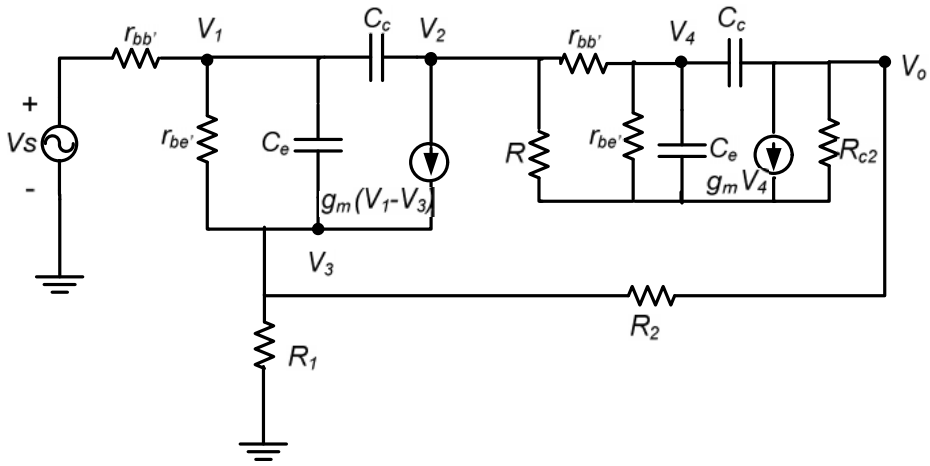

Figure (2). Small-signal hybrid-π model for voltage-series multistage feedback amplifier.

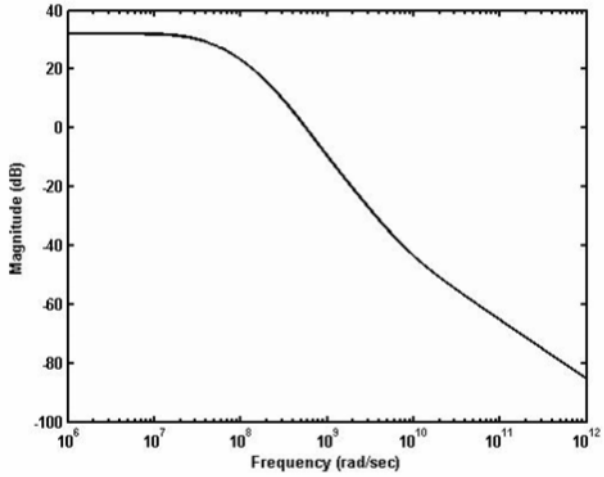

Figure (3). Bode magnitude plot for multistage feedback amplifier.

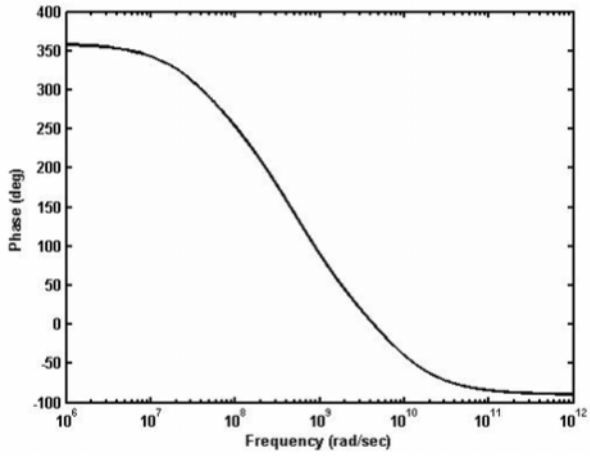

Figure (4). Bode phase plot for multistage feedback amplifier.

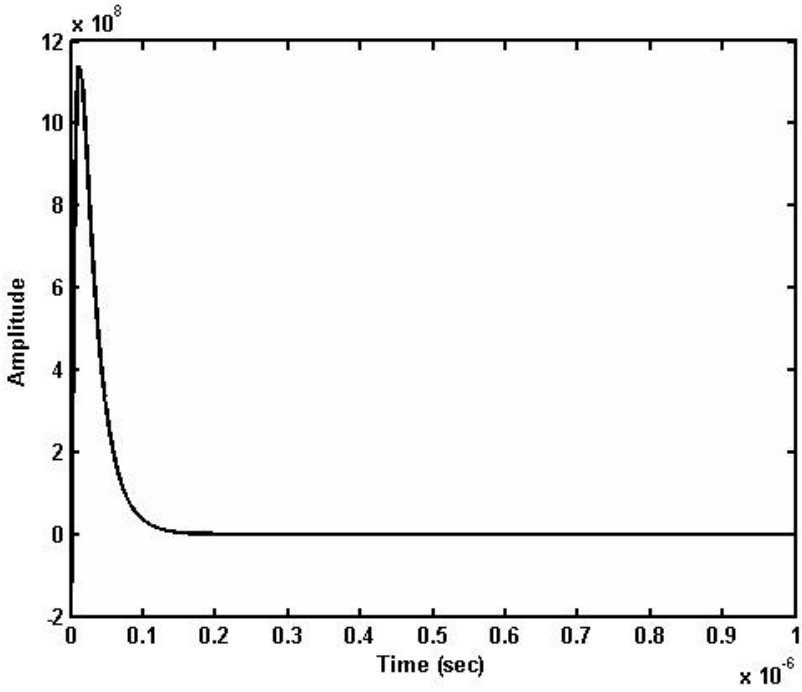

Figure (5). Unit impulse response of the multistage feedback amplifier.

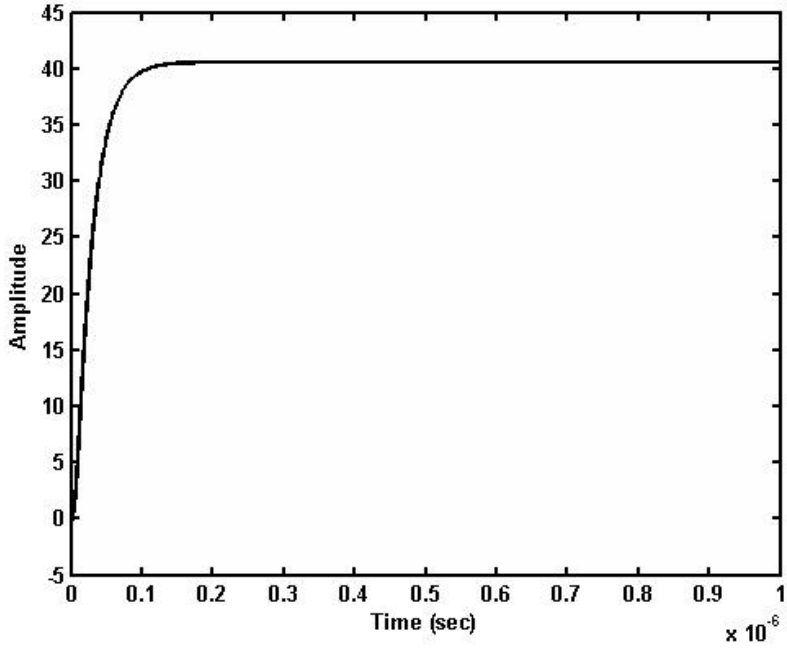

Figure (6). Unit step response of the multistage feedback amplifier.

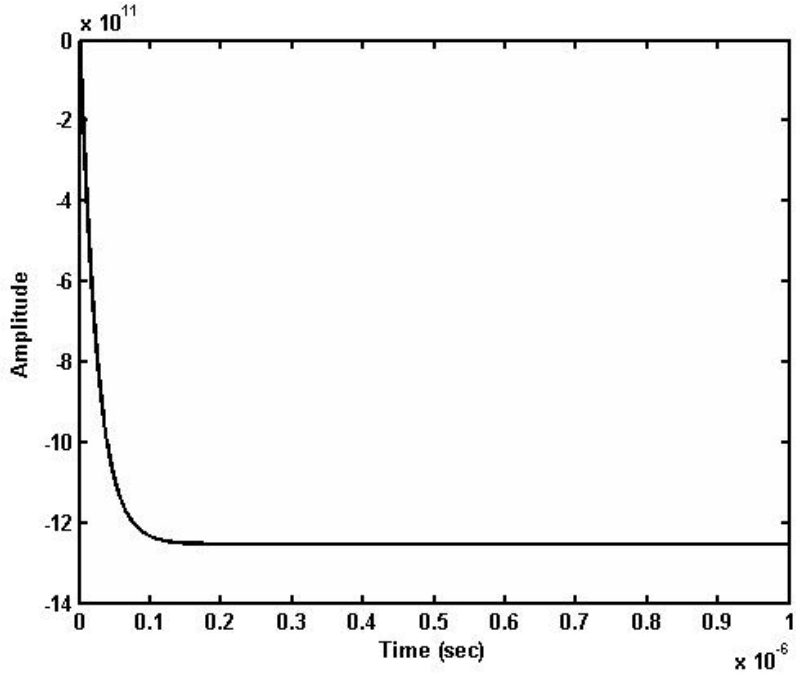

Figure (7). Unit ramp response of the multistage feedback amplifier.

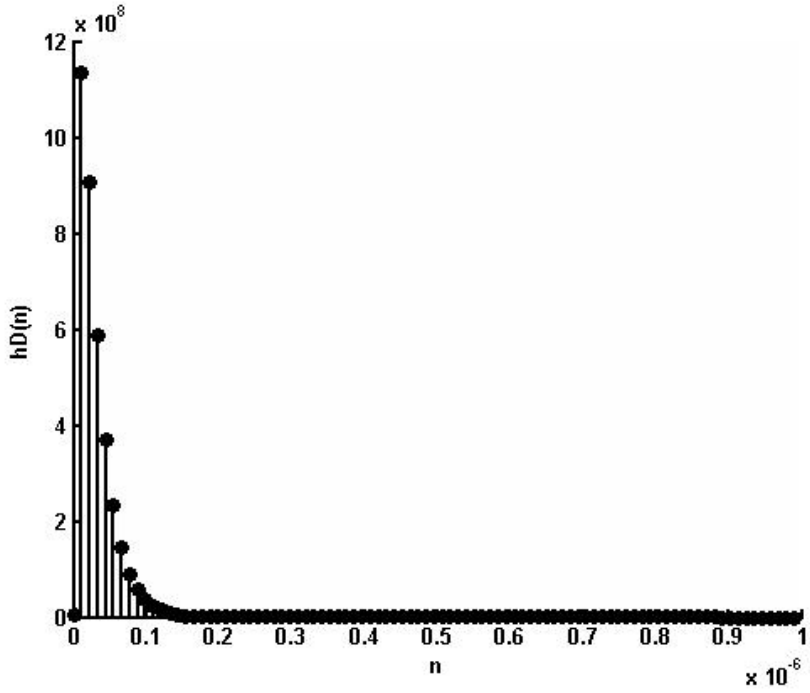

Figure (8). Unit sample response of a discrete-time feedback amplifier.

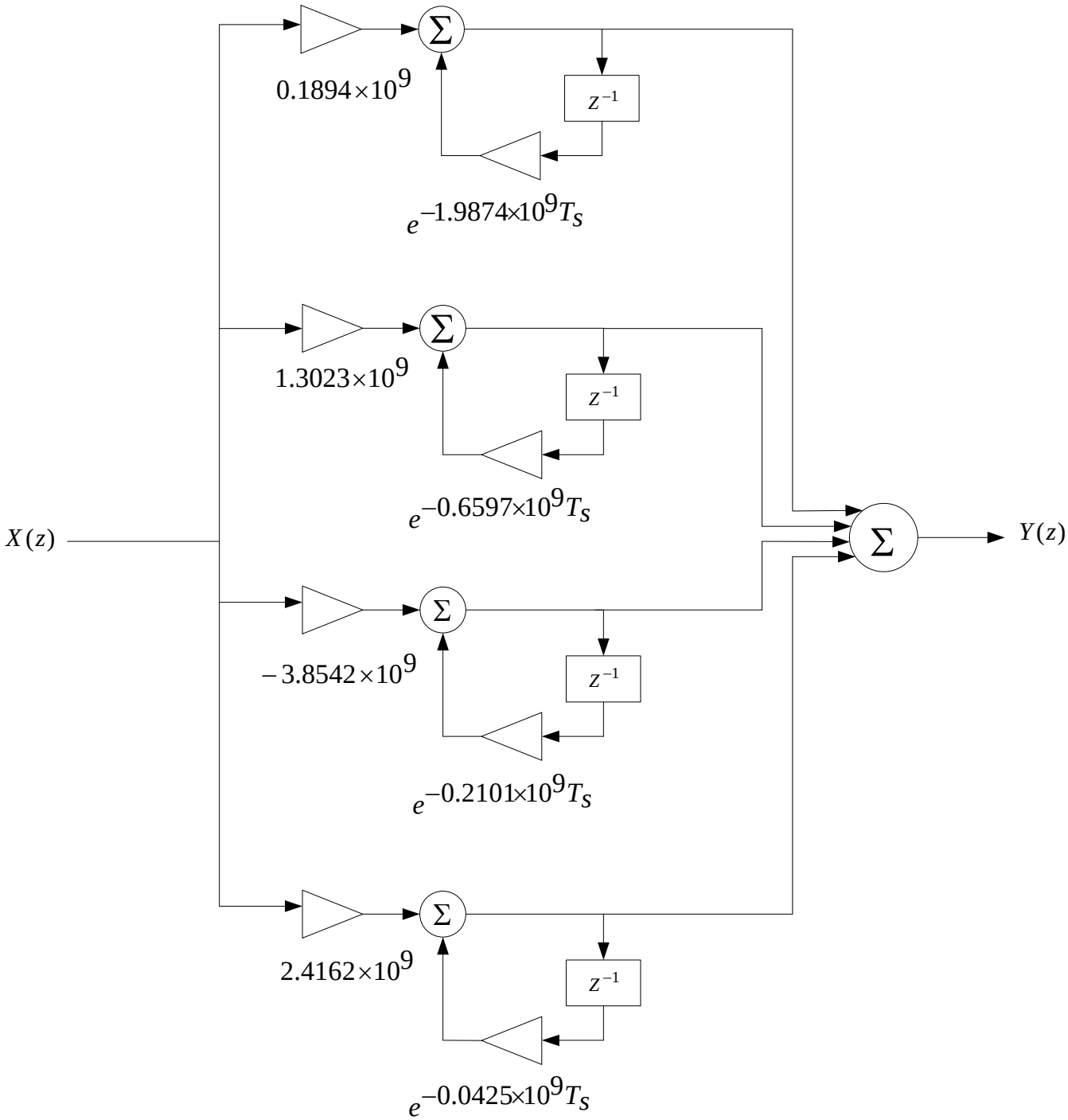

Figure (9). Simulation of an amplifier network by impulse invariant method.

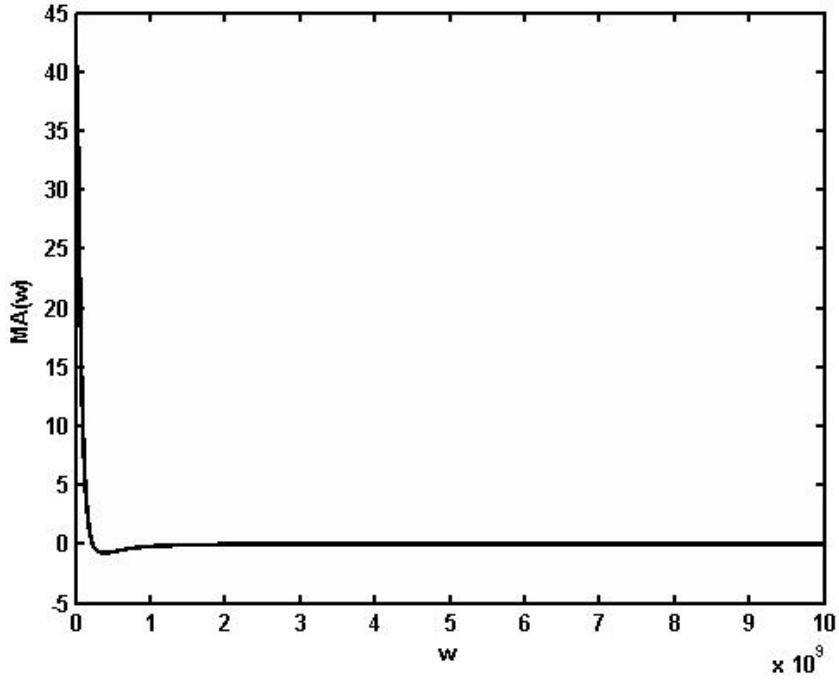

Figure (10). Magnitude response of analogue amplifier.

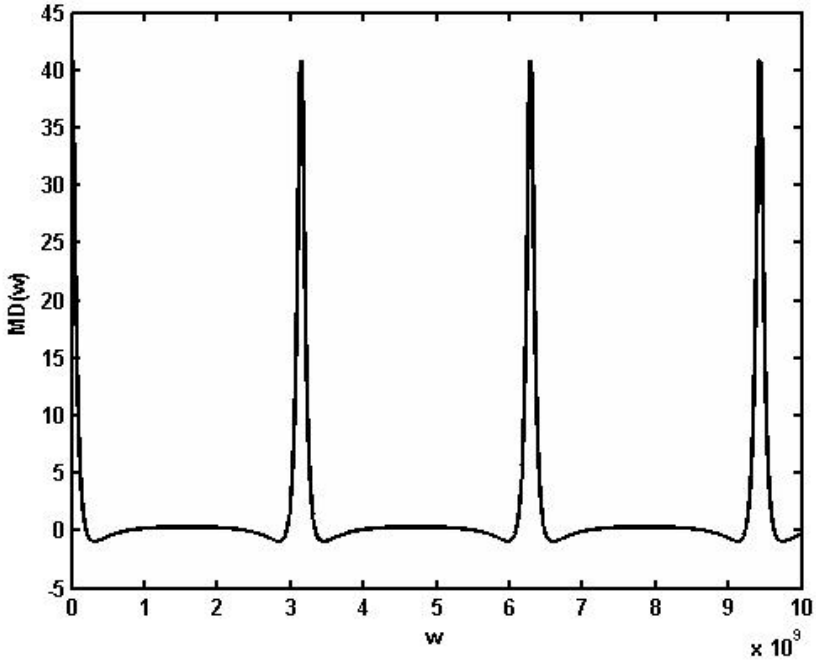

Figure (11). Magnitude response of a discrete-time feedback amplifier.

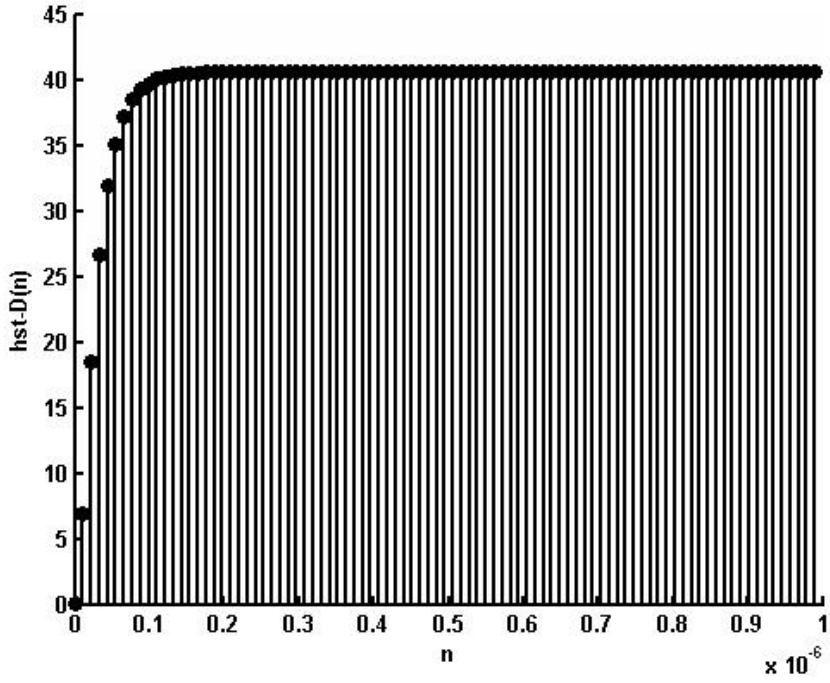

Figure (12). Unit Step sample response of a discrete-time feedback amplifier.

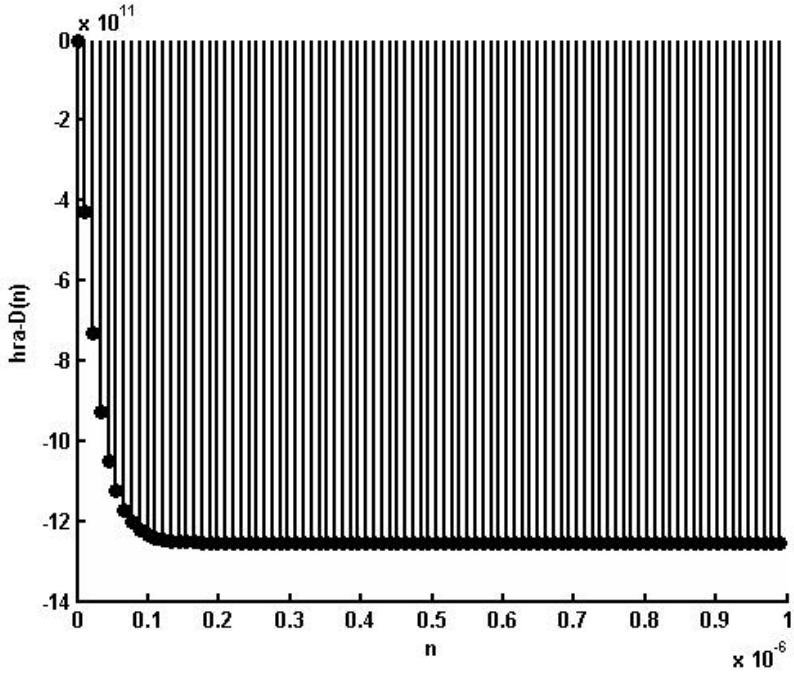

Figure (13). Unit ramp sample response of a discrete-time feedback amplifier.

7. References

[1] Kenneth A. Kuhn, **"Feedback Effects on Amplifier Response,"** http://www.kennethkuhn.com /electronics, 2010.

[2] Millman-Halkias," **Integrated Electronics,** "McGraw-Hill Inc, 1972.

[3] John Bird **,"Higher Engineering Mathematics, "** Elsevier Ltd, 2006.

[4] Katsuhiko Ogatta **,"Modern Control Engineering "** Fourth Edition, Prentice-Hall, Inc, 2002.

[5] Phillip E. Allen, and Michael b. Terry, **"The Use of Current Amplifiers for High Performance Voltage Amplifications,"** IEEE Journal of Solid-State Circuits, vol, sc-15, No. 2, April 1980.

[6] John O. Attia, **"Electronics and Circuit Analysis Using MATLAB,"** CRC Press, LLC 1999.

[7] **''Frequency Response and Stability of Feedback Amplifiers''** http://www.electronics.dit.ie/staff/ypanarin/Lecture%20Notes/K235-1/4%20feedback%20amplifiers, 2003.

[8] Daniel Williamson, **"Conversion of Analog to Digital Transfer Function,"** http://localhost/E:/Conversion%20of%20Analog%20to%20Digital%20Transfer%20Functions.mht, 2008.

[9] Finn Haugen, **"Discrete-Time Signals and Systems,"** http://techteach.no/publications, 2005.

[10] Edward W. Kamen, Bonnie S. Heck, **"Fundamentals of Signals and Systems using the WEB and MATLAB,"** Third Edition, Pearson Prentice-Hall, 2007.

[11] Rodger E. Ziemer, William H. Tranter, D. Ronald Fannin, **"Signals & Systems, Continuous and Discrete,"** Fourth Edition, Prentice-Hall, Inc, 1998.

Studying the Effect of Scale of Fluctuation on the Flow Through an Earth Dam Using Stochastic Finite Element

Ressol R. Shakir

Civil Engineering Department

College of Engineering

Thi-Qar University

Abstract

Estimation of quantity of flow through earth dams by using finite elements method mainly depends on the magnitudes of permeability for the earth dam. The permeability of soil medium may be included in the solution as constant permeability or non homogeneous, anisotropic or may be distributed as random field. Simulation of properties of soil by using random fields' generators has great interest nowadays. This paper includes studying of the effect of anisotropy of scale of fluctuation of the permeability through the stochastic finite elements analysis for case of flow through earth dam. Permeability has been simulated by random field and mapped into finite element methods according to the most recent studies. The results have shown that (1) quantity of seepage through stochastic earth dam is always less than that calculated for deterministic state. (2) As horizontal to vertical scale of fluctuation (anisotropy of scale of fluctuation) increases, quantity of seepage increases but it still less than that for deterministic state. The seepage elevation is also reduced at random field state compared to deterministic solution.

Keywords: Flow; stochastic finite element, earth dam; scale of fluctuation.

دِراسَة تأثير مِقياس التقلّبِ على التدفق خلال سدٍّ ارضي باستعمال عناصر محدودة عشوائية

المستخلص

تقدير كميةِ التدفق خلال السدودِ الأرضِية بإستعمال طريقةِ العناصر المحدودةِ تَعتمدُ بشكل رئيسي على مقادير النفاذيةِ للسد الترابي فإذية وسطِ التربةِ قَدْ تُتضمّنُ في الحَلِّ كنفاذية ثابتة أوغير متجانسة غير متماثلة أوقَدْ تَوزّعُ كحقل عشوائي. محاكاة خصائص التربةِ بإستعمال مولّداتِ الحقول العشوائيةِ لها إهتمامُ عظيمُ هذه الأيامُ. يتضمن هذا البحث دِراسَة تأثير اللاتماثل لمِقياس تقلّبِ النفاذيةِ خلال تحليلِ عناصر محدودة عشوائية لحالةِ التدفق خلال سد ارضي. النفاذية تم محاكاتها بحقل عشوائي وخطّطتْ إلى طرق العنصر المحدودةِ طبقاً لآخر الإرسالاتِ. النَتائِج بينت بأنّ (1) كمية التسرب خلال سد ترابي عشوائياً أقل مِنْ تلك المَحْسُوبةِ للحالةِ الحتميةِ. (2) زيادة مقياس التقلب الافقي الى العمودي (مِقياس اللاتماثل

للقلّبِ) يزيد من كمية التسرب لكنَّها ما زالتْ أقل مِنْ التي للحالةِ الحتميةِ.إنّ إرتفاعَ التسرب يخفّضُ أيضاً عند الوسط العشوائيمُقَارَنة مع الحالةِ الحتميةِ.

1. Introduction

It is well known that properties of soil at the site are different from point to point. Permeability is the important soil property that used in calculation of quantity of seepage in different projects such as seepage through earth dam. Studying the variability of permeability of soil through the soils has revealed that permeability may be simulated as a random field. Design of earth dam most widely considers the average values (first moment of statistics) of permeability in case of different values are found for small regions in the earth dam medium. If the permeability simulated as random field, standard deviation and correlation are necessary to be used.

Finite element method is combined with random filed concept in two ways: directly included in finite element formulation such as those researched by (Freeze, 1975, Dagan 1993,) [1,2] or indirectly included to finite element code in which the random field is manipulated in isolated form then mapped to the finite element such as those developed by (Fenton and Griffiths, 1993) [3]. A good review on stochastic finite element can be found on **Stefanou** (2009) [4].

Spatial variability of soil property such as permeability has been investigated by Griffiths and Fenton 1993, Popescu, et, al., 2005, Hoeksema 1985, Ahmed 2009 [5,6,7,8]. These studies have shown that flow rates calculated based on permeability simulated as random field are less than flow rates calculated based on average permeability solution which is called deterministic solution. This conclusion has a great attention in design and it increases the importance for further studies on the effect of scale of fluctuation “correlation through distance”. Very few researchers study the effect of anisotropy of scale of fluctuation on the rate of flow. For instance Ahmed, 2009 [8] reported that anisotropy of permeability decreases the flow rate for a simple dam with core. In spite of that the subject still need more researches and more range of scale of fluctuation should be included in calculations.

This research has used fixed mean and variable standard deviation for soil permeability property to study the effect of permeability on the rate of flow through earth dam utilizing the finite element method plus random field generation for permeability property. They are merged together to get a stochastic finite element analyses (Griffiths and Fenton, 1993) [5]. The main objective of this study is to investigate the effect of random field permeability on the flow rate. Variance and spatial correlation effects on the quantity of seepage are

investigated also. Anisotropy of scales of fluctuation effects are also investigated since it mostly represents the real case of soil in the field.

2. Mean and covariance

It is well known from site investigations that soil properties differ from point to point. If these properties are simulated as random field, they can be characterized by first and second moment of statistic. In spit of that classic design uses just the first moment "mean value" which can be expressed mathematically as

$$u = \frac{\sum x_i}{N} \tag{1}$$

Where u is the mean value; N is the number of events; x is the event.

However the second moment of statistic (Equation 2) has an effect and should be taken specially when a lot of data concerning a property are

$$\sigma_x = \sqrt{\frac{x_i - u}{N}} \tag{2}$$

Sometimes the coefficient of variation is used instead of variance which is equal to standard deviation to the mean value. It is reasonable to say that soil properties through short distance are more correlated than long distance. Spatial correlation is measured by scale of fluctuation which is defined as the distance over which the properties show appreciable correlation (Jaksa et. al., 1999) [9].

Stochastic model

Very few researches have been done in the investigation of spatial variation of soil properties in a stochastic finite element method. It has been applied for different applications in geotechnical engineering such as flow through earth dam. It consists of two parts: the first is an ordinary two dimensional finite element model for flow through earth dam developed by Smith and Griffiths (1998)[10] and the second is the random field model for permeability property. The results of random field permeability are mapped to the finite element model (Fenton and Griffiths,1996) [3].

Flow through earth dam is governed by Laplace's equation.

$$k_x \frac{\partial^2 \phi}{\partial x^2} + k_y \frac{\partial^2 \phi}{\partial y^2} = 0 \tag{3}$$

where ϕ is fluid potential and k_x , k_y are permeability in x, y direction.

The Laplace differential equation has been implemented in a program that has been developed by several researchers such as Smith and Griffiths (1998) [10]. The program can compute the free surface location and flow through the earth dam using a two-dimensional iterative finite element model for constant or variable permeability. Finite element program developed to solve problems without random field permeability such as flow through earth dam was developed originally by Smith and Griffiths, (1998) [10]. Another development in analysis of anisotropy of permeability of typical earth dam or core installed in large earth dam was by Shakir (2004), Shakir, (2009) and Shakir, (2011)[11,12,13]. The combination of finite element with random field has been developed by Fenton and Griffiths, 1996 [3].

3. Permeability field generation

Permeability is considered to be log normally distributed in accordance with the field measurements as determined by Freeze (1975), Hoeksema and Kitanidis (1985), Sudicky, (1986) [1,7,14] and reported by Griffiths and Fenton (1993) [5]. Permeability is expressed as K(x) where x is any point in the two dimensional field of soil. Variance and "σ_{lnk}^2" mean "u_{lnk}^2" are the first and second moment of statistics for the normally distributed "ln k". These measures are represented by the following two equations.

$$\sigma_{\ln k}^2 = \ln\left(1+\frac{\sigma_k^2}{\mu_k^2}\right) \tag{4a}$$

$$\mu_{\ln k} = \ln(\mu_k) - \frac{1}{2}\sigma_{\ln k}^2 \tag{4b}$$

It is reasonable to think that the permeability value at a point is highly correlated with the permeability at close point and in contrast the permeability at a point is different from permeability at another point far from the first point "poorly correlated". The distance between the two points is called scale of fluctuation. Correlation structure can be modeled depending on field observations. Generally, It can be defined mathematically as following (Sudicky, 1986) [14].

$$\rho(\tau) = \exp\left\{-\frac{2}{\theta}\tau\right\} \tag{5}$$

Where ρ is the correlation coefficient between two points separated by a large distance τ. Above function is a function of the distance between two points ($\tau = x_i - x_j$). This model

indicates that correlation ρ decay exponentially. θ is the scale of fluctuation which is defined as the distance beyond which the field is effectively uncorrelated (Vanmarke 1984) [15]. This relation is modeled depending on expensive observation of permeability value in the field. Confirming this equation is difficult since it depends on large data which are expensive to be obtained. Figure (1) demonstrates the effect of increasing the distance τ with respect to θ on the correlation structure ρ. For instance, when θ is equal to 50 the correlation coefficient, ρ, is equal to 0.135 at distance τ=50.

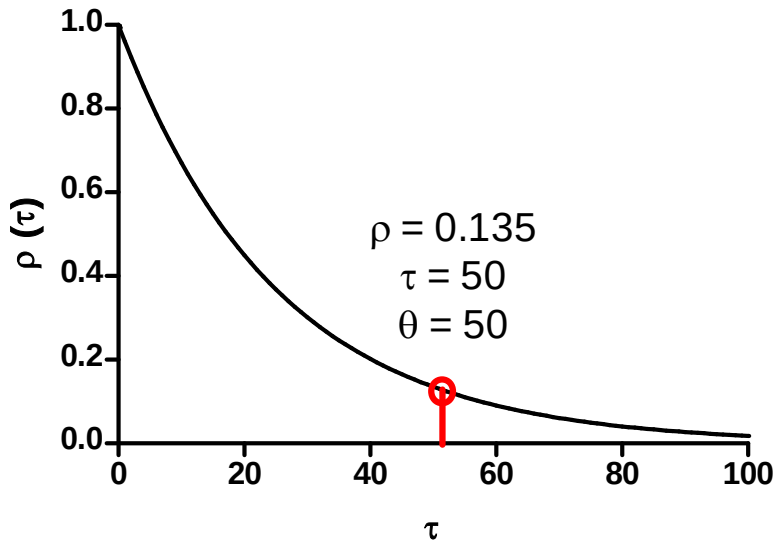

Figure (1). Effect of distance on the correlation of permeability property (Eq. 5).

If the permeability properties are observed at field, the problem is simple. We just mapped these values in the finite element program. Mostly large number of permeability values is not available but we can get mean and variance and also the correlation structure. According to that we can get the distribution by Monte Carlo simulation to give a picture of permeability through the field.

$$k_i = \exp\{\mu_{\ln k} + \sigma_{\ln k} g_i\} \quad (6)$$

Where u_{lnk} is the mean and σ_{lnk} is the standard deviation of the lognormal distributed k_i. Uniform permeability on each realization can be obtained as scale of fluctuation goes to infinity. In contrast the permeability is different rapidly from element to element as scale of fluctuation goes to zero. G_i is derived from the standard Gaussien random field g through using LAS (Local average subdivision developed by Fenton and Vanmark 1990 [16]

technique with zero mean and unit variance and a spatial correlation controlled by the scale of fluctuation (Vanmarcke 1984) [15].

Application

The size of the dam is shown in Figure (2). The base width was 20 m, the top width was 2 m and the height was 10 meter. Through random field generation the permeability has different values from element to element. About 605 program executions were performed. Table 1 shows a list of sets of values of scale of fluctuation and covariance used in this study. On the other hand the value of quantity of seepage is calculated for the same problem using mean value of permeability. For case of k =0.1 cm/s based on the solution of Gilbowy, (Harr, 1962) [17] Δ=9 m; 0.3Δ = 2.7 m; d= 13.7 m; α = 48^{o}, m =0.42; q = kmh = 0.1 (0.42)(10) = 0.42; q/(kh) =0.42. The finite element based solution used in this study gives approximately the same result (q/kh=0.42) .

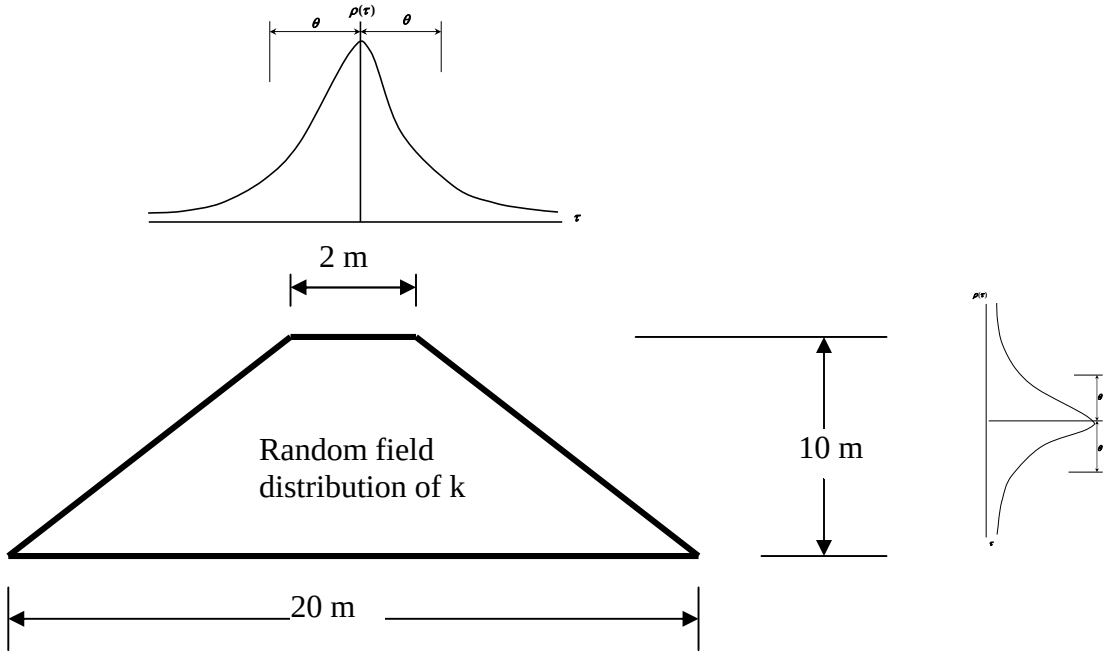

Figure (2). Dimensions of earth dam.

Table (1). Set values included to the stochastic program.

σ_k/u_k	θ_x	θ_y	σ_k/u_k	θ_x	θ_y	σ_k/u_k	θ_x	θ_y	σ_k/u_k	θ_x	θ_y	σ_k/u_k	θ_x	θ_y
0.1	0.1	0.1	0.1	0.1	0.8	0.1	0.1	3.2	0.1	0.1	6.4	0.1	0.1	12
0.2	0.2	0.1	0.2	0.2	0.8	0.2	0.2	3.2	0.2	0.2	6.4	0.2	0.2	12
0.4	0.4	0.1	0.4	0.4	0.8	0.4	0.4	3.2	0.4	0.4	6.4	0.4	0.4	12
0.8	0.8	0.1	0.8	0.8	0.8	0.8	0.8	3.2	0.8	0.8	6.4	0.8	0.8	12
1.6	1.6	0.1	1.6	1.6	0.8	1.6	1.6	3.2	1.6	1.6	6.4	1.6	1.6	12
3.2	3.2	0.1	3.2	3.2	0.8	3.2	3.2	3.2	3.2	3.2	6.4	3.2	3.2	12
6.4	6.4	0.1	6.4	6.4	0.8	6.4	6.4	3.2	6.4	6.4	6.4	6.4	6.4	12
12	12	0.1	12	12	0.8	12	12	3.2	12	12	6.4	12	12	12
24	24	0.1	24	24	0.8	24	24	3.2	24	24	6.4	24	24	12
48	48	0.1	48	48	0.8	48	48	3.2	48	48	6.4	48	48	12

4. Effect of covariance and scale of fluctuation

The problem of flow through the earth dam shown in Figure (2) has been solved for two cases. The first case includes using the specified permeability in all elements of the mesh and the second includes using permeability as random field. In literature the first one may be called deterministic solution and the second is undeterministic solution.

The normalized quantity of flow (q/kh) that obtained from deterministic solution (4) contains using average permeability. Figure (3) shows the relationship between normalized quantity of seepage versus covariance (σ_k /μ_k). As covariance amount increases, normalized quantity of seepage decreases. This conclusion is compatible with solution of Ahmad, (2009) [8] and also the solution of Griffiths and Fenton (1993) [5]. This means that allowable quantity of seepage is in the safe side and is greater than semi real case of random field. The flow in any studied cases will not increase more than the deterministic state.

In the same previous figure, using fixed scale of fluctuation in y direction θ_y = 0.1 and using different scales of fluctuation in x direction θ_y = 0.1 to 96 causes different results. Increasing of the scale of fluctuation in x direction increases the normalized quantity of seepage especially when covariance, (σ_k/u_k) exceeds the value of 0.7. Decreasing of scale of fluctuation causes high probability to existence of elements with small permeability and increasing the scale of fluctuation causes small probability to existence of element with low permeability. This may interpret the difference between the two cases of using scale of fluctuation. Increasing of Cov, (σ_k/u_k) more than 0.1 makes the normalized quantity of seepage decreases. This is reasonable since the high permeability variance affect flow more than low variance. High variance in permeability gives high variance in seepage.

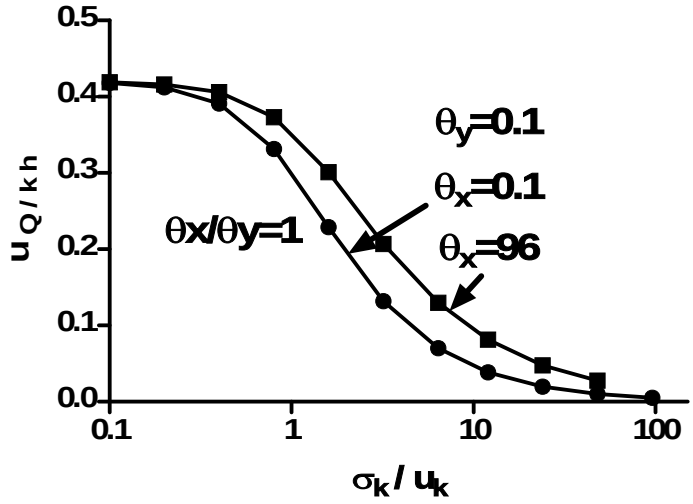

Figure (3). Relation between normalized quantity of seepage and covariance.

Figure (4) shows the relationship of the standard deviation of the quantity of seepage versus the covariance (standard deviation to mean value) of permeability. The standard deviation increases as correlation factor increases at covariance equal 1.6 the curve decays i.e. the standard deviation decreases. For instance at $\sigma_k / \mu_k = 0.4$ the standard deviation σ_Q equals 0.0275 at $\theta = 0.1$ while it reaches 0.048 (maximum) at $\sigma_k / \mu_k = 1.6$ after that it decreases. Scale of fluctuation has an effect on the σ_Q as it increases the standard deviation increases. This is may be attributed to increase the potential of existence elements with high difference in quantity of seepage value. This phenomenon is reported previously by Griffiths and Fenton, (1993) [5] and the result in this section confirms this phenomenon for wide range of sale of fluctuation.

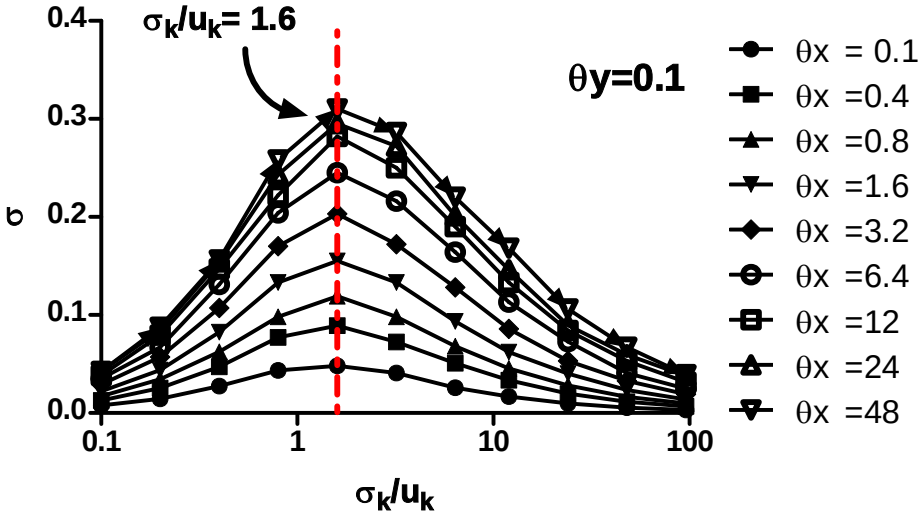

Figure (4). Quantity of seepage variance versus covariance.

5. Scale of fluctuation

Figure (5) shows the relationship between normalized quantity of seepage versus scale of fluctuation in x direction, $\theta_{x,}$ for a selected value of scale of fluctuation (the spatial correlation length) in y direction (0.1; 0.8, 3.2 and 6.4. The covariance, COV, (σ_k/u_k) was selected as 3.2. As the scale of fluctuation increases, the quantity of seepage increases. The scale of fluctuation is interpreted as the distance over which correlation is significant. Since many of the statistics of interest depend strongly on the scale of fluctuation, different scales of fluctuation are implemented. Some studies have considered the permeability and scale of fluctuation for reconstituted soil used in earth dam as isotropic (Fenton and Griffiths 1996) [3], however layered construction may lead to anisotropy. Strong correlation is referred by large scale of fluctuation which means the value of normalized quantity reach to the deterministic value and vise versa. This compatible which theoretical results that as scale of fluctuation reach infinity deterministic value will be identified. (Fenton and Griffiths, [3] 1996, Prospuc et al., 2005) [6].

For very short scales of fluctuation, the flow rate is small, while it increases dramatically as the scale of fluctuation increases Figure (5). At θ_x =0.8 normalized quantity of seepage approximately equals 0.1 which is very low. It shows a good representative flow through dam. At high scale of fluctuation θ_x =10 normalized quantity of seepage approximately equals 0.2 which is greater than that at small scale of fluctuation. The spatial correlation length, also known as the scale of fluctuation, describes the distance over which the spatially random values will tend to be correlated in the underlying Gaussian field. Thus, a large value will imply a smoothly varying field, while a small value will imply a ragged field. For more discussion of the spatial correlation length, the reader is referred to Vanmarcke (1984), Wickremesinghe, (1993) and Jaksa et. al., (1999) [15, 18 , 9].

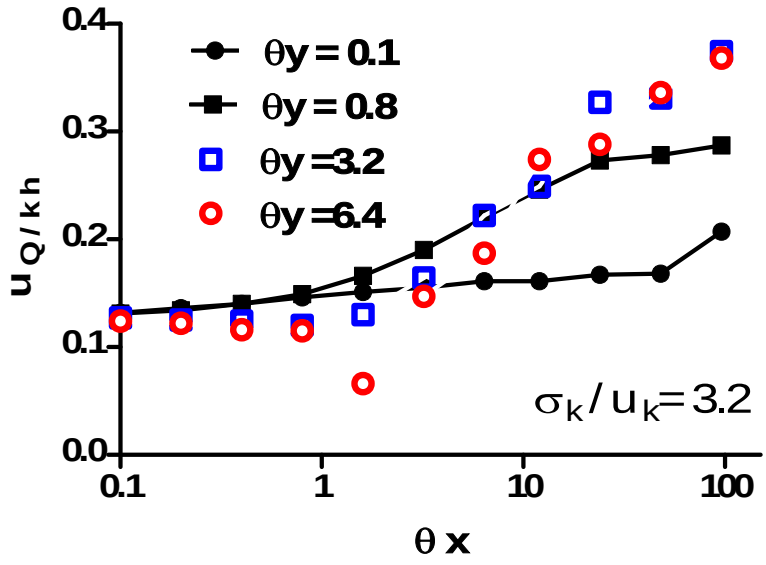

Figure (5). Normalized quantity of seepage versus scale of fluctuation in x direction.

6. Anisotropy of scale of fluctuation

Permeability property in y direction is spatially correlated assuming magnitudes smaller than that in x direction. That can be expressed in term of scale of fluctuation. The scale of fluctuation in vertical direction is smaller than the scale of fluctuation in x direction because of the stratification of soil that makes the water flow as in pipes in the horizontal direction. Figure (6) shows the effect of anisotropy of scale of fluctuation on the result of normalized quantity of flow. The result is somewhat scatter. It is different little from the finding of Ahmed, (2009) [8] who concluded that the quantity of seepage increases as ratio of horizontal to vertical increases. From the study results it was found that at θ_x / θ_y less than unity the normalized quantity increased dramatically and after that the increase in normalized quantity of seepage is slight increase.

Quantity of seepage increases as scale of fluctuation in x direction increases θ_x Figure (6). When horizontal scale of fluctuation is high i.e. strongly correlated (θ_x = 96), quantity of seepage approximately close to deterministic state for case of θ_y = 6.4 i.e. vertical scale of fluctuation slightly increases. For case of small horizontal scale of fluctuation θ_x = 1 for θ_y =0.1, 0.8, 3.2, 6.4, quantity of seepage equal to 1.3. Small horizontal scale of fluctuation means possibility of small permeability for row of cell, that is, make the quantity of seepage small also. The result was presented for σ_k/u_k = 3.2

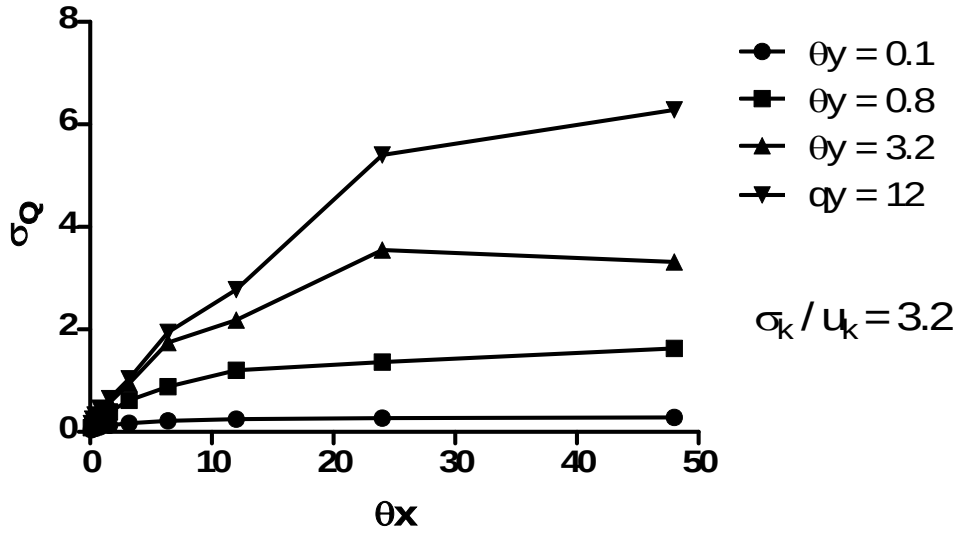

Figure (6). Standard deviation of quantity of seepage versus scale of fluctuation in x direction.

7. Effect of the standard deviation of permeability

Figure (7) shows the relation between flow rate and standard deviation for different scales of fluctuation in x direction. Flow rate changes as standard deviation changes also. The standard deviation of the flow rate increases as flow rate increases until it reaches to value 2.5 then the standard deviation decreases. Scale of fluctuation affects the standard deviation values too much as demonstrated in the graph.

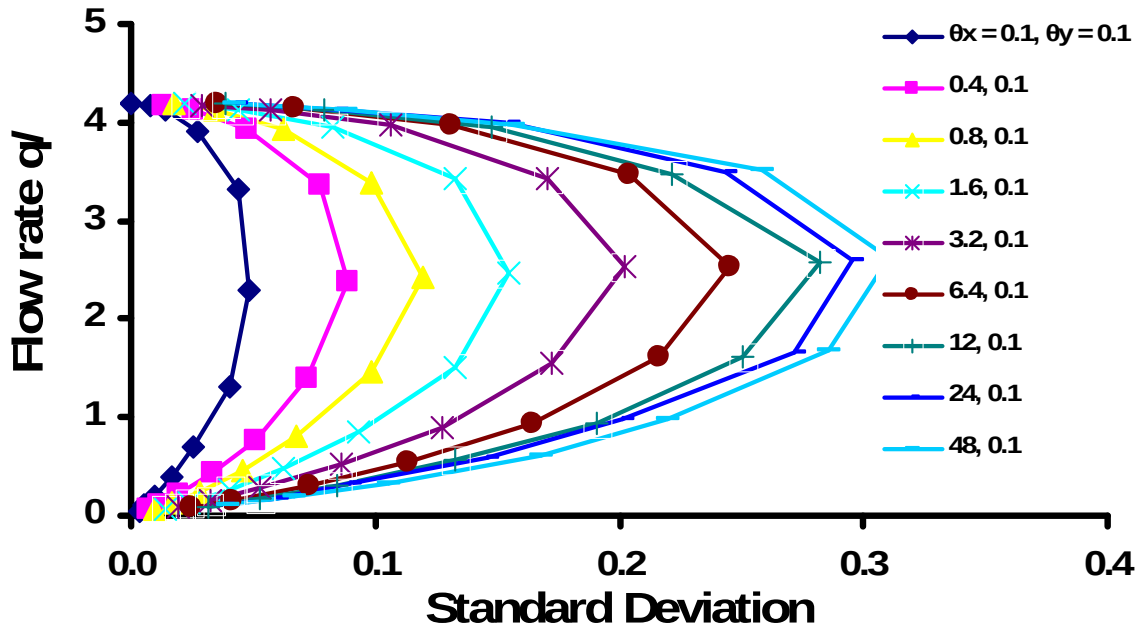

Figure (7). Relation between standard deviation and flow rate.

8. Seepage elevation

Seepage elevation (drawdown) is defined as the elevation of the point on the downstream face of the dam at which the water first reaches the dam surface. This section shows the results of the amount of drawdown of the free surface at the downstream face of the dam. The magnitude of seepage elevation is very important since it determines the height according to which the treatment is desired. The results obtained by executing the program for many times for different value of scale of fluctuation are presented in this section. The relation between seepage elevation and standard deviation is mapped for every percentage of scale of fluctuation Figure (8). Seepage elevation decreases as standard deviation increases. Increasing standard deviation means high difference around the average. High variability may cause reduction in the seepage elevation since existing of small permeability inputs

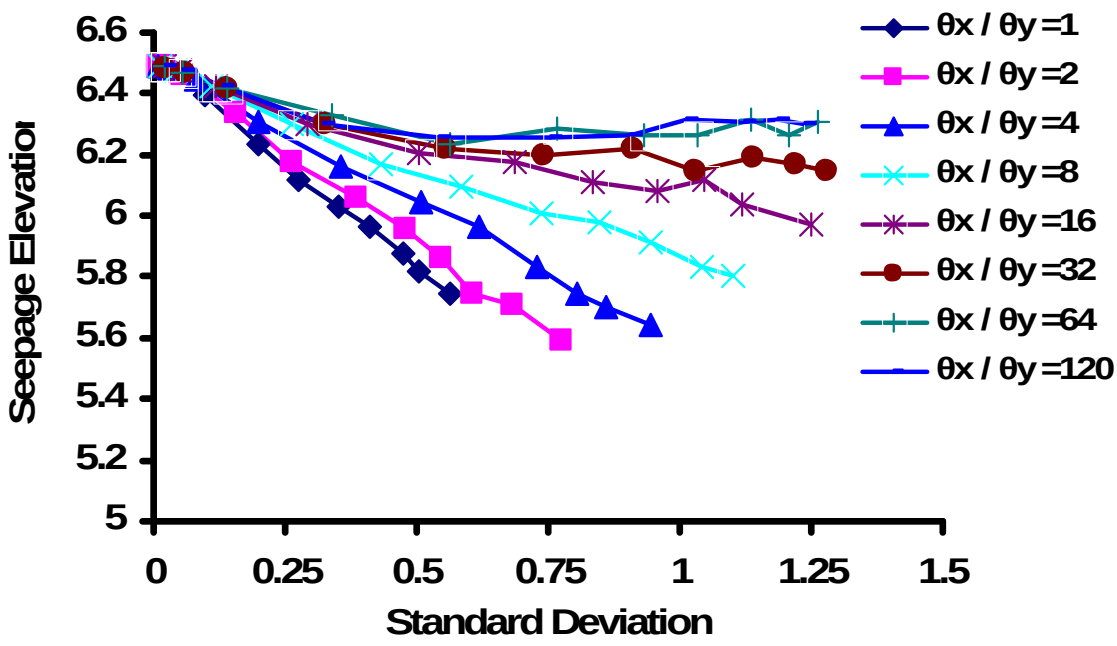

Figure (8). Relation between seepage elevation and standard deviation.

9. Conclusion

Flow through stochastic earth dam has been studied including the effect of anisotropy of scale of fluctuation. The result of research outlines the following conclusions: (1) quantity of seepage through stochastic earth dam is always less than that calculated for deterministic solution which confirms the conclusion of other researchers. This conclusion is very important for design. It means the design on average permeability is in the safe side. (2) It is found that as horizontal to vertical scale of fluctuation (anisotropy of scale of fluctuation increases, quantity of seepage increases but it still less than that for deterministic state (case of average value). (3) Variance of quantity of seepage depends on covariance value. It increases until covariance approximately equals two, then it decreases. (4) Seepage elevation is also decreases as scale of fluctuation decreases.

10. References

[1] Freeze, R.A. (1975). "A stochastic-conceptual analysis of one-dimensional groundwater flow in nonuniform homogeneous media," *Water Resources Res.*, **11**(5), 725–741.

[2] Dagan, G. (1993). "Higher-order correction of effective conductivity of heterogeneous formations of lognormal conductivity distribution," *Transp. Porous Media*, **12**, 279–290.

[3] Fenton, G. A., and Griffiths, D. V. (1996), Statistics of free surface flow through a stochastic earth dam, J. Geotech. Eng., 122, 422–436.

[4] Stefanou, G. (2009) The stochastic finite element method: Past, present and future, Computer Methods in Applied Mechanics and Engineering Volume 198, Issues 9-12, 15 February, Pages 1031-1051.

[5] Griffiths, D.V. and Fenton, G.A. (1993). "Seepage beneath water retaining structures founded on spatially random soil," *Geotechnique*, 43(4), 577–587.

[6] Popescu, R. ; Prevost, J. H. ; Deodatis, G. (2005) Effects of spatial variability on soil liquefaction: some design recommendations" Géotechnique, Volume 47, Issue 5, pages 1019 –1036 , ISSN: 0016-8505, E-ISSN: 1751-7656; DOI: 10.1680/geot.1997.47.5.1019.

[7] Hoeksema, R.J. and Kitanidis, P.K. (1985). "Analysis of the spatial structure of properties of selected aquifers," *Water Resources Res.*, **21**(4), 563–572.

[8] Ahmed A. A. (2009) "Stochastic analysis of free surface flow through earth dams." Computers and Geotechnics, Vol. 36, No. 7, pp 1186-1190.

[9] Jaksa, M.B., Kaggwa, W.S. & Brooker, P.I. 1999. Experimental Evaluation of the Scale of Fluctuation of a Stiff Clay. Proceedings 8th Int. Conference on the Application of Statistics and Probability, R. E. Melchers and M. G. Stewart (eds.), Sydney, (Publ. 2000), Vol. 1. Rotterdam: A. A. Balkema: 415–422.

[10] Smith, I.M. and Griffiths, D.V. 1998. Programming the Finite Element Method, (3rd Ed.), John Wiley & Sons, New York, NY.

[11] Shakir, R. R. (2004) "Estimating the Quantity of Seepage Under Single Sheet Pile through Two Layered Soil" Eng. and Tech. Journal.

[12] Shakir, R. R. (2009) "Quantity of Flow through a Typical Dam of Anisotropic Permeability, Computational Structural Engineering, 1301–1308. " Edited by Yuan, J.Z. Cui and Mang, H.

[13] Shakir, R. R. (2011) "Effect of an impervious core constructed into a large earth dam on the quantity of seepage" Thi-Qar University Journal of Engineering Science Vol. 2, No. 2. P 1:17.

[14] Sudicky, E.A. (1986). "A natural gradient experiment on solute transport in a sand aquifer: Spatial variability of hydraulic conductivity and its role in the dispersion process," *Water Resources Res.*, **22**(13), 2069–2083.

[15] Vanmarcke, E.H. (1984). *Random Fields: Analysis and Synthesis*, The MIT Press, Cambridge, Massachusetts.

[16] Fenton, G.A. and Vanmarcke, E.H. 1990. Simulation of Random Fields via Local Average Subdivision, ASCE, J. Engrg. Mech., 116(8), 1733.1749.

[17] Harr M. E. (1962). Ground water and seepage, McGraw-Hill, New York, 315.

[18] Wickremesinghe, D. & Campanella, R.G. 1993. Scale of Fluctuation as a Descriptor of Soil Variability. Proceedings of Conference on Probabilistic Methods in Geotech. Engrg., Canberra. Rotterdam: A. A. Balkema: 233–239.

11. Nomenclature

Symbols

u	Mean value;
N	Number of events
x	Event
ϕ	Fluid potential
k_x	Permeability in x direction
k_y	Permeability in y direction
σ_{lnk}^2	Variance i.e. second moment of statistics for the normally distributed “ln k”
u_{lnk}^2	Mean i.e. first moment of statistics for the normally distributed “ln k
ρ	Correlation coefficient between two points separated by a large distance τ.
θ_x	Scale of fluctuation in x direction
θ_y	Scale of fluctuation in y direction
σ_k/u_k	Covariance
σ_k	Standard deviation

Numerical Simulation of Parallel Flow Microchannel Heat Exchanger with Isosceles Right Triangular Geometry

Hayder M. Hasan

Machines and Equipments Department
Shatra Technical Institute

Abdul-Muhsin A. Rageb

Mechanical Department
College of Engineering
University of Basrah

Abstract

The isosceles right triangular microchannl heat exchanger performance was numerically investigated in this work. Hydrodynamics and heat transfer characteristics in a laminar, 3-D, incompressible, single-phase, steady state, parallel flow are proposed. The solution was obtained by solving the continuity and Navier-Stokes equations (momentum equations) for the hot and cold fluids by using pressure-correction method to obtain the velocity distribution, and then the energy equations for the two fluids and the separating wall are solved simultaneously as second step. The governing equations are discretized using finite-volume method-upwind differencing scheme, and then these are solved using SIMPLE algorithm method on staggered grid with FORTRAN code. The study investigated various parameters that can effect on the exchanger effectiveness and other performance parameters. From the obtain ned results it was found that the factors affecting the effectiveness are: Reynolds number Re, thermal conductivity ratio K_r, hydraulic diameter D_h and channel volume. Increasing of Re, D_h and channel volume each separately leads to decrease the effectiveness while increasing of K_r up to K_r =10 leads to increase the effectiveness. Also, it was found that the factors affecting on pressure drop are: Re, D_h and channel volume. Increasing of Re leads to increase pressure drop while increasing of D_h and channel volume each separately leads to decrease pressure drop.

Keywords: parallel flow, microchannel heat exchanger and numerical solution.

التمثيل العددي لمبادل حراري متوازي الجريان ذي قنوات مايكروية ذات شكل مثلث متساوي الساقين وقائم الزاوية

المستخلص

يتضمن العمل الحالي دراسة مبادل حراري مايكروي متوازي الجريان ذو قنوات مثلثة الشكل (قنوات ذات شكل مثلث متساوي الضلعين وقائم الزاوية) بطريقة عددية. الخصائص الهيدروديناميكية وخصائص انتقال الحرارة تمت دراستها في جريان طباقي ثلاثي الأبعاد وفي حالة الاستقرار ولا انضغاطي. تم حل المسالة الحالية على خطوتين وكما يلي: حل معادلة الاستمرارية (continuity equation) ومعادلات الزخم (momentum equations) وبطريقة التصحيح للضغط (pressure-correction method) لحل مشكلة الازدواج التي تحدث بين السرعة والضغط، والتي تكون صالحة للحل الحالي (pressure-velocity coupling) لايجاد توزيع السرعة كخطوة أولى، بعد ذلك حل معادلات الطاقة (energy equations) للمائعين والجدار الذي يفصل بينهما انيا كخطوة ثانية. وقد تم تحويل المعادلات الحاكمة إلى الشكل العددي باستخدام طريقة الحجوم المحددة (finite-volume method) وتم حل هذه المعادلات باستخدام (SIMPLE method) مع شبكة نقاط متداخلة (staggered grids) وباستخدام لغة فورتران (FORTRAN). كذلك درست مجموعة من العوامل التي تصف مسألة المبادل مثل الفعالية وغيرها. من خلال ملاحظة النتائج المستحصلة من الحل العددي، تبين بأن هناك مجموعة من العوامل التي تؤثر على فعالية المبادل وهي: عدد رينولدز(Reynolds number Re) ونسبة الموصلية الحرارية (thermal conductivity ratio K_r) والقطر المكافئ (hydraulic diameter D_h) وحجم القنوات. عند زيادة Re و D_h وحجم القنوات كل على حدة تقل الفعالية، وعند زيادة K_r تزداد الفعالية الى K_r =10 بعد هذه القيمة تصبح موصلية الجدار الفاصل مالا نهاية والتالي يكون غير مؤثر على الفعالية. كذلك تبين بأن هناك مجموعة من العوامل التي تؤثر على هبوط الضغط وهي: عدد رينولدز(Reynolds number Re) والقطر المكافئ (hydraulic diameter D_h) وحجم القنوات. عند زيادة Re يزداد هبوط الضغط وعند زيادة D_h وحجم القنوات كل على حدة يقل هبوط الضغط.

1. Introduction

The miniaturization of devices has become an increasingly common goal of researchers in recent years. This technique is most widely apparent in the increasing of transistors number per chip in the integrated circuits. The benefits of miniaturization are being realized in the many areas like, microbiology, medical, aerospace, optics, microelectronics and micro cooling devices (heat exchangers and heat sinks). This technology has provided many benefits including faster response time, high levels of system integration, high heat transfer rates and reduced cost [1]. Normally, microchannels can be defined as channels whose dimensions are less than 1mm and greater than 1µm. Above 1mm the flow exhibits behavior that is same as macroscopic flow. Below 1µm the flow is characterized as nanoscopic. Currently, most microchannels fall into the rang of 30µm to 300µm. Microchannels can be fabricated from many materials such glass, polymers, silicon and metals by using various tools and processes

including bulk micromachining, surface micromachining, laser techniques, molding, embossing and conventional machining with microcutters [2].

The ever-growing demand for functionality and performance in microprocessors cause continuous increase in the number of transistors integrated per chip and the operating frequency and decrease in feature size. For example, the Dual-Core Intel Itanium 2 processor, the new processor released by Intel, boasts over 1 billion transistors [3]. As a result, the total amount of heat generated is also increased tremendously over the past decades. It is of vital importance to dissipate the heat from the active circuits to the environment while maintaining an acceptable junction temperature in order to maintain the reliability and performance of the devices. However, microchannels, as the name suggest, are very fine channels of the width of a normal human hair widely used for electronic cooling. In microchannel heat exchanger, multiple microchannels are stacked together as shown in Figure(1).

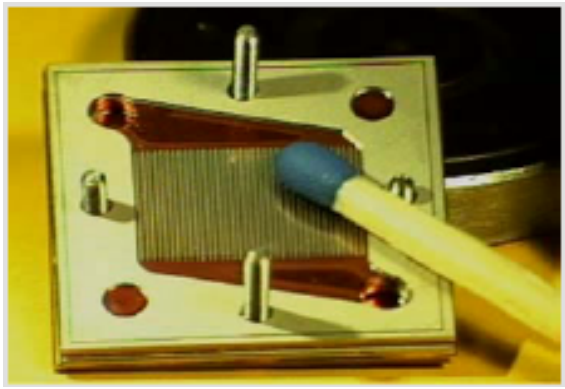

Figure (1). Sample of microchannels array as heat exchanger.

Using these microchannel heat exchangers heat fluxes as high as $1000 W/cm^2$ can be dissipated at relatively low surface temperatures [4]. However, compared with conventional heat exchangers, the main advantage of micro heat exchangers is their high heat transfer area per unit volume and hence the high overall heat transfer coefficient per unit volume [5]. Over the recent years ago, the scientists and researchers are focused on microchannels (heat sink and heat exchanger) due to their numerous applications as electronic cooling systems to provide effective ways to cover the development of electronic devices demands.

Muzychka [6]1999 developed an analytical and experimental study for the fluid friction and heat transfer for wide range of channels geometries. He showed that the square root of cross-section flow area as characteristic length provide better correlations for wide range of the ducts, than could be achieved by the hydraulic diameter.

Jiang et al. [7]2001 experimentally studied the fluid flow and forced convection heat transfer in rectangular micro heat exchanger. They concluded that the microchannel heat exchanger with deep channels has the best overall thermal-hydraulic performance.

Al-bakhit and Fakheri [8]2005 numerically investigated the parallel flow microchannel heat exchanger with rectangular ducts. They showed that using a high conductive material will not have an effect on increasing the heat exchanger effectiveness since the heat exchanger effectiveness will be independent of the wall thermal conductivity for K_r above 40. **Ashman and Kandlikar [9]2006** studied the types of manufacturing processes which currently being used in the fabrication of micro heat exchangers such as, Chemical Etching and micro machining. They concluded that the micro heat exchangers benefit is their high surface area to volume ratio and then high heat transfer.

Al-bakhit and Fakheri [10]2006 numerically investigated the parallel flow microchannel heat exchanger with rectangular ducts. They showed that the overall heat transfer coefficient is rapidly changing for $x/D_h Pe$ (Graetz number) below 0.03, and therefore the assumption of constant overall heat transfer coefficient is not valid if the Graetz number based on the heat exchanger length is of the order of 0.03. Also, the accurate results can be obtained by solving thermally developing energy equation using fully developed velocity profiles.

Nirm et al. [11]2009 numerically investigated the hydrodynamics and thermal behaviors of the laminar, 2-D, fully developed, slip flow inside an insolated parallel-plate microchannel heat exchanger. They showed that both the velocity slip and the temperature jump at the walls increase with increasing Knudsen number.

Accurate prediction of temperature distribution in both the solids and fluids in these systems is of critical importance for a fundamental understanding of the physics governing of the thermal and fluid flow processes and for practical system design and optimization [12]. Many authors are investigated circular microchannels and non-circular microchannels such as rectangular, trapezoidal, elliptical and triangular. All these works are aimed to obtain the best applicable microchannel geometry, this means high heat transfer rate and low pressure drop. However, there are nearly negligible numerical researches concern flow and heat transfers in the isosceles right triangular microchannel heat exchanger. On other hand, the available results concerns flow and heat transfer characteristics in that exchanger is not cleared, therefore the present study is aimed to investigate the main points: Obtain a numerical model for hydrodynamics and heat transfer in isosceles right triangular microchannel heat exchanger by solving the continuity, momentum and energy equations and overcome the complexity in that heat exchanger. And study of hydrodynamics and heat transfer characteristics in the

isosceles right triangular microchannel heat exchanger and obtaining the controlling parameters on these characteristics.

2. Analysis

Schematic structure of a parallel flow microchannel heat exchanger under concentration is shown in Figure 2a. Due to symmetry between channels rows, the individual heat exchange unit under consentration which consists of two channels (hot and cold) and a separating wall as shown in Figure 2b. In this figure, the hot fluid enters the lower duct with a uniform velocity $u_{h,in}$ and uniform temperature, $T_{h,in}$ while the cold fluid enters the upper duct at $u_{c,in}$ and $T_{c,in}$. Heat is transferred from the hot fluid to cold fluid through the inclined wall (solid) of thickness t_s. Also, In this configuration, two corners are chamfered to facilitate the numerical solution. On other hand, this is not affected on the computations. Moreover the solid is inclined by angle 45^o, this will increase the area of heat transfer comparatively with rectangular channel for same dimensions.

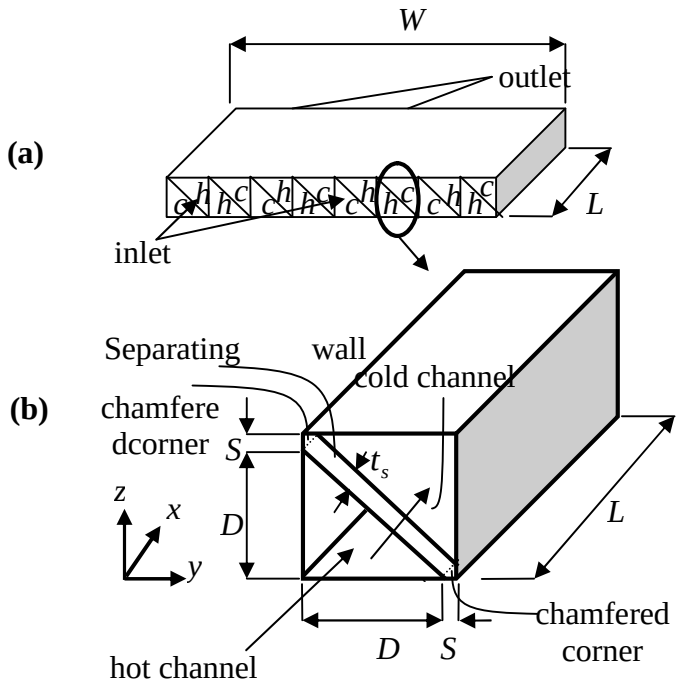

Figure (2). Schematic of parallel flow microchannel heat exchanger.

However, the governing equations for the present model are based on the following physical and geometrical assumptions:

- The flow is laminar and steady.
- The Knudsen number is small enough so that, the fluid is a continuous medium (no slip).
- The fluids are incompressible, Newtonian fluids with constant properties; in this case the water is used as working fluid.
- There is no heat transfer to/from the ambient medium.
- The energy dissipation is negligible.
- The pressure gradient is in axial direction only.
- Three dimensional of the flow and heat transfer.

The dimensionless form of the governing equations and its boundary conditions is aachieved based on the following dimensionless parameters:

$$x^* = \frac{x}{D_h}\ ,\quad y^* = \frac{y}{D_h}\ ,\quad z^* = \frac{z}{D_h}\ ,\ t_s^* = \frac{t_s}{D_h}\ ,\quad u_i^* = \frac{u_i}{u_{h,in}},\ v_i^* = \frac{v_i}{u_{h,in}}\ ,\ w_i^* = \frac{w_i}{u_{h,in}},\ p_i^* = \frac{p_i}{\rho u_{h,in}^2}$$

$$,\ T_i^* = \frac{T_i - T_{c,in}}{T_{h,in} - T_{c,in}} and\ \ T_s^* = \frac{T_s - T_{c,in}}{T_{h,in} - T_{c,in}}$$

therefore, the dimensionless governing equations are:

x-momentum equation

$$u_i^* \frac{\partial u_i^*}{\partial x^*} + v_i^* \frac{\partial u_i^*}{\partial y^*} + w_i^* \frac{\partial u_i^*}{\partial z^*} = -\frac{dp_i^*}{dx^*} + \frac{1}{Re_i}\left(\frac{\partial^2 u_i^*}{\partial x^{*2}} + \frac{\partial^2 u_i^*}{\partial y^{*2}} + \frac{\partial^2 u_i^*}{\partial z^{*2}}\right) \quad (1)$$

y-momentum equation

$$u_i^* \frac{\partial v_i^*}{\partial x^*} + v_i^* \frac{\partial v_i^*}{\partial y^*} + w_i^* \frac{\partial v_i^*}{\partial z^*} = \frac{1}{Re_i}\left(\frac{\partial^2 v_i^*}{\partial x^{*2}} + \frac{\partial^2 v_i^*}{\partial y^{*2}} + \frac{\partial^2 v_i^*}{\partial z^{*2}}\right) \quad (2)$$

z-momentum equation

$$u_i^* \frac{\partial w_i^*}{\partial x^*} + v_i^* \frac{\partial w_i^*}{\partial y^*} + w_i^* \frac{\partial w_i^*}{\partial z^*} = \frac{1}{Re_i}\left(\frac{\partial^2 w_i^*}{\partial x^{*2}} + \frac{\partial^2 w_i^*}{\partial y^{*2}} + \frac{\partial^2 w_i^*}{\partial z^{*2}}\right) \quad (3)$$

where $\mathrm{Re}_i = \dfrac{\rho_i u_{h,in} D_h}{\mu_i}$

continuity equation

$$\frac{\partial u_i^*}{\partial x^*} + \frac{\partial v_i^*}{\partial y^*} + \frac{\partial w_i^*}{\partial z^*} = 0 \quad (4)$$

energy equation for fluid

$$u_i^* \frac{\partial T_i^*}{\partial x^*} + v_i^* \frac{\partial T_i^*}{\partial y^*} + w_i^* \frac{\partial T_i^*}{\partial z^*} = \frac{1}{Pe_i}\left(\frac{\partial^2 T_i^*}{\partial x^{*2}} + \frac{\partial^2 T_i^*}{\partial y^{*2}} + \frac{\partial^2 T_i^*}{\partial z^{*2}}\right) \quad (5)$$

where the subscript *i* is represent *h* or *c* which refer to the lower and upper (hot and cold) channels respectively.

The diffusion equation for solid becomes

$$\frac{\partial^2 T_s^*}{\partial x^{*2}} + \frac{\partial^2 T_s^*}{\partial y^{*2}} + \frac{\partial^2 T_s^*}{\partial z^{*2}} = 0 \quad (6)$$

The dimensionless boundary conditions are:

- Lower channel (hot channel)

$$x^* = 0 \qquad u^* = 1, v^* = w^* = 0 \quad and \quad T_h^* = 1 \quad (7)$$

$$x^* = L^* = \frac{L}{D_h} \qquad \frac{\partial u^*}{\partial x^*} = \frac{\partial v^*}{\partial x^*} = \frac{\partial w^*}{\partial x^*} = 0 \quad and \quad \frac{\partial T_h^*}{\partial x^*} = 0 \quad (8)$$

$$y^* = 0,\ 0 \le z^* \le D^* \qquad u^* = v^* = w^* = 0 \quad and \quad \frac{\partial T_h^*}{\partial y^*} = 0 \quad (9)$$

$$z^* = 0,\ 0 \le y^* \le D^* \qquad u^* = v^* = w^* = 0 \quad and \quad \frac{\partial T_h^*}{\partial z^*} = 0 \quad (10)$$

and the boundary conditions along the inclined wall ($z = D - y$) are:

$$u^* = v^* = w^* = 0, \frac{\partial T_h^*}{\partial n^*} = \frac{k_s}{k_h}\frac{\partial T_s^*}{\partial n^*} \quad and \quad T_h^* = T_s^* \quad (11)$$

- Upper channel (cold channel)

$$x^* = 0 \qquad u^* = \frac{u_{c,in}}{u_{h,in}}, v^* = w^* = 0 \qquad T_c^* = 0 \quad (12)$$

$$x^* = L^* = \frac{L}{D_h} \qquad \frac{\partial u^*}{\partial x^*} = \frac{\partial v^*}{\partial x^*} = \frac{\partial w^*}{\partial x^*} = 0 \quad and \quad \frac{\partial T_c^*}{\partial x^*} = 0 \quad (13)$$

$$y^* = D^* + S^* = \frac{D+S}{D_h},\ S^* \le z^* \le S^* + D^* \qquad u^* = v^* = w^* = 0 \quad and \quad \frac{\partial T_c^*}{\partial y^*} = 0 \quad (14)$$

$$z^* = D^* + S^* = \frac{D+S}{D_h},\ S^* \le y^* \le S^* + D^* \qquad u^* = v^* = w^* = 0 \quad and \quad \frac{\partial T_c^*}{\partial z^*} = 0 \quad (15)$$

also, the boundary conditions along the inclined wall ($z = D + 2S - y$) are

$$u^* = v^* = w^* = 0 \quad \frac{\partial T_c^*}{\partial n^*} = \frac{k_s}{k_c}\frac{\partial T_s^*}{\partial n^*} \quad and \quad T_c^* = T_s^* \quad (16)$$

- Separated wall (solid)

$$x^* = 0 \qquad \frac{\partial T_s^*}{\partial x^*} = 0 \quad (17)$$

$$x^* = L^* = \frac{L}{D_h} \qquad \frac{\partial T_s^*}{\partial x^*} = 0 \quad (18)$$

$$z^* = y^* + D^* \qquad \frac{\partial T_s^*}{\partial m^*} = 0 \tag{19}$$

$$z^* = y^* - D^* \qquad \frac{\partial T_s^*}{\partial m^*} = 0 \tag{20}$$

Where

$$D^* = \frac{D}{D_h}, m^* = \frac{m}{D_h}, n^* = \frac{n}{D_h} \text{ and } S^* = \frac{S}{D_h}$$

The boundary conditions in equations (19) and (20) represents the boundary conditions at the chamfered corners. And between solid and hot liquid ($z = D - y$)

$$\frac{\partial T_h^*}{\partial n^*} = \frac{k_s}{k_h}\frac{\partial T_s^*}{\partial n^*} \quad and \quad T_h^* = T_s^* \tag{21}$$

also, between solid and cold liquid ($z = D + 2S - y$)

$$\frac{\partial T_c^*}{\partial n^*} = \frac{k_s}{k_c}\frac{\partial T_s^*}{\partial n^*} \quad and \quad T_c^* = T_s^* \tag{22}$$

After establishing the governing equations and boundary conditions, the finite-volume method with FORTRAN code will be used to obtain numerical solution for the problem. At this situation, the velocity and pressure fields for two channels and temperature distribution for hot liquid T_h^*, solid T_s^* and cold liquid T_c^* are obtained. Now, the performance parameters such the effectiveness ε will be estimated which is the ratio of actual heat transfer to the maximum possible heat that can be transferred and given by [13]:

$$\varepsilon = q_{actual} / q_{\max.\ possible} \tag{23}$$

$$q_{actual} = m_c^{\cdot} c_c \left(T_{c,out} - T_{c,in}\right) = m_h^{\cdot} c_h \left(T_{h,in} - T_{h,out}\right) \tag{24}$$

For convenience, the rates and specific heats are lumped together the flow and term the products the capacity rates

$$C_c = m^{\cdot}{}_c c_c \text{ and } C_h = m^{\cdot} c_h \tag{25}$$

Now, if $C_h < C_c$, this means the

$$q_{\max} = C_h \left(T_{h,in} - T_{c,in}\right) \tag{26}$$

otherwise

$$q_{\max} = C_c \left(T_{h,in} - T_{c,in}\right) \tag{27}$$

thus

$$q_{\max} = C_{\min} \left(T_{h,in} - T_{c,in}\right) \tag{28}$$

then the effectiveness is

$$\varepsilon = \frac{C_c\left(T_{c,out} - T_{c,in}\right)}{C_{\min}\left(T_{h,in} - T_{c,in}\right)} = \frac{C_h\left(T_{h,in} - T_{h,out}\right)}{C_{\min}\left(T_{h,in} - T_{c,in}\right)} \quad (29)$$

3. Numerical solution

Finite volume method was used to convert the governing equations to algebraic form accomplished using an upwind differencing scheme on a staggered which used to solve pressure-velocity coupling (pressure-correction method). The SIMPLE algorithm was used to solve the problem as published in [14] where, the velocity and pressure fields are estimated in each channel separately because no coupling between the channels for these variables, and then the temperatures for hot fluid, separated wall and cold fluid are achieved simultaneously [15].

4. Results and discussion

In this section the hydrodynamics and heat transfer characteristics in parallel flow microchannel heat exchanger with isosceles right triangular ducts are presented. The effects of various parameters on the performance of the heat exchanger will be introduced. The main parameters characterize the flow and heat transfer are: pressure drop Δp along the length of micro heat exchanger, dimensionless velocity u^*, dimensionless mean temperature T_m^* for hot and cold fluid, dimensionless mean temperature $T_{s_m}^*$ for solid, convective heat transfer coefficients for hot and cold fluid h_h and h_c, dimensionless overall heat transfer coefficient UD_h/k_w and microchannel heat exchanger effectiveness ε. The properties are taken at average temperature $T_{average}$, where $T_{average} = \left(T_{h,in} + T_{c,in}\right)/2$.

The numerical results are presented for the microchannel heat exchanger with rectangular ducts in the figures, 3 and 4 for verification of the developed numerical model, which was developed basically for isosceles right triangular microchannel heat exchanger. Numerical solution of continuity, momentum and energy equations for parallel flow rectangular microchannel heat exchanger is achieved for verification of the numerical program. The verification is achieved as the following: the calculations are carried out by present FORTRAN program for rectangular microchannel heat exchanger and the results compared with the analytical results of Muzychka [6] and numerical results of Al-bakhit and Fakheri [10].

Figure (3). shows a comparison for the apparent friction constant $f_{app}\,\mathrm{Re}_{\sqrt{A_f}}$, where Reynolds number is based upon square root of flow area $\sqrt{A_f}$, this means the characteristic length is $\sqrt{A_f}$ in rectangular channel against the dimensionless axial distance $x^{-}_{\sqrt{A_f}} = \dfrac{x}{\sqrt{A_f}\,\mathrm{Re}_{\sqrt{A_f}}}$ at Re=50 and $\sqrt{A_f}$=100μm. The figure shows that the $f_{app}\,\mathrm{Re}_{\sqrt{A_f}}$ for both the numerical and analytical models is higher at entrance region and decrease towards exit with nearby constant value, and the numerical results gives a good agreement with analytical results of Muzychka [6] and the maximum percentage error was ±4.95%.

Figure 4. illustrates a comparison for the dimensionless mean temperature T_m^* for the hot and cold fluid in rectangular microchannel heat exchanger against the dimensionless axial distance x^+ at Re=100, Pr=0.7 and $\dfrac{k_w D_h}{k_s t_s}$=100. The figure indicates the numerical results gives a good agreement with numerical results of Al-bakhit and Fakheri [10] and the maximum percentage error was ±2.01%.

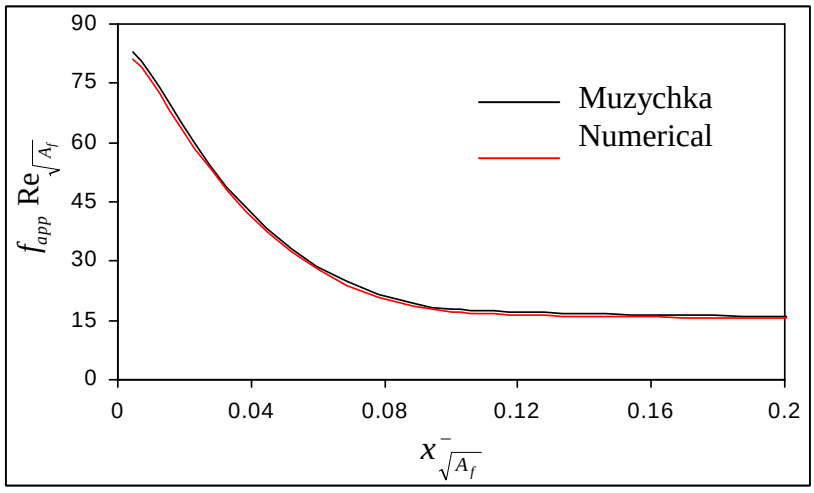

Figure (3). Comparison of the apparent friction constant.

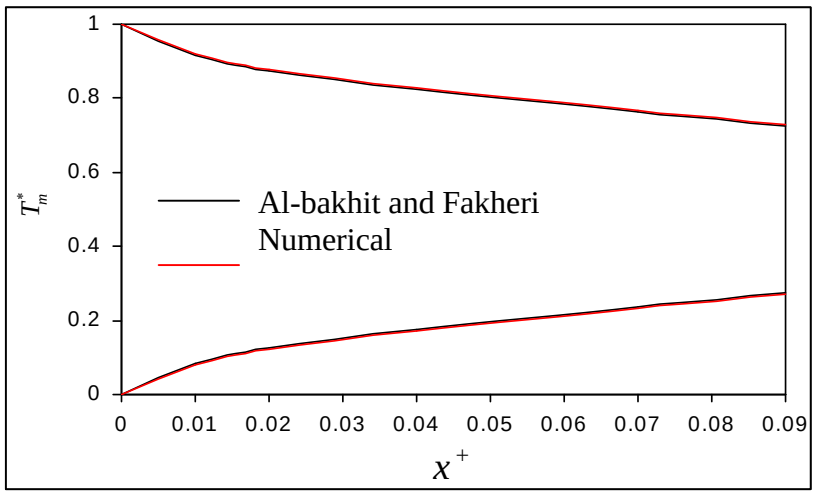

Figure (4). Comparison of the dimensionless mean temperature of the hot and cold fluid.

Figure (5). illustrates the variation of the dimensionless centerline velocity profile u^* with dimensionless axial distance x^* for different Reynolds number at D_h =117μm. The figure clarify that the velocity profile is varied with Reynolds number, also indicate that the entrance length increase with Re. Once the fully developed region is reached the velocity profile becomes constant [16].

Figure (6). shows the longitudinal variation of pressure drop Δp with dimensionless axial distance x^* for different Reynolds numbers at D_h =117μm. The figure clarify that pressure drop Δp increases with Reynolds number especially at high Reynolds number (Re=200). This because the mass flow rate increase with Re and pressure drop that required to force the fluid through the channel increase.

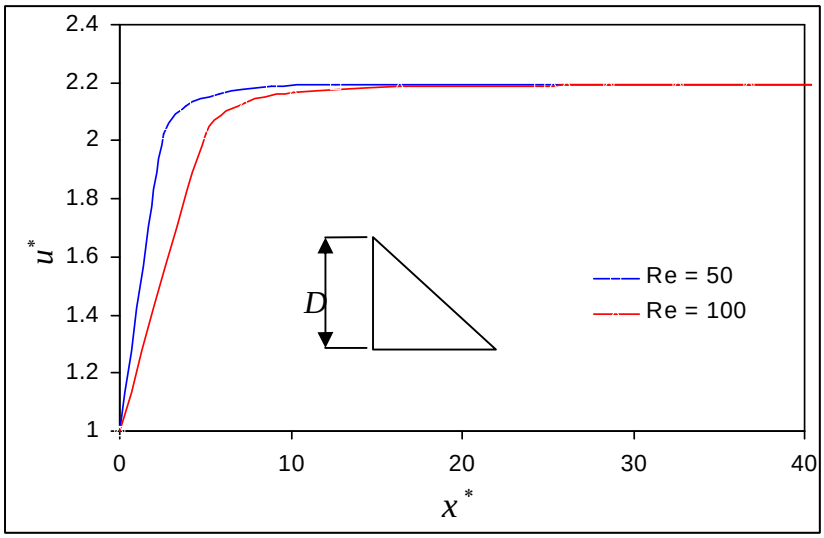

Figure (5). Variation of the dimensionless centerline velocity profile for different Reynolds numbers.

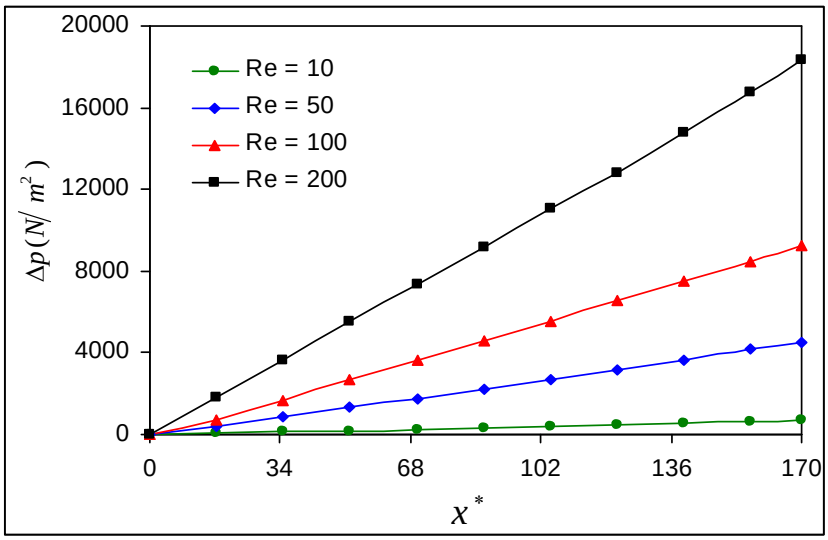

Figure 6. Longitudinal variation of the pressure drop for different Reynolds numbers.

Consider $2*10^{-8}m^3$ microchannel heat exchanger volume contains number of channels, if number of channels increase, the channel volume decreases. Figure 7. represents the variation of pressure drop Δp with number of channels, and the exchanger volume is $2*10^{-8}m^3$. For each Re, the figure clarifies that pressure drop Δp increases with number of channels. When channel volume decrease, the flow area decrease and then the hydraulic diameter decrease.

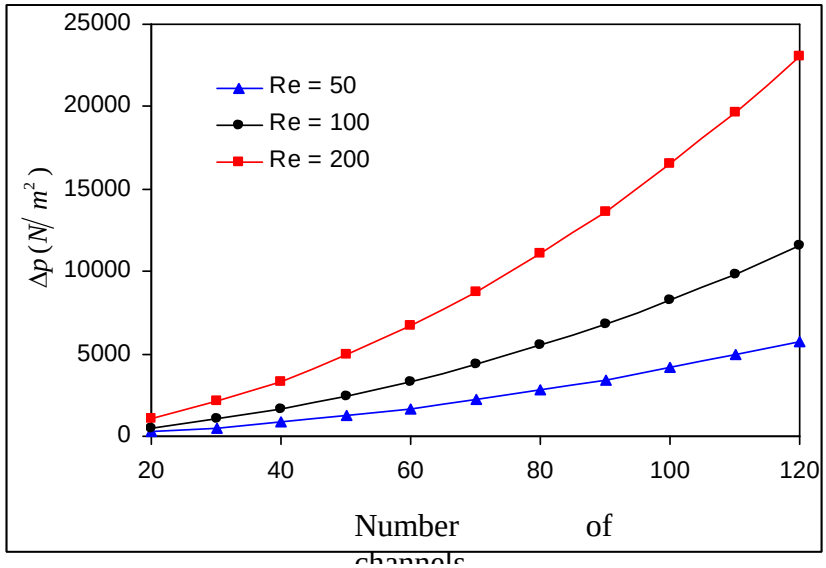

Figure 7. Variation of the pressure drop through the heat exchanger with number of channels.

Figure (8). represents the longitudinal variation of the dimensionless mean temperature T_m^* of the hot and cold fluid with dimensionless axial distance x^* for different Reynolds numbers at K_r=1, D_h=117μm and t_s=50μm. As can be seen the dimensionless mean temperature T_m^* diverge to each other when Re is high and vice versa. At high Re the velocity of fluid increase and then the outlet temperatures is nearest to inlet temperatures.

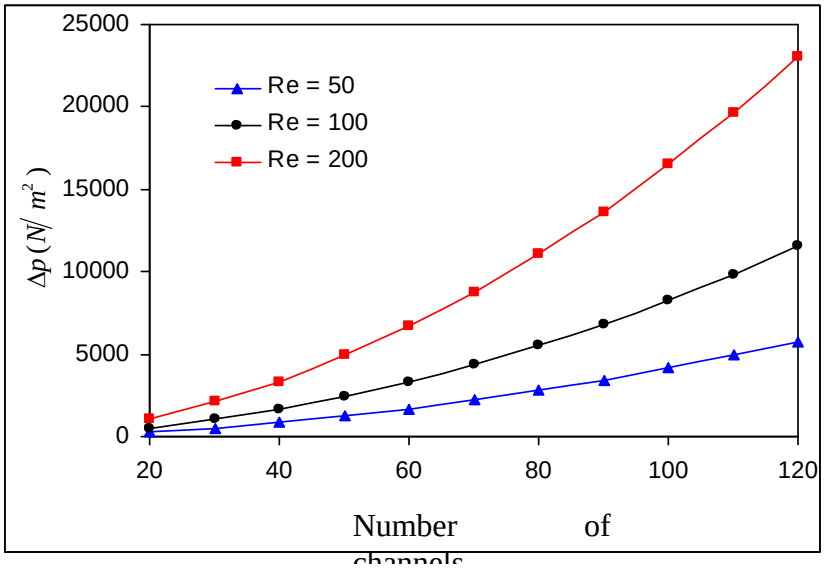

Figure (8). Longitudinal variation of the hot and cold fluid dimensionless mean temperature for different Reynolds numbers.

Figure (9). illustrates the longitudinal variation of the dimensionless mean temperature T_m^* of the hot and cold fluid with dimensionless axial distance x^* for different thermal conductivity ratios at Re=200, D_h =117μm and t_s =50μm. The figure shows that the T_m^* converge to each other and the difference between inlet and outlet temperatures increase with K_r up to a certain limit K_r=10. After this value the T_m^* remain constant for same x^*. The numerical results of Al-bakhit and Fakheri [8] for parallel flow rectangular microchannel heat exchanger showed that more heat is transferred as the thermal conductivity ratio is increased up to K_r=40, after which increasing the thermal conductivity will not enhance the heat transfer. They showed that this is because, the wall will behaves as an infinitely conducting wall with negligible temperature gradient, and the heat transfer between the two fluids will be independent of the wall properties, depending only on the fluids conditions and heat exchanger geometry. The difference between the numerical results of Al-bakhit and Fakheri [8] and present results is due to the different in geometry. However, for same conditions, the Figure (10). may explain this behavior. As can be seen the dimensionless mean solid

temperature $T^*_{s_m}$ is varied with fluid temperature up to K_r=10. After this value the $T^*_{s_m}$ is independent of fluid temperature and seems as straight line. This means the wall will be not affected on the fluid temperature after K_r=10.

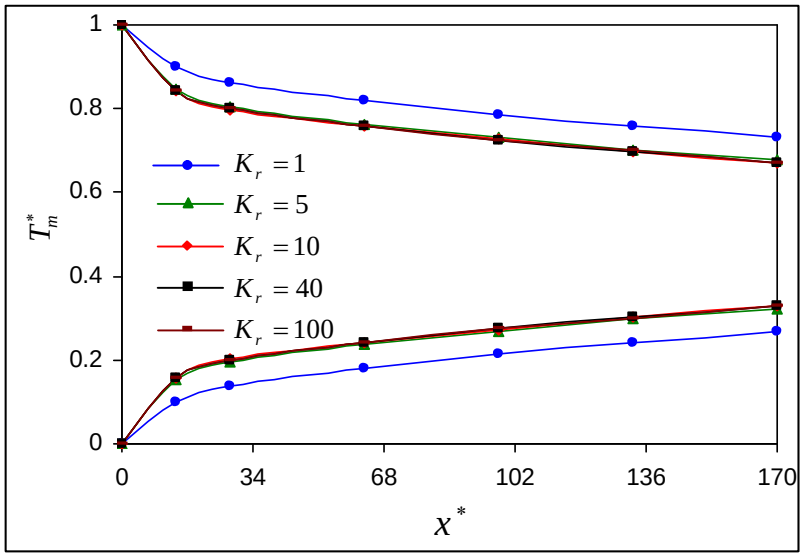

Figure (9). Longitudinal variation of the hot and cold fluid dimensionless mean temperature for different thermal conductivity ratios.

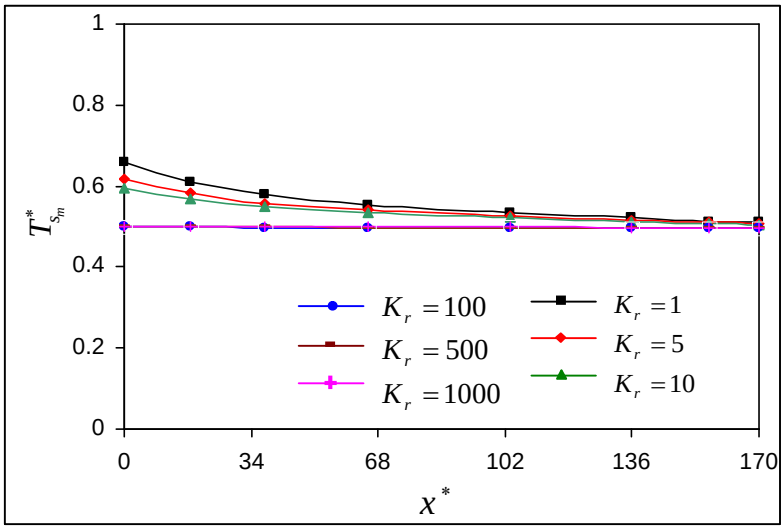

Figure (10). Longitudinal variation of the solid dimensionless mean temperature for different thermal conductivity ratios.

Figure (11). shows the longitudinal variation of the dimensionless mean temperature T^*_m of the hot and cold fluid with axial distance *x* for different hydraulic diameters at Re=100, K_r

=1 and t_s =50μm. The figure clarifies that the T_m^* is converge to each other when the hydraulic diameter decrease. This is because, when the hydraulic diameter decreases, the amount of fluid decrease and then the difference between inlet and outlet temperatures increase.

Figure (12). clarifies the longitudinal variation of T_m^* with axial distance x for different channels numbers at Re=100, K_r=1, t_s =50μm and exchanger volume is $2*10^{-8} m^3$. The figure shows that the T_m^* is to converge to each other when number of channels increase and vice versa. This is because, when the number of channels increases, the flow area decreases, this leads to the amount of fluid decrease and then the difference increase.

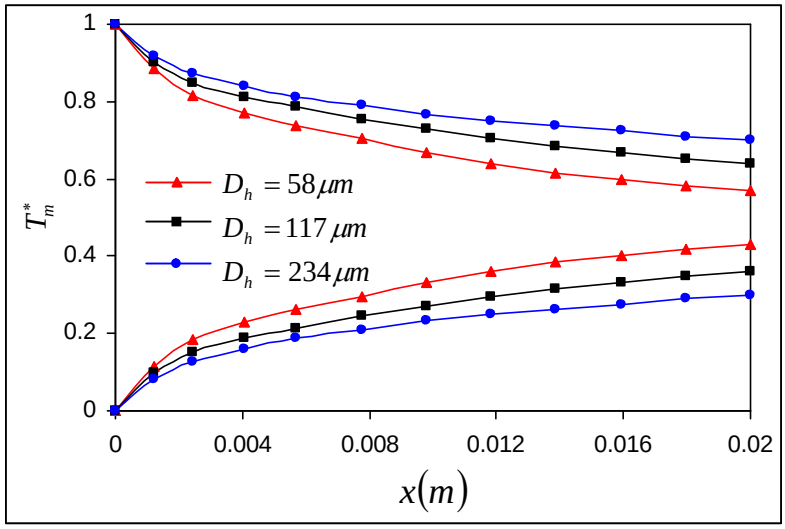

Figure (11). Longitudinal variation of the hot and cold fluid dimensionless mean temperature for different hydraulic diameters.

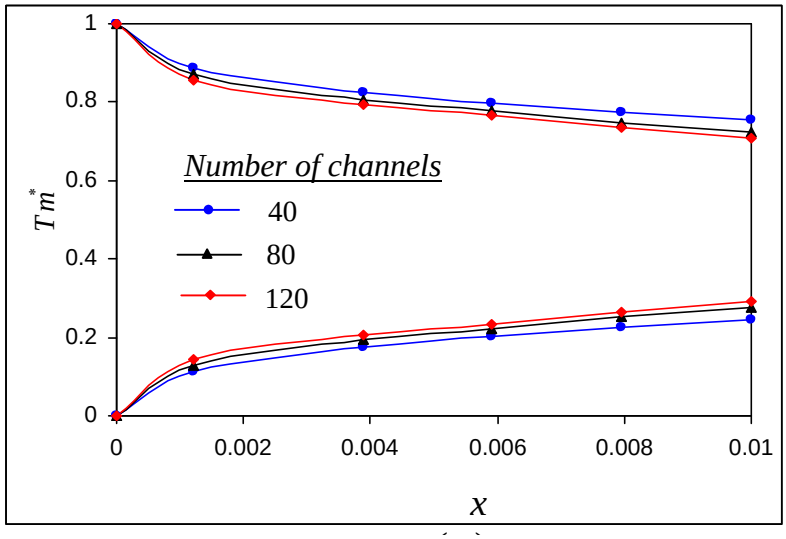

Figure 12. Longitudinal variation of the hot and cold fluid dimensionless mean temperature for different channels numbers.

Figure (13). represents the longitudinal variation of the convective heat transfer coefficients, h_h and h_c for both fluids with dimensionless axial distance x^* at K_r=1 D_h =117μm and t_s =50μm for different Reynolds numbers. As can be seen at the entrance region (initial part of channel) leads to high values of h_h and h_c due to high temperature gradient and small boundary layer. Also, h_h and h_c increase with Re because increase the mass flow rate (velocity) with increasing Re, also the figure shows for each Re the h_h and h_c are not equal this because the axial heat conduction in the separated wall (solid), which is large in the entrance region.

Figure (14). clarifies the longitudinal variation of the dimensionless overall heat transfer coefficient UD_h/k_w with dimensionless axial distance x^* at K_r=5, D_h =117μm, Re=200 and t_s =50μm. Notice that in the entrance region, the developing flow leads to high values of the UD_h/k_w and then decrease towards fully developed flow.

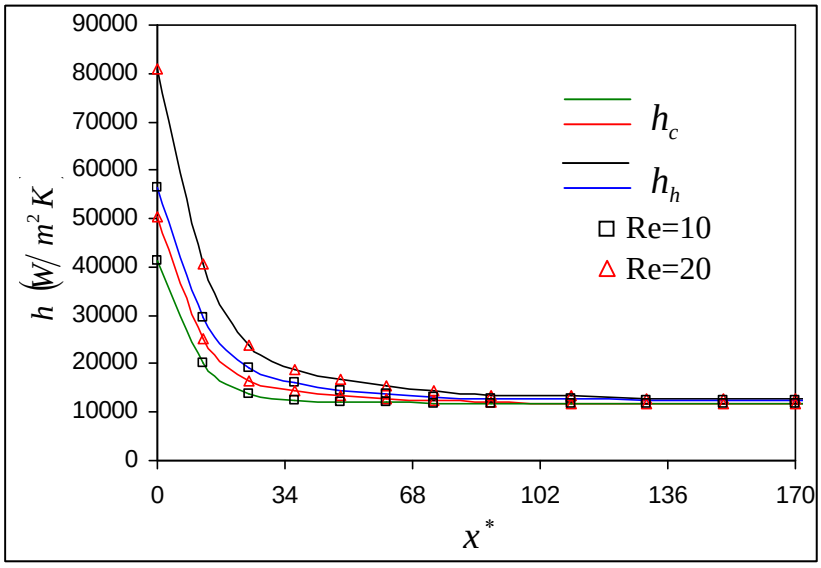

Figure 13. Longitudinal variations of the convective heat transfer coefficients for hot and cold fluid for different Reynolds numbers.

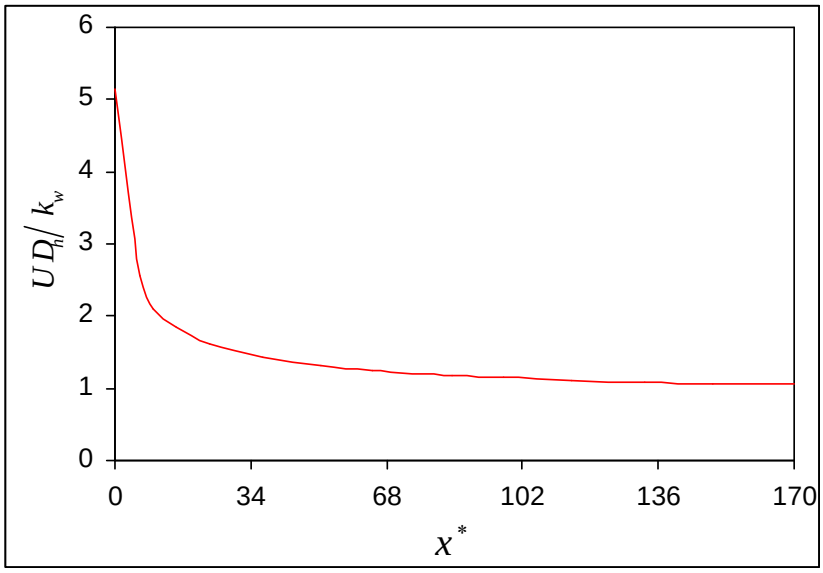

Figure (14). Longitudinal variation of the dimensionless overall heat transfer coefficient.

Figure (15). shows the variation of the microchannel heat exchanger effectiveness ε with Reynolds number Re at K_r=1, D_h =117μm, L=1cm and t_s =50μm. The figure clarifies that the effectiveness decreases with increasing Re. This is because the amount of fluid increase with Re and then ΔT decrease.

Figure (16). represents the variation of the microchannel heat exchanger effectiveness ε with thermal conductivity ratio K_r at Re=100, D_h =117μm, L=1cm and t_s =50μm. The figure indicates that the effectiveness increase with thermal conductivity ratio up to K_r=10. After this value the effectiveness remains constant. This is because the temperature is independent of K_r after 10.

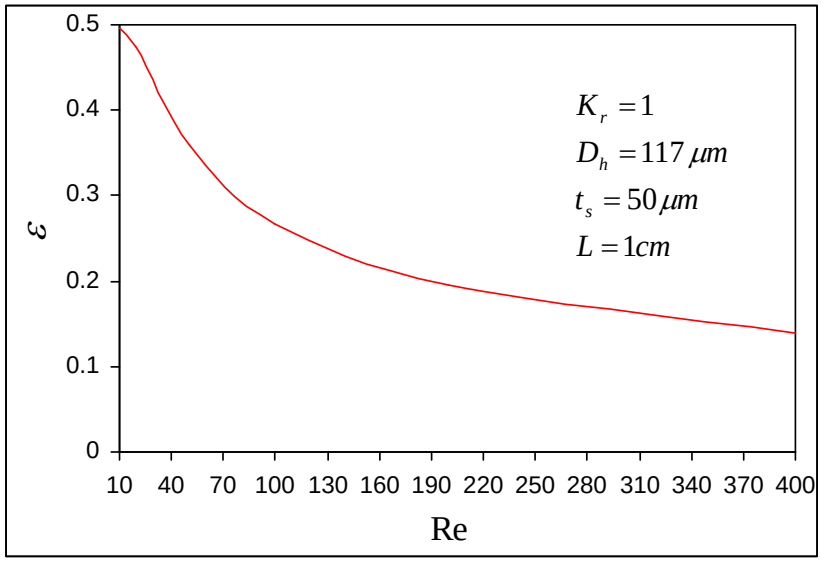

Figure (15). Variation of the microchannel heat exchanger effectiveness with Reynolds number.

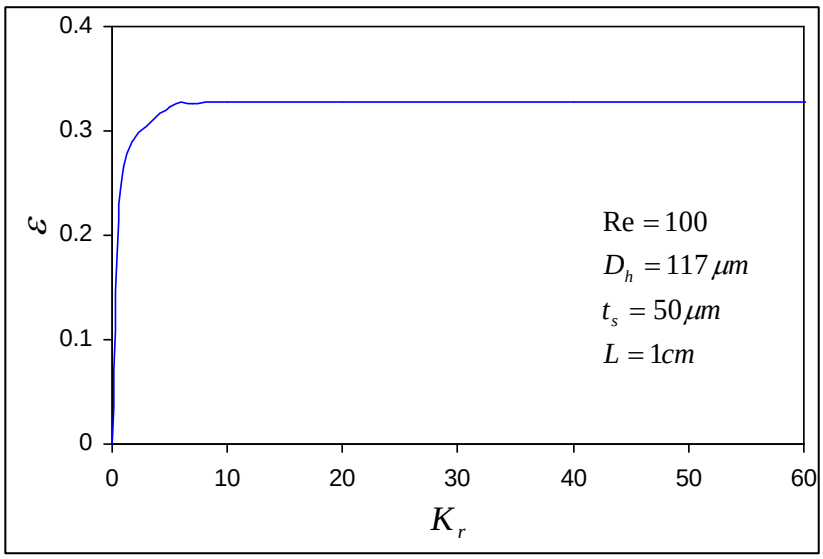

Figure (16). Variation of the microchannel heat exchanger effectiveness with thermal conductivity ratio.

Figure (17). illustrates the variation of the microchannel heat exchanger effectiveness ε with number of channels, and exchanger volume is $2*10^{-8}m^3$ at K_r=1 and t_s=50μm. For each Re, the figure clarifies that the effectiveness increases with number of channels. This is because the amount fluid decreases when the channel volume decrease and then ΔT increase. Also, the figure shows that the effectiveness at Re=50 is larger than that at Re=100 and 200, this because the velocity of fluid increase with Re and then ΔT decrease.

Figure (18). shows the variation of the microchannel heat exchanger effectiveness ε with number of channels, and exchanger volume is $2*10^{-8}m^3$ at Re=100 and t_s=50μm. For each K_r, the figure clarifies that the effectiveness increases with number of channels. This is because the amount of fluid decreases when the channel volume decrease and then ΔT increase. Also, the figure indicates that the effectiveness at K_r=10 is larger than that at K_r=1 and 5, this because the ΔT increase with K_r.

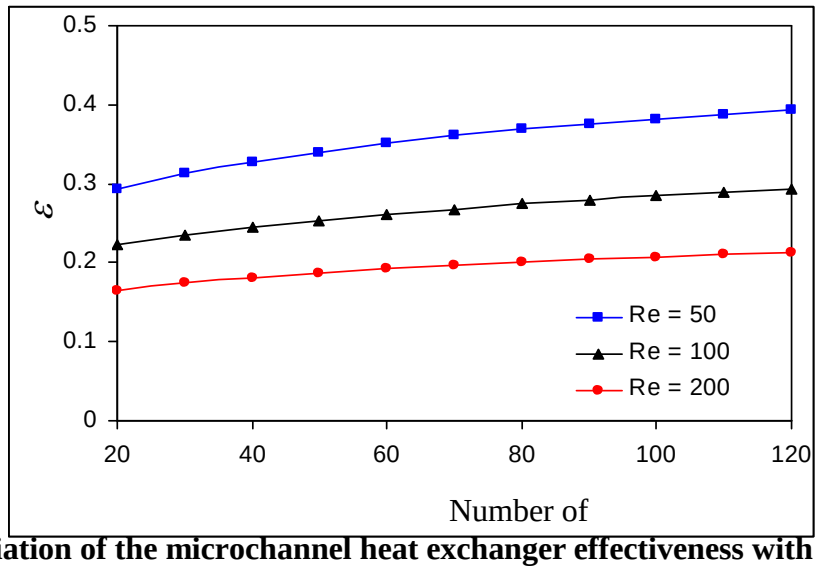

Figure 17. Variation of the microchannel heat exchanger effectiveness with number of channels.

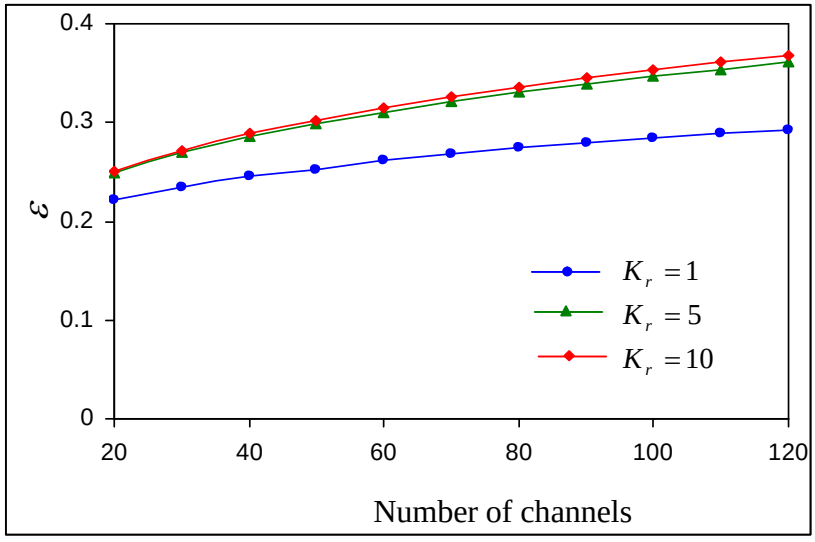

Figure 18. Variation of the microchannel heat exchanger effectiveness with number of channels.

The performance index will be discussed through the effectiveness to pressure drop ratio $\varepsilon/\Delta p$. When this parameter increase, this means either the effectiveness increase or pressure drop decrease and both cases are desired. Figure 19. indicates the variation of the microchannel heat exchanger effectiveness to pressure drop ratio $\varepsilon/\Delta p$ with number of channels, and exchanger volume is $2*10^{-8} m^3$ at K_r=1 and t_s =50μm. For each Re, the figure clarifies that $\varepsilon/\Delta p$ ratio decrease with number of channels. This because pressure drop increase with number of channels.

Figure 20. clarifies the variation of the microchannel heat exchanger effectiveness ε to pressure drop ratio $\varepsilon/\Delta p$ with number of channels, and exchanger volume is $2*10^{-8} m^3$ at Re=100 and t_s =50μm. For each K_r, the figure shows that $\varepsilon/\Delta p$ ratio decrease with number of channels. This because pressure drop increase with number of channels. Also, the figure indicates that $\varepsilon/\Delta p$ ratio increase with K_r, this because the effectiveness increase with K_r.

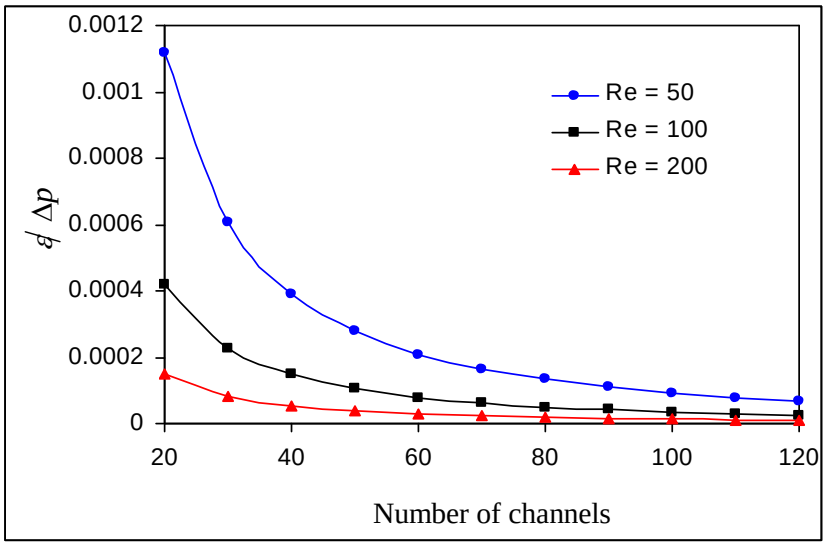

Figure (19). Variation of the microchannel heat exchanger effectiveness to pressure drop ratio with number of channels.

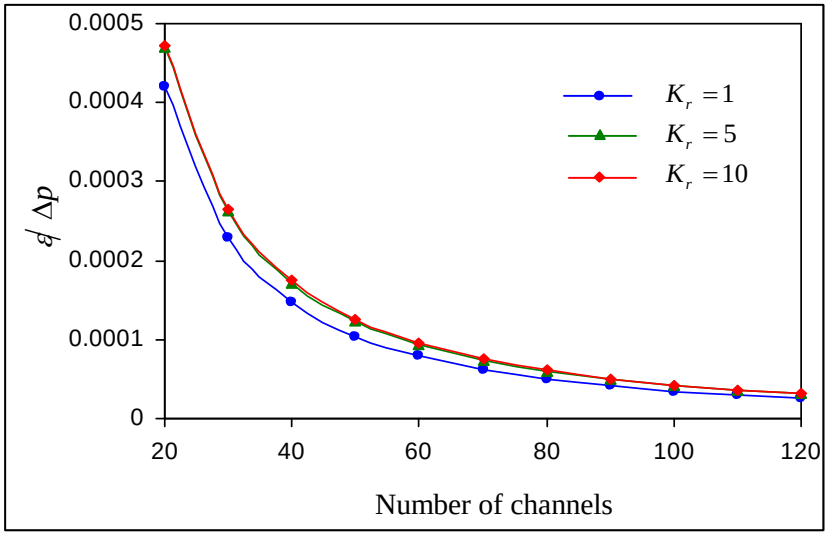

Figure (20). Variation of the microchannel heat exchanger effectiveness to pressure drop ratio with number of channels.

5. Conclusions

From the present work it can be concluded the following remarks:

- The flow in the isosceles right triangular microchannels heat exchanger is studied and the obtained effecting parameters that control the flow and heat transfer are the thermal conductivity ratio K_r, Reynolds number Re, hydraulic diameter D_h and channel volume.

  Thermal conductivity ratio K_r plays a significant role on the heat transfer characteristics, this reflected in the effectiveness ε, where the ε increase with K_r up to K_r =10. After this value the wall will behaves as infinity conducting wall with negligible temperature gradient (becomes not affected on the heat transfer characteristics).
- There is an important role of Reynolds number Re on the heat transfer and hydrodynamics characteristics, this reflected in the effectiveness ε, pressure drop Δ*p*, dimensionless velocity u^* and convective heat transfer coefficients h_h and h_c.
- The hydraulic diameter D_h effect on the heat transfer and hydrodynamics characteristics, this reflected in the effectiveness ε and pressure drop Δ*p*.
- Channel volume effect on the heat transfer and hydrodynamics characteristics, this reflected in the effectiveness ε and pressure drop Δ*p*.

6. References

[1] **Michael Kohl,** "An Experimental Investigation of Microchannel Flow with Internal Pressure Measurements", PhD Thesis, Georgia Institute of Technology, May (2004).

[2] **Amit S. Kulkarni,** "Effects of Surface Roughness in Microchannel Flows", MSc Thesis, University of Florida, (2004).

[3] **Carter Reynolds Dietz,** "Single-Phase Forced Convection in A microchannel with Carbon Nanotubes for Electronic Cooling Applications", MSc Thesis, Georgia Institute of Technology, August (2007).

[4] **Pritish Ranjan Parida,** "Experimental Investigation of Heat Transfer Rate in Microchannels", MSc Thesis, B. Tech., Indian Institute of Technology Guwahati 2006, December (2007).

[5] **Ionel Olaru and Radu Caliman,** "A cross Flow Micro Heat Exchanger Design", MOCM 12, Romanian Technical Sciences Academy, Vol. 1, (2006).

[6] **Yuri Stephan Muzychka,** "Analytical and Experimental Study of Fluid Friction and Heat Transfer in Low Reynolds Number Flow Heat Exchangers", PhD Thesis, Waterloo, Ontario, Canada, (1999).

[7] **Pei-Xue Jiang, Ming-Hong Fan, Guang-Shu Si and Ze-Pei Ren,** "Thermal-hydraulic Performance of Small Scale Microchannel and Porous-media Heat Exchangers", International Journal of Heat and Mass Transfer, Vol. 44, pp. 1039-1051, (2001).

[8] **Hussien Al-bakhit and Ahmad Fakheri,** "Entrance and Wall Conduction Effects in Parallel Flow Heat Exchangers", Proceedings of Fifth Internal Conference on Enhanced, Compact and Ultra-Compact Heat Exchangers: Science, Engineering and Technology, Eds. R. K. Shah, M. Ishizuka, T. M. Rudy and V. V. Wadekar, Engineering Conferences International, Hoboken, NJ, USA, September (2005).

[9] **Sean Ashman and Satish G. Kandlikar,** "Numerical Methods for Heat & Fluid flow", Vol. 12, No. 1, pp. 81-99, (2002).

[10] **Hussien Al-bakhit and Ahmad Fakheri,** "Numerical Simulation of Heat Transfer in Simultaneously Developing Flows in Parallel Rectangular Ducts", Applied Thermal Engineering, Vol. 26, pp. 596-603, (2006).

[11] **M. A. Al-Nirm, M. Maqableh, A. F. Khadrawi and S. A. Ammourah,** "Fully Developed Thermal Behaviors for Parallel Flow Microchannel Heat Exchanger", International Communications in Heat and Mass Transfer, Vol. 36, pp. 385-390, (2009).

[12] **W. Song and B. Q. Li,** "Finite Element Solution of Conjugate Heat Transfer Problems with and without the Use of Gap Elements", International Journal of

[13] **David P. Kessler and Robert A. Greenkorn,** "Momentum, Heat, and Mass Transfer Fundamentals", Marcel Dekker, (1999).

[14] **H. K. Versteeg and W. Malalasekera,** "An introduction to Computational Fluid Dynamics-The Finite-Volume Method", Longman, (1995).

[15] **Hussien Al-bakhit and Ahmad Fakheri,** "A hybrid Approach for Full Numerical Simulation of Heat Exchangers", Proceedings of HT2005, 2005 ASME Heat Transfer Summer Conference, San Francisco, CA, USA, July 17-22 (2005).

[16] **Zongqin Zhang, Hongwei Sun, Ahmed Fadl and Mohammed Faghri,** "A concept of Pumpless Convective Micro/Micro Channel cooling Technology", Proceedings of MNHT2008, Micro/Nanoscale Heat Transfer International Conference, Tainan, Taiwan, January 6-9 (2008).

7. Nomenclature

English symbols

A_f cross-sectional area . . . . m^2
c specific heat . .. . J/(kgK)
C_c heat capacity of cold fluid … *W/K*
C_h heat capacity of hot fluid …… *W/K*
C_{min} minimum heat capacity ……. *W/K*
D_h hydraulic diameter . . .. m
D channel height and base . . . . m
h convection heat transfer coefficient ….W/m^2 K
k thermal conductivity . . . . . .W/mK
L channel length . .. . m
$\dot{m}$ mass flow rate . . . . kg/s
p pressure . . .. Pa
q heat transfer rate . . .. .W
T temperature . . . . . K
t_s separating wall thickness . . . . . m
u fluid *x*-component velocity . . . m/s
U overall heat transfer coefficient . . . . $W/m^2.K$
v fluid *y*-component velocity . . . m/s
w fluid *z*-component velocity .. . . .m/s
x axial coordinate . .. . ….m
y horizontal coordinate . . . . . m
z vertical coordinate . . . .m

Greek symbols

ε heat exchanger effectiveness

μ dynamic viscosity . . . . . Pa/s
ρ density . . . . . kg/m^3

Dimensionless groups

$K_r = k_s / k_f$ thermal conductivity ratio

$Re = \rho u_{in} D_h / \mu$ Reynolds number

$\Pr = \frac{\mu C_P}{k_f}$ prandtl number

$Pe = \mathrm{RePr}$ Peclet number

$p^* = \frac{p}{\rho u_{in}^2}$ dimensionless pressure

Subscripts

c cold fluid
f fluid
h hot fluid
in inlet
m mean
min minimum value
out outlet
s solid

Superscripts

* dimensionless value